Mitigation of parametric instabilities based on radiation pressure in gravitational wave detectors

Thomas Harder

UNIVERSITÉ CÔTE D'AZUR

ÉCOLE DOCTORALE
SCIENCES FONDAMENTALES ET APPLIQUÉES

THÈSE DE DOCTORAT

Atténuation des instabilités paramétriques basée sur la pression de radiation dans les détecteurs d'ondes gravitationnelles

Thomas HARDER

Artemis UMR 7250

Présentée en vue de l'obtention du grade de docteur en Physique d'Université Côte d'Azur
Dirigée par : Gilles Bogaert

Soutenue le : 28 Mars 2022

Devant le jury, composé de :
Lisa Barsotti, Massachusetts Institute of Technology, Cambridge, États-Unis
Gilles Bogaert, Artemis, Observatoire de la Côte d'Azur, Nice
François Bondu, FOTON, Université de Rennes, Rennes
Mathilde Hugbart, INPHYNI, Université Côte d'Azur, Nice
Ettore Majorana, La Sapienza, Università di Roma, Rome, Italy
Margherita Turconi, Artemis, Observatoire de la Côte d'Azur, Nice

EGO European Gravitational Observatory

Atténuation des instabilités paramétriques basée sur la pression de radiation dans les détecteurs d'ondes gravitationnelles

Mitigation of Parametric Instabilities based on Radiation Pressure in Gravitational Wave Detectors

Jury:
Président du jury:
François Bondu, Directeur de Recherche, FOTON, Université de Rennes

Rapporteurs:
Lisa, Barsotti, Principal Research Scientist, Massachusetts Institute of Technology, Cambridge, États-Unis
François Bondu, Directeur de Recherche, FOTON, Université de Rennes

Examinateurs:
Mathilde Hugbart, Chargé de Recherche, INPHYNI, Université Côte d'Azur
Ettore, Majorana, Professor, La Sapienza, Università di Roma, Rome, Italy
Margherita, Turconi, Maître de Conférence, Artemis, Observatoire de la Côte d'Azur

Directeur de thèse:
Gilles, Bogaert, Chargé de Recherche-HC, Artemis, Observatoire de la Côte d'Azur

Resumé

La première détection directe des ondes gravitationnelles (OG) a eu lieu en 2015 grâce aux interféromètres , interféromètre de type Michelson à recyclage possédant des cavités Fabry Perot de plusieurs km de longueur dans les bras. Ces cavités permettent une puissance optique élevée, nécessaire pour réduire le bruit de grenaille des détecteurs. Une instabilité paramétrique (IP) est un phénomène optomécanique non linéaire qui transfère une partie de l'énergie du faisceau à un mode propre d'un miroir et à un mode optique d'ordre élevé dont les amplitudes croissent de façon exponentielle. Sans atténuation, l'instabilité fait perdre le contrôle de l'interféromètre. Différentes stratégies d'atténuation les IP ont été proposées et ont été intégrées dans les détecteurs qui ont pu ainsi fonctionner jusqu'au niveau actuel de puissance optique. Pour les détecteurs de prochaine génération, une augmentation de sensibilité d'un facteur dix est visé par rapport aux détecteurs actuels. Une manière d'atteindre ce but consiste à augmenter la puissance optique dans les cavités des bras. Cette augmentation pourrait impliquer plus d'IP, plus difficiles à atténuer.

Dans cette thèse nous proposons une méthode active et flexible d'atténuation des IP, qui utilise la pression de radiation d'un faisceau laser dédié. L'idée est d'appliquer une contre pression sur plusieurs points du miroir grâce à un petit faisceau laser, avec des fréquences de dizaine de kHz. A cette fin, la déflection rapide du faisceau est requise. Par ailleurs, il faut être capable de détecter les IP dès leur naissance, au niveau de l'excitation thermique.

Cette thèse présente les premières études expérimentales d'un tel système : la déflection rapide basée sur des modulateurs acousto-optiques est explorée. Une fréquence de déflection de 10 MHz en 2D est démontrée. La puissance optique maximale du faisceau dévié est 3,6 W, ce qui correspond à une force de pression de radiation de 24 nN. Ces caractéristiques remplissent les conditions nécessaires.

La détection des modes mécaniques d'un miroir est étudiée à l'aide d'un system utilisant un interféromètre de Michelson. La sensibilité obtenue pour un faisceau en position fixe sur le miroir correspond à un changement de longueur de bras de $\delta L = 4.8 \cdot 10^{-14} \frac{\mathrm{m}}{\sqrt{\mathrm{Hz}}}$. Cette valeur est environ un ordre de grandeur plus élevée que le déplacement de la surface du miroir due à l'excitation thermique des modes mécaniques. Des propositions sont données pour améliorer la sensibilité de l'interféromètre et pour utiliser ce système pour étudier l'atténuation active des modes propre d'un miroir par la pression de radiation.

Mots-clés: détecteur d'onde gravitationnelle, instabilité paramétrique, pression de radiation, déflection de faisceau, détection des modes mécaniques

Abstract

Direct detection of Gravitational Waves was demonstrated for the first time in 2015 with km-scale Michelson interferometers. In order to reduce the shot noise at high frequency of these detectors high optical power in the arm cavities is needed. At that high circulating power a nonlinear optomechanical phenomenon called parametric instability (PI) may occur that induce the amplification of mirror's eigenmodes. It limits the optical power and can cause the loss of the interferometer's control if not mitigated.

Several PI mitigation strategies have been proposed and already implemented in current gravitational wave detectors. These schemes keep them working without PI at the current optical power level in the cavities but they are not adapted to PI involving any kind of mechanical mirror modes, which needs to be considered when the optical circulation power is increased further. Next generation detectors aim at increasing their sensitivity of a factor of ten compared to current detectors. This can be achieved, inter alia, through the increase of the optical power in the arm cavities which will imply more PI.

In this thesis an active and flexible PI mitigation strategy based on radiation pressure of a movable laser beam is proposed. The idea is to apply a damping force to mitigate PI. Fast beam steering is required to point at different positions of the cavity mirror with a small laser spot during one period of the mechanical mode with frequencies in the kHz-range. A sensitive sensing method is required to detect PI at the level of thermal excitation.

First experimental studies of a table-top setup are presented: rapid beam deflection based on acousto-optic modulators is investigated. A final configuration with 2D arbitrary beam steering with a maximal deflection rate of 10 MHz is demonstrated for a maximal optical power of 3.6 W, corresponding to a radiation pressure force of 24 nN. It satisfies the requirements of the laser beam that should be used as radiation pressure force for our proposed PI damping scheme.

Sensing of mechanical mirror modes is investigated with the 2D beam steering system based on a Michelson interferometer. A sensitivity corresponding to a differential arm length change of $\delta L = 4.8 \cdot 10^{-14} \frac{\mathrm{m}}{\sqrt{\mathrm{Hz}}}$ is achieved for a fixed beam position on the mirror. It is around one order of magnitude higher than the expected displacement of the mirror due to thermally excited mirror modes. Propositions are given to

improve the sensitivity of the interferometer and to use the same setup to investigate active damping of mirror modes via radiation pressure.

Keywords: gravitational wave detectors, parametric instability, radiation pressure, beam deflection, mechanical mode sensing

For my beloved and beautiful Lauritas
who is deep and purely loving and more
inspiring, than any galaxy as far and large
and colourful it could be.

Acknowledgement

Looking back on the past 3 years gives me many reasons to be thankful. I really liked my working place in the office in *Maison Jumelle* on the *Mont Gros* of the Observatory site in Nice. The amazing view on the city and the sea is really inspiring. But these were only the soft facts. It was a great privilege to work together with Margherita, Rémi, Walid and Gilles. I appreciated Walid's rigorous and detailed advises at various stages of my research. I could learn a lot from Rémi's experiences in experimental work and enjoyed working with him in the clean room. It helped me to advance in my reflections and work when Margherita came in my office and asked me about the state of art and gave me some ideas. I was benefiting a lot from her profound and detailed reviews on my thesis manuscript. Gilles was easy to join and always available for a discussion which helped me a lot to do all administrative formality. It was a great pleasure to be a part of the Artemis laboratory directed by Nelson, who was always available and come once a while in my office to ask how things were going.

As a Phd-student it was so healthy and enjoyable to share my office with fellow students like Cosmin, Guillaume and Adrian and later during my studies Kamiel. The good atmosphere and discussions once a while were making my working place a lovely place where I enjoyed to work every day. A big reason to come every day to the observatory instead of working at home was the restaurant on the site. Khalid was not only cooking delicious meals but provided also a good and joyful ambience during lunch. The lunch time in the restaurant was also a great opportunity to get to know other scientist on the site.

An important help for my experimental work were Jean-Pierre, providing inter alia control loops for my experimental setup and Mourad, doing simulations with Ansys for my project. I enjoyed the friendship with colleagues like Marco, Cosmin and Loïc, who were not only willing to share their work experience but were available to go skiing on the weekend and hiking in the mountains of the back land of Nice. These outdoor activities were important for my work-life balance.

My church in Nice, *Calvary Chapel Nice*, became my family here: As I arrived in Nice, I didn't know anyone but at church I was warmly welcomed which helped me to settle. Their prayers were a great encouragement for me during my studies and especially during the end when I was writing the manuscript.

It is a miracle for me how I got to know my wife during my studies. She has been

a great encouragement for me and was supporting me especially during the time I was writing the thesis : sometimes it was just her smile or a meal or a cake, but it helped me to go on.
I want to say also a special thank to my brother Stefan, who was calling me to support me and had time for me which gave me always hope and new courage. I am so glad, I could stay at my parents' place in Germany during the two months of lockdown in 2020. Their fellowship and our common meals were a healthy change during these months of working at home. I guess, I would have been affected psychologically during that time of isolation, if I could not be surrounded by my parents and my family.
During the last months of my thesis I was mainly writing the manuscript and I was hosted at different places with my wife. It was a great opportunity to fill my need of social interactions during that time. I want to thank my parents and parents-in-low, who opened their house for us and my cousin Sascha with his wife.
Last but not least I want to thank my father in heaven, the creator of heaven and earth, the beginning of everything and everyone for his strength and encouragement which I experienced during my doctoral studies as it is written in the Bible in Isiah 40,29: **He gives strength to the weary and increases the power of the weak**. [New International Version, 2011]

Contents

Acronyms

2D,3D	Two/Three-Dimensional
AC	Alternating Current
AMD	Acoustic Mode Damper
AO	Acousto-Optical
AOM	Acousto-Optic Modulator
CPU	Central Processing Unit
DC	Direct Current
DE	Deflection Efficiency
DDS	Direct Digital Synthesizers
DMA	Direct Memory Access
DPDK	Data Plane Development Kit
EOM	Electro-Optic Phase Modulator
ESD	ElectroStatic Drive
FIFO	First-In-First-Out
FPGA	Field-Programmable Gate Array
GR	General Relativity
GW	Gravitational Wave
I/Q	In-phase and Quadrature
KTN	Potassium(K),Tantalum (Ta) and Niobium (Nb)
MTU	Maximal Transmission Unit
O1,O2,..	Observation Run 1,2,...
OPA	Optical Phased Array
PI	Parametric Instability
Q-factor	Quality-Factor
RF	Radio Frequency
RAM	Residual Amplitude Modulation
RIN	Relative Intensity Noise
RMS	Root Mean Square
UHD	USRP Hardware Driver
USRP	Universal Software Radio Peripheral

Preface

The experimental work presented in this thesis has been done at the *Artemis Laboratory, Observatoire de la Côte d'Azur, Nice* in France. A flexible active mitigation strategy of parametric instability in gravitational wave detectors is presented which is based on radiation pressure applied by a small and movable laser beam. The content of this thesis is structured in the following way:

In **chapter 1** gravitational waves are introduced. A brief historical overview on the development of gravitational wave detectors is given. The working principle of current detectors based on a Michelson interferometer is discussed. Important noise sources that limit the sensitivity of these detectors are pointed out.

In **chapter 2** the optomechanical phenomenon of parametric instability is explained. Experimental observations of this effect are reviewed and its limiting impact on gravitational wave detectors is highlighted. Subsequently, mitigation strategies of parametric instabilities are classified. Strategies that have already been implemented in current detectors are reviewed.

Chapter 3 presents the flexible and active mitigation scheme of parametric instability based on radiation pressure applied by a movable beam. The requirements on the laser source and on the beam deflection for this scheme are discussed. Furthermore, possible ways to apply radiation pressure with this laser beam are presented.

In **chapter 4** the experimental investigations of rapid beam deflection are presented. Acousto-optic modulators are used in order to deviate the beam. Two different driver signal generation schemes for these modulators are studied. The results of a final setup of rapid two-dimensional beam deflection are presented, which satisfy the requirements of the movable radiation pressure source for parametric instability mitigation.

In **chapter 5** an experimental setup based on a Michelson interferometer for sensing the mechanical modes of a mirror is presented as an important part of the active mitigation scheme. Limits of this setup are discussed. Propositions are given to

observe mechanical mirror modes in this table-top experiment in order to investigate active damping of mirror modes via radiation pressure.

Chapter 6 concludes this thesis. The importance to further develop parametric instability mitigation strategies is pointed out. The presented experimental results in this work are summarized, as an important step towards implementing an active and flexible parametric instability mitigation scheme in future gravitational wave detectors.

1 Introduction

1.1 Gravitational Waves

In 1916 Albert Einstein published the theory of General Relativity (GR) [1]. In this theory gravity is described as the curvature of a four-dimensional geometry of space and time, the spacetime [2]. In Newtonian physics spacetime is infinitely rigid and interactions between masses are instantaneous [3]. GR predicts, though, that it is elastic with an enormous high stiffness, 10^{22} times stiffer than diamond [4]. Interactions between masses propagate with the speed of light. Moving masses may also generate waves, known as gravitational waves. They can be interpreted as ripples in the shape of the four-dimensional spacetime. The amplitude of these waves is infinitely small and their coupling to matter is weak [2]. This makes the detection of gravitational waves so challenging but also so interesting. Even waves from far sources in the universe reach earth. They deliver information from objects like compact binary systems of neutron stars and/or black holes and supernova explosions.

In vacuum, at large distance from their source, gravitational waves are transverse, like electromagnetic waves. Their amplitude oscillates in a plane perpendicular to the direction of their propagation. Gravity has, in contrast to electromagnetism, only one charge: the mass. Whereas electromagnetic waves are generated by a time-varying dipole moment caused by positive and negative charges, gravitational waves are ordinarily generated by a time-varying quadrupole moment. Thus, non-spherical, non-rectilinear motion of mass will generate gravitational waves [2].

Figure 1.1 shows the distortion of a ring of point particles (green dots) during one period of the gravitational wave. While the point particles themselves stay locally at rest, their relative distances oscillate due to the change of the spacetime metric [5]. The propagation direction of the gravitational wave in this figure is perpendicular to the page and two independent polarisations of the gravitational wave, (+) and (x) are shown. In contrast to electromagnetic waves, the two polarisations of gravitational waves describe an angle of 45 degrees.

The amplitude of the gravitational wave h is measured by the change of the relative distance between two test masses, caused by the oscillating metric of spacetime. It is

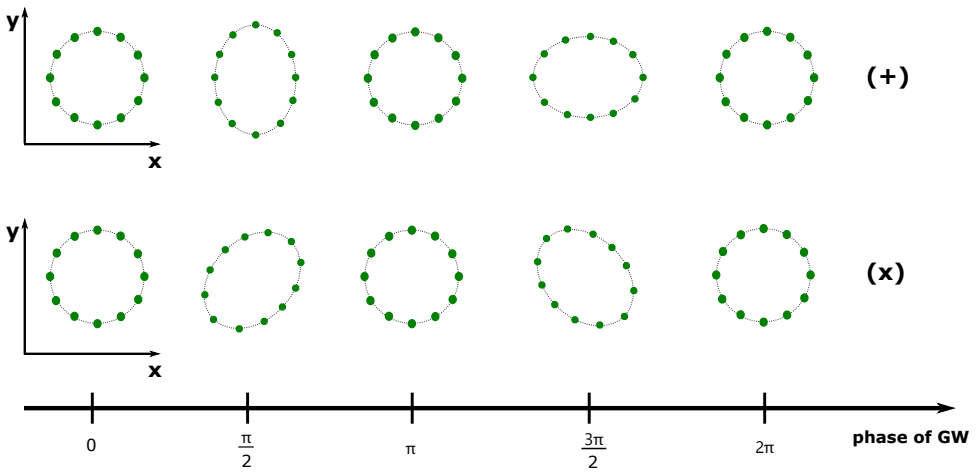

Fig. 1.1: A gravitational wave with (+) and (x) polarisation acting on a ring of point particles (green dots) in the xy plane while passing perpendicular to the page. The distortion of the particles is shown for different phases of the gravitational wave.

given by $\Delta L/L$, with the equilibrium distance L between the test masses and ΔL the distance change of two masses due to the passage of a gravitational wave.

In 2015, around hundred years after their prediction, the first gravitational wave was simultaneously detected in the two detectors of the Laser Interferometer Gravitational-Wave Observatory (LIGO) originating from a Binary Black Hole Merger [6]. Since then, more than 50 gravitational-wave events have been detected directly [7].
In order to detect more gravitational-wave events with even smaller amplitudes and from different sources than already detected, the sensitivity of the detectors needs to be increased. But this implies, inter alia, overcoming several limiting factors in the detectors. In this thesis a mitigation strategy of a possible limiting factor in current und future gravitational wave detectors, called parametric instabilities, is presented.

1.2 Gravitational Wave Detectors

In the beginning of the 60s, Joseph Weber proposed methods to generate and detect gravitational waves in a laboratory [8]. He built a first gravitational wave detector consisting of a suspended 1.5 ton aluminium cylinder in a vacuum chamber [9]. He measured the amplitude of normal eigenmodes of this test mass which may change when a gravitational wave passes and excites them. In 1969 he claimed to have detected a gravitational wave by observing a coincidence of two such detectors with a distance of about 1000 km in the USA [10]. This drew the attention of scientists all over the world who started to build such detectors with even higher sensitivities but they could not confirm Weber's claim [11].

A review covering the historical evolution and technical aspects of such so-called Resonant-Mass gravitational wave detectors can be found in [11].
In the 70s an alternative approach to detecting gravitational waves was experimentally investigated by different working groups, which were partially exchanging ideas and expertise [12]: laser interferometry to measure distance changes using suspended test masses. Some of the scientists who were leading such experimental work were Robert L. Forward with his group at the Hughes Research Laboratories in Malibu, California [13, 14], Rainer Weiss in the Research Laboratory of Electronics (Massachusetts Institute of Technology) in Massachusetts, USA [15], Heinz Billing with his group in the Max-Planck-Institut fuer Physik und Astrophysik in Munich, Germany [16] and Drever with his group in Glasgow, UK [12]. Laser interferometer detectors were promising, since higher sensitivity could be achieved, and this in a wider frequency range than Resonant Mass detectors.
In the next section the principle of laser interferometers will be reviewed.

1.2.1 Michelson interferometer for gravitational wave detection

A simplified setup of a GW interferometric detector is depicted in figure 1.2. It is a Michelson interferometer with a suspended semi-transparent mirror with a reflectivity of 50% (50/50 beam splitter) and two suspended mirrors. These are the test masses which will change their relative distances to the beam splitter when a gravitational wave passes. For this reason the mirrors in GW detector interferometers are also called test masses.
The incoming laser beam is split into two beams at the beam splitter. Both beams

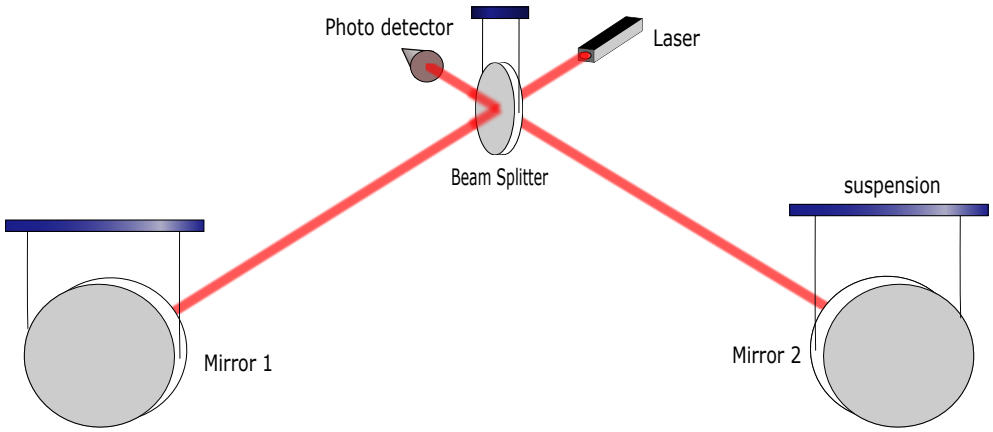

Fig. 1.2: Simplified optical setup of a Michelson interferometer for gravitational wave detection.

are reflected off mirrors 1 and 2 respectively, before being recombined in the beam splitter. The arm length of both interferometer arms is equal. One part of the recombined beam goes into the detector and the other part goes back towards the

laser.

If the optical path length of the laser beam in each interferometer arm is equal, the beams will interfere destructively (dark port) in the port towards the detector and both beams will interfere constructively (bright port) in the port back to the laser. If a gravitational wave passes the interferometer it will change the metric of the spacetime. This will be detectable as intensity modulation at the detector.

Let us assume a perfect 50/50 beam splitter without any absorption and mirrors

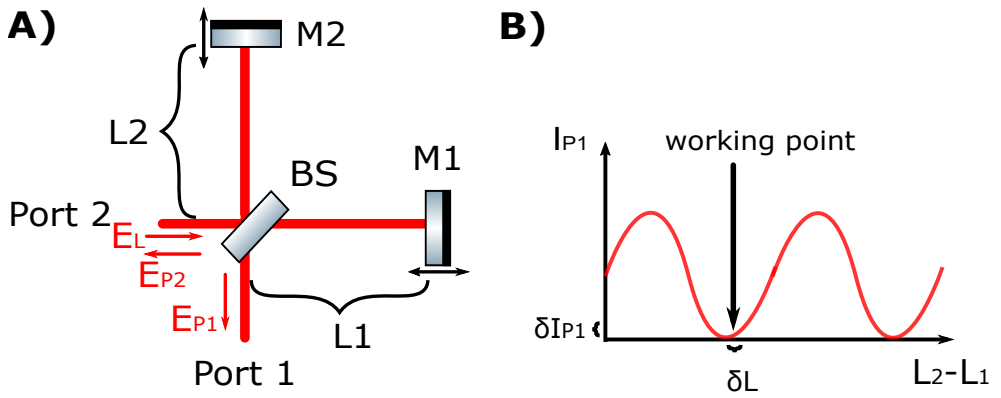

Fig. 1.3: Interference in a Michelson interferometer for gravitational wave detection. A) Schematic of a Michelson interferometer with incoming electromagnetic wave E_L through port 2. The wave is split into two arms at a 50/50 beam splitter (BS). Both beams are reflected off mirrors 1 and 2 (M1,M2), respectively and recombine in the beam splitter. Depending on the distance L1 and L2 of both mirrors from the beam splitter, the exiting wave at port 1 E_{P1} is described in equation 1.6 and the wave at port 2 E_{P2} is described in equation 1.7. B) Interference curve a port 1 depending on the differential arm length of L1 and L2 with the working point of the interferometer for gravitational wave detection. The working point is at the dark fringe with a small offset. In this way there exists approximately a linear relation between the differential arm length change δL due to the passage of a gravitational wave and the corresponding measurable intensity modulation δI_{P1}.

with 100% reflectivity (see figure 1.3), the electromagnetic wave (only considering the electric field of the wave) $E_L(t)$ of an incoming monochromatic laser beam with wavelength λ_L at the beam splitter can be written as

$$E_L(t) = E_0 \cos(\omega_0 t) \tag{1.1}$$

with an amplitude E_0 and angular laser frequency of $\omega_0 = \frac{2\pi c}{\lambda_L}$ with the speed of light c. Thus, both waves E_1, E_2, after reflecting off both mirrors respectively, and before interfering in the beam splitter, can be written as (approximation for a beam splitter with infinitely small thickness)

$$E_1(t) = -\frac{E_0}{\sqrt{2}} \cos\left(\omega_0 t - 2\omega_0 \frac{L_1}{c}\right) \tag{1.2}$$

$$E_2(t) = -\frac{E_0}{\sqrt{2}} \cos\left(\omega_0 t - 2\omega_0 \frac{L_2}{c}\right) \tag{1.3}$$

The superposition of both electric waves E_{P1}, E_{P2} in port 1 and 2 equals

$$E_{P1}(t) = \frac{E_1(t) - E_2(t)}{\sqrt{2}} = -E_0 \sin\left(\omega_0 t - \omega_0 \frac{L_1 + L_2}{c}\right) \sin\left(\omega_0 \frac{\delta L}{c}\right) \tag{1.4}$$

$$E_{P2}(t) = \frac{E_1(t) + E_2(t)}{\sqrt{2}} = -E_0 \cos\left(\omega_0 t - \omega_0 \frac{L_1 + L_2}{c}\right) \cos\left(\omega_0 \frac{\delta L}{c}\right) \tag{1.5}$$

for the relative arm length difference $\delta L = L_2 - L_1$ and under the consideration that a reflected beam acquires a phase shift of π if the incident beam approaches the reflective surface (e.g. beam splitter) from a less optically dense medium (e.g. air or vacuum) and no phase shift if it encounters the reflective surface from a more optically dense medium (e.g. inside the beam splitter) [17].
The intensity measured with a photodiode is given by the relation of $I \propto E(t)^2$. Since a photodiode is not able to detect the fast oscillation of the first term of equation 1.4,1.5 it will only see a temporal average of this term. The intensities I_{P1}, I_{P2} measured in port 1 and 2 are:

$$I_{P1} = \frac{I_0}{2}\left(1 - \cos 4\pi \frac{\delta L}{\lambda_L}\right) \tag{1.6}$$

$$I_{P2} = \frac{I_0}{2}\left(1 + \cos 4\pi \frac{\delta L}{\lambda_L}\right) \tag{1.7}$$

where I_0 is the intensity of the laser. For current gravitational wave detection the working point of the interferometer is chosen in a way to measure in the dark port with a little offset, known as DC-readout [18]. In this configuration, an approximately linear relation is achieved between small variations of δL of L1 and L2 and the resulting intensity modulation in the dark port [17].

Assuming a plus-polarized gravitational wave with an amplitude a propagating in z-direction perpendicular to the laser interferometer plane as depicted in figure 1.4 with an angular frequency Ω and the x- and y- axes orientated along the two interferometer arms the distance change $\delta L_x, \delta L_y$ of both interferometer arms with an equal arm length L can be described as [2]

$$\delta L_x(t) = \frac{1}{2} a L \sin \Omega t \tag{1.8}$$

$$\delta L_y(t) = -\frac{1}{2} a L \sin \Omega t \tag{1.9}$$

From equation 1.6-1.9 it can be concluded, that the longer the interferometer arm L the greater the change of the interference pattern for a given amplitude a of the gravitational wave. However, to increase the sensitivity of the detector the arm length should not only be chosen arbitrarily high. Imagine measuring the swell of the ocean with two buoys floating on the ocean. The optimum is to place both buoys with a distance equal to half the wavelength of the wave you want to measure. Then

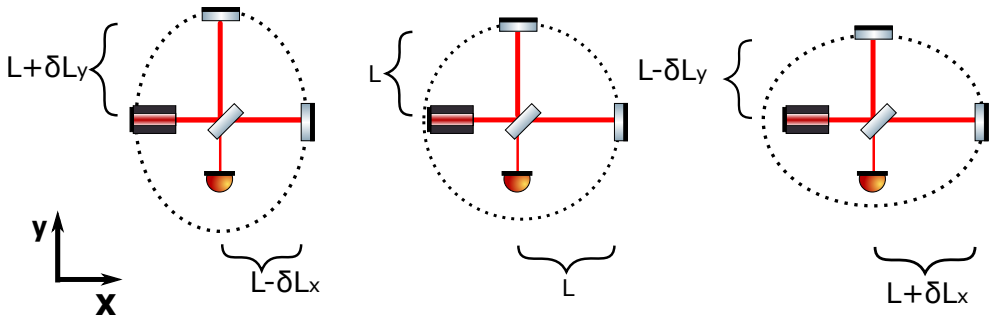

Fig. 1.4: Impact on the arm length of a Michelson interferometer if a (+) polarized gravitational wave passes perpendicular to the page. The effect is depicted for different phases of the gravitation wave.

they will move in anti-phase and the relative movement is maximized [3].
In this way, the optimum arm length L equals $L = \frac{c}{4\nu_{GW}}$ for a given frequency ν_{GW} of the gravitational wave. For a gravitational wave with ν_{GW}=100 Hz the optimum arm length is L=750 km. Such arm lengths would pose some technical problems when constructing an interferometer on Earth because of its curvature.
Different solutions have been proposed in order to maximize the intensity variation measured at the dark port of the interferometer when a gravitational wave passes without increasing the arm lengths.
One solution consists in adding delay lines [19]. The idea is to let the light bounce several times between two concave mirrors back and forth without interference of adjacent beams.
Another solution, which is currently used in GW detectors, is to use a Fabry-Perot cavity in the interferometer arms. It also consists of two mirrors but the back and forth reflected beams in the cavity are superposed and interfere either constructively or destructively depending on the laser wavelength and the distance between the mirrors.
The effective interferometer arm is increased by a factor N for constructive interference in the Fabry-Perot cavity given by

$$N = \frac{2F}{\pi} \tag{1.10}$$

with the finesse F of the cavity determined by the different reflectivity of both cavity mirrors.

1.2.2 Advanced Gravitational Wave detectors

The first generation of large scale gravitational wave detectors was two LIGO interferometers with 4 km arms in the USA [20], a Virgo interferometer with 3 km arms in Italy [21], GEO600 with a 600 m arms in Germany [22] and TAMA with 300 m arms in Japan [23]. They were all power-recycled Michelson interferometers

and were designed and reached their nominal sensitivity. Several modifications in the optical setup were done, the injected laser power into the interferometer was increased and technical improvements were realized in the detectors in the following years to increase the sensitivity.

LIGO and GEO600 started joint runs in 2005 [12]. The GEO600 interferometer served as detector but was also used to develop new technologies. In 2007, Virgo and LIGO agreed to collaborate in order to search for GW together and exchange data [12]. Between 2007 and 2011, LIGO, Virgo and GEO observed together several times.

Advanced LIGO [24] and Advanced Virgo [25] are so-called second generation GW interferometric detectors. They were designed to achieve a strain sensitivity of factor 10 better than the initial detectors that had not detected any GW. Advanced LIGO started its first observation run in 2015 and Advanced Virgo joint during the second observation run in 2017.

A simplified setup of Advanced GW detectors is depicted in figure 1.5. A) shows the optical setup of Advanced GW detectors and B) shows a picture of the Virgo site in Italy, close to Pisa.

Electro-optic phase modulators (EOM) are implemented to create side bands which are used to control and lock the interferometer [26]. The input mode cleaner (IMC) is used to prestabilize the laser frequency, to filter beam jitter and send a proper transverse optical mode into the interferometer. As the interferometer is locked to dark fringe at the detector the whole optical power will return back into the laser. In order to protect the laser from back reflection an optical Faraday-isolator is used (ISO). And a power recycling mirror (PRM) is installed to reuse the exiting optical power from the bright port of the interferometer (going back into the laser) by reflecting it back into the interferometer. A 50/50 beam splitter devides the beam into two orthogonal propagating beams with equal power. Each arm is composed of a Fabry-Perot cavity with a spacing between the input test mass (ITM) and end test mass (ETM) of 4 km for the two LIGO interferometers and 3 km for the Virgo interferometer. Because of the high reflectivity of the Fabry-Perot mirrors, resulting in a finesse of around 450, the design optical power stored in the cavity is around 700 kW for LIGO and Virgo. This high circulating power involves optomechanical effects which are the starting point for this thesis.

A signal recycling mirror (SRM) modifies the response of the detector to gravitational waves. It builds a cavity with the beam splitter. By changing the position of the SRM in a microscopic scale, the resonant frequency in the cavity is changed. This can be used to enhance the sensitivity of a specific frequency band. The bandwidth is determinded by the reflectivity of the SRM [27]. It has been used only by Advanced LIGO during O3. The output mode cleaners (OMC) are used to filter out sidebands and higher-order optical modes in the beam that are not relevant for GW detection. In this way the contrast of the detected signal is increased and the shot noise is minimized, which results in an increase of the detectors sensitivity [26].

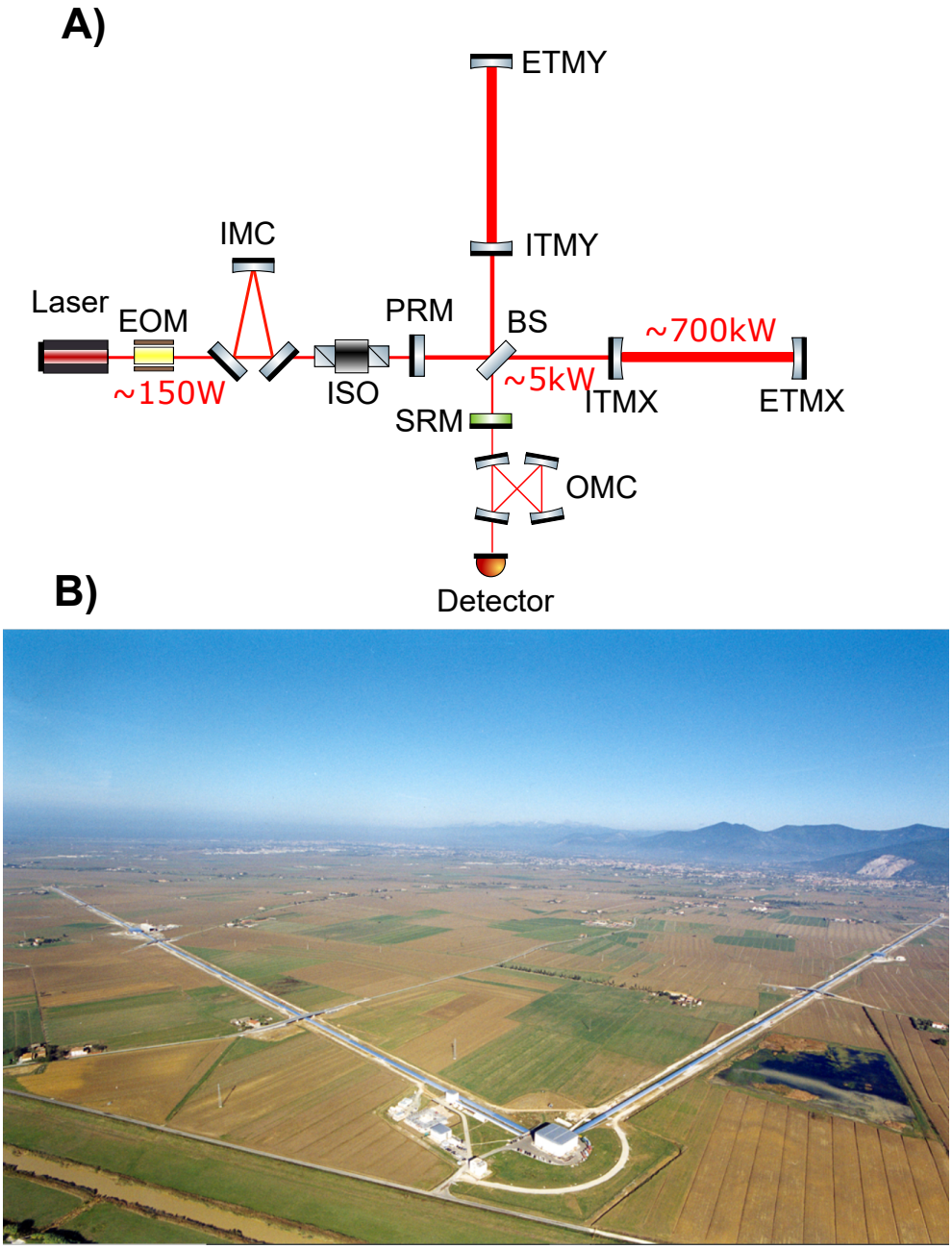

Fig. 1.5: The advanced gravitational wave detector. A) Simplified Optical Setup of Advanced GW detectors with the following optical components: EOM- electro-optic modulator, IMC -input mode cleaner, ISO- Faraday-isolator, PRM - power recycling mirror, BS- 50/50 beam splitter, ITM- input test mass and ETM- end test mass in X and Y direction, SRM- signal recycling mirror, OMC output mode cleaner. B) Photo of the Virgo site in Cascina, near Pisa, Italy (figure taken from [28])

The measured strain sensitivity of the Advanced LIGO and Virgo interferometer during their joint observation run O3 with GEO600 is depicted in figure 1.6. It is the amplitude spectrum of the measured noise in the detection band between 10 Hz and 10 kHz. The peak sensitivity reaches down to a strain of $\sim 10^{-23}\frac{1}{\sqrt{\text{Hz}}}$, which corresponds to a relative distance change of both interferometer arms of around 10^{-20} m.

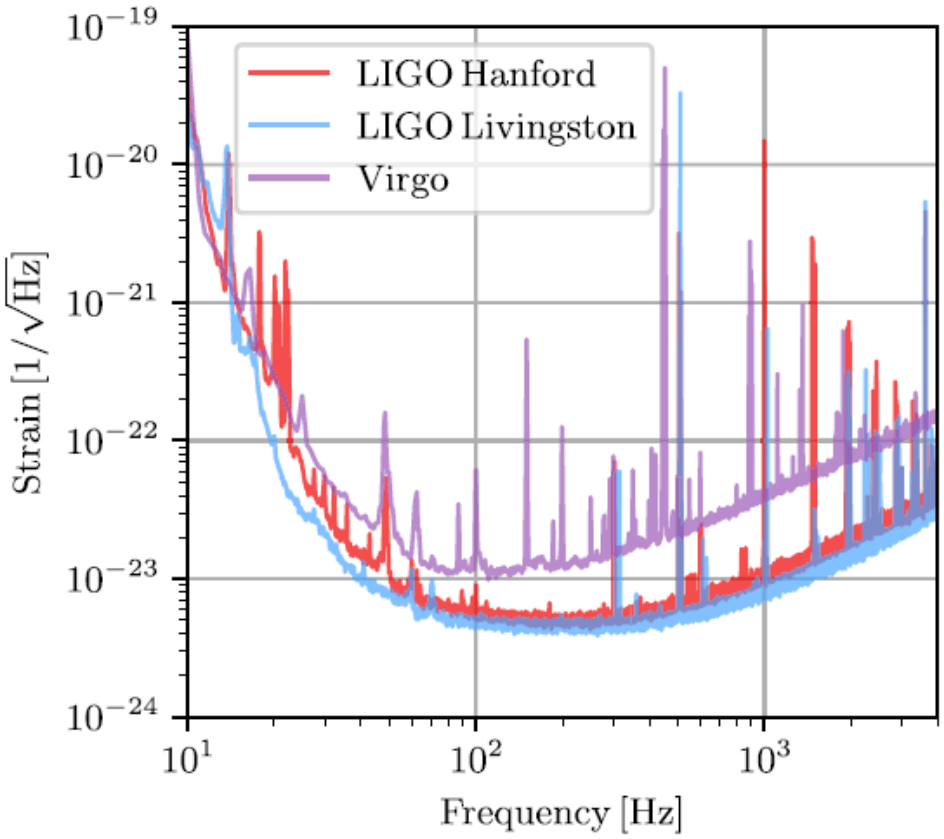

Fig. 1.6: Strain Sensitivity curve of Advanced Virgo and LIGO measured in 2019 during observation run O3. (figure taken from [29])

In 2010 the construction of a cryogenic interferometric GW detector 3 km, called Kagra, deep in a mountain with cryogenic mirrors and 3 km arms was started in Japan [30]. It joined the LIGO/Virgo collaboration in 2019 and joined the third observation run of LIGO/Virgo for the last months of 2020. Figure 1.7 shows the location of current large scale interferometers with the orientation of the interferometer arms. It is expected to make the reconstruction of the GW waveform more precise as well as the source localisation by including Kagra in the global network of gravitational wave detectors [31]. LIGO-India is a project to establish a state-of-the-art advanced LIGO gravitational wave interferometer in India which will improve the source localisation of GW sources [32].

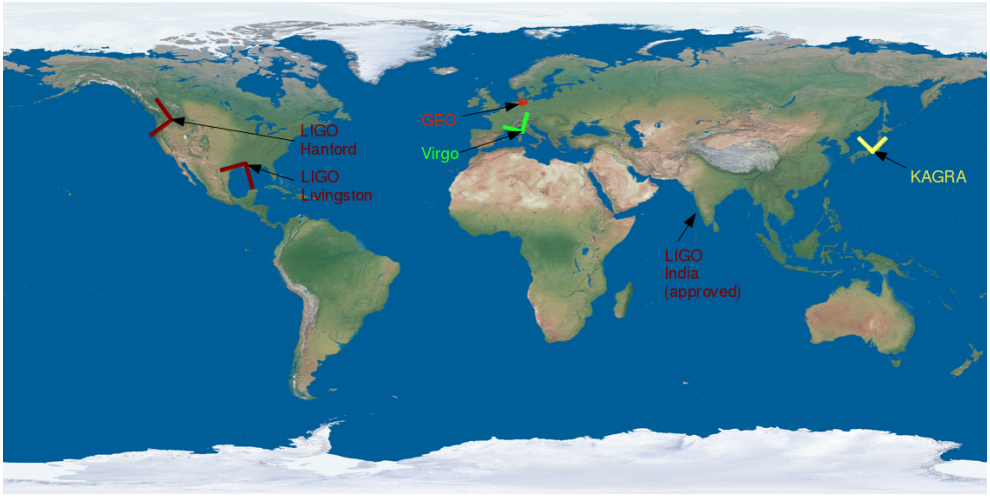

Fig. 1.7: Global network of second generation interferometric gravitational wave detectors. (figure taken from [28])

1.2.3 Noise sources in ground-based GW detectors

The sensitivity of GW interferometric detectors is limited by several noise sources. Figure 1.8 shows the strain sensitivity curve of Advanced Virgo for a 125 W input laser power and with signal and power recycling mirrors. Some noise sources constituting this curve are also plotted. As one might see, increasing the sensitivity of GW detector interferometer means decreasing the noise in the interferometer. Some noise sources will be reviewed in the following:

- **Seismic noise**: It is due to motion of the ground where the interferometer is situated. Sources are for example waves impinging on the continent, storms and human activity on the site. The average noise depends on the place on the earth. But even for a relatively quiet site below ground at the site, the amplitude of the seismic motion is still around $10^{-13}\frac{m}{\sqrt{Hz}}$ at 100 Hz [3]. This noise level is far above the the displacement change one wants to measure, due to the passage of gravitational waves. For this reason the interferometer needs to be isolated from seismic vibrations of the ground. This is realized in current GW detector interferometers by the suspension of the test masses by several stages of active and passive vibration isolation systems.

- **Newtonian Gravity noise (Gravity Gradients)**: It is related to the seismic noise but the detector cannot be isolated against it by springs and pendulums as for seismic noise. It is caused by local density fluctuations (earth, air) which act directly via the gravitational force on the test mass. Sources are seismic waves, human activity and moving massive bodies in the vicinity of the test masses. It limits the sensitivity of GW detector interferometer below 10 Hz [33]. If this noise is measured in the environment of the interferometer,

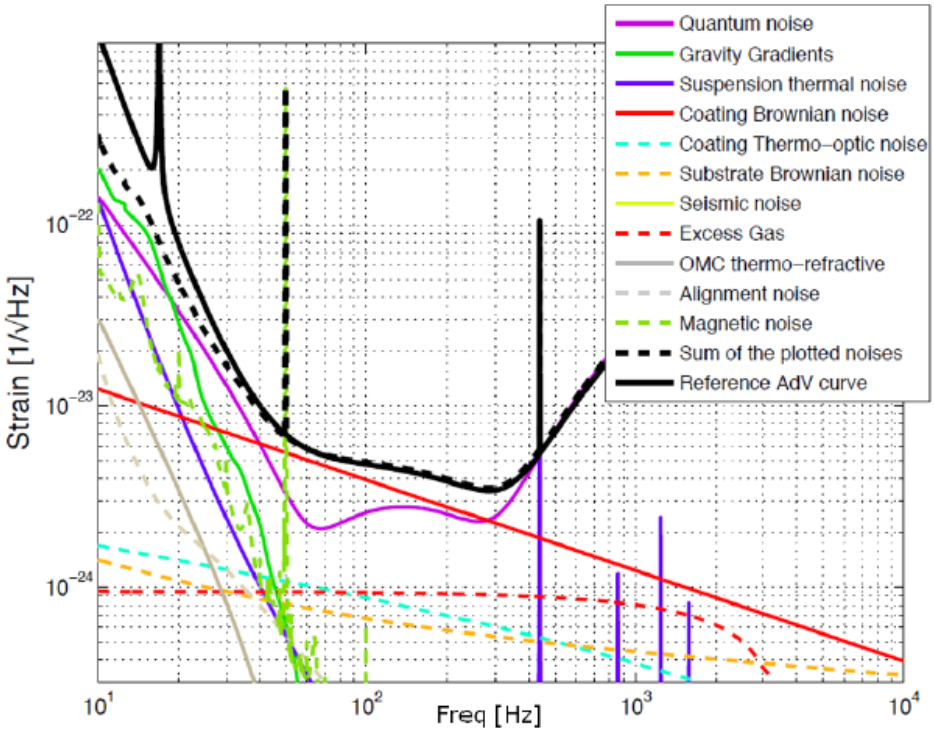

Fig. 1.8: Advanced Virgo strain sensitivity for a detuned dual recycled configuration with 125 W of input power (solid black line). The noise contribution of some noise sources are also plotted. (figure taken from [7])

the measured GW signal of the detector can be extracted from this noise backgroud[34]. Newtonian gravity as well as seismic noise can be reduced by running the interferometer underground [35].

- **Thermal noise**: Random thermal fluctuations induce motion of the test mass which is the source of this noise. It affects three components of the test mass in a different way: the substrate, the coating and the suspension. The coating Brownian thermal noise and the suspension thermal noise are predominant in the detection band of Advanced GW detectors.
  The test masses are coated with dielectric layers in order to obtain a high reflectivity for the laser wavelength. Internal friction and friction between the layers and the substrate are the reason for the coating Brownian thermal noise [36]. By sensing the test mass with a larger beam diameter the coating noise can be reduced [37].
  Vibration of the suspension wire is coupled to the test mass. By choosing a low-dissipation material for the suspension wires, the suspension thermal noise can be minimized.

- **Quantum noise**: The origin of this noise comes from the quantum property of the photons in the interferometer. It comprises quantum shot noise and

quantum radiation pressure noise. Quantum shot noise arises from the fluctuation of the number of photons detected by the photo detector in a given time interval. The strain sensitivity associated to quantum shot noise is proportional to $1/\sqrt{P}$ with the total optical power P in both interferometer arms [38].
But the the strain sensitivity associated to quantum radiation pressure is proportional to $\sqrt{P}$ [38]. It arises from the fluctuation of the number of photons impinging on the test masses during a given time interval. This implies a fluctuation of radiation pressure on the test masses which causes a displacement noise. By increasing the mass of the test masses radiation pressure noise can be reduced.

1.2.4 Next generation ground-based GW detectors

Advanced LIGO, Advanced Virgo and Kagra are currently in preparation for the next observation run O4 in the end of 2022. Different modifications of the detectors will be realized, such as the increase of the injected laser power in the interferometer in order to increase the sensitivity further [7, 39].
Further improvements of the second generation detectors are foreseen between O4 and O5.
Third generation gravitational wave detectors have already been proposed and aim to obtain a sensitivity of factor ten higher than Advanced detectors. The European proposal is the Einstein telescope. It is a triangular observatory consisting of three nested detectors around hundred meters underground [40, 41]. Each detector consists of a high-power interferometer which will work at room temperature sensitive to high frequency and an interferometer which will have cryogenic test masses sensitive to low frequencies (see figure 1.9). At the design power of 3 MW in the arm

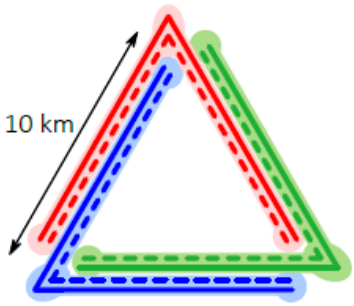

Fig. 1.9: Schematic of the Einstein Telescope geometry with three nested detectors (figure taken from [5])

cavities, the optomechanical effect of parametric instabilities is considered which needs to be mitigated in order to attain such high optical powers in the cavities [42].

The American concept of a third generation detector is the Cosmic Explorer. It is an interferometer with L-shaped arms of 40 km length and build on the earth's surface with circulating arm cavity powers of 1-3 MW. [43, 44].

At these high optical powers an optomechanical phenomenon, called parametric instabilities can pose problems. It will be explained in the following chapter.

2 Parametric Instability

2.1 Introduction

The design power in Advanced LIGO and Virgo is around 700 kW in the arm cavities [25, 24]. This power level gives rise to several optomechanical interactions between the cavity beam and the suspended mirrors. There are for example the Sidles Sigg Instabilities [45], a torsional optical spring effect that couples both mirrors of the Fabry-Perot cavity. It needs to be controlled in order to keep the detector working [24]. Another phenomenon called parametric instability (PI) results in the amplification of the test mass eigenmodes. This poses a problem since the control of the interferometer is lost if these instabilities are not mitigated [46].
Brankinsky et al. predicted this opthomechanical interaction in Fabry-Perot cavities in 2001 [47] and did a first analysis of PI in the power recycled LIGO interferometer [48]. He compared this phenomenon to stimulated Brillouin scattering and predicted that it would create a limit of the maximal energy stored in the arm cavities.

In this chapter, I will review the theory of parametric instability, its first observations and methods to mitigate this optomechancial phenomenon in GW detectors. In Section 2.2 the conditions which need to be fulfilled in order to observe this nonlinear effect in cavities are pointed out. A model introduced by Evans et al. in [49] to describe this phenomenon is presented. In Section 2.3 the parametric gain is introduced, which is a dimensionless quantity characteristic of PI. The first observations of PI proving the theoretical models are reviewed in Section 2.4. In Section 2.5 different PI mitigation strategies are reviewed and classified. Three PI mitigation methods which have already been implemented in current Advanced GW detectors are explained in detail. And a conclusion is given at the end of this chapter.

2.2 Three-mode optomechanical interaction

A three-mode optomechanical interaction involves the fundamental optical cavity mode at an angular frequency of ω_0, a higher-order transverse optical mode at ω_1 and a mechanical mode of a cavity mirror at ω_m. The mechnical modes of the mirror can

be excited for example due to thermal excitation. The interaction can be described as a scattering process of photons and phonons as depicted in figure 2.1. If the photons of the fundamental mode hit the vibrating mirror at ω_m, they can either be scattered into a photon with lower frequency $\omega_0 - \omega_m$ by creating a phonon with ω_m, or they are scattered into a photon with higher frequency $\omega_1 = \omega_0 + \omega_m$ by absorbing the phonon at ω_m. These two processes are called Stokes- and anti-Stokes-process. In the Stokes-process the optical system transfers energy into the mechanical resonator by amplifying the mechanical mode. In the anti-Stokes-process the optical system takes energy from the mechanical resonator by damping the mechanical mode. These two processes create an upper and lower sideband around the angular frequency ω_0 of the fundamental optical mode. In a cavity, the two higher-order optical modes corresponding to the two sidebands will experience different gains and have different mode shapes.

If the fundamental cavity mode and the higher-order mode resulting from the

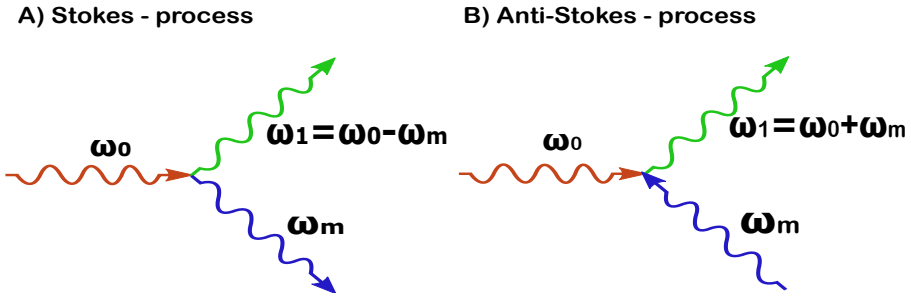

Fig. 2.1: Schematic diagram of three-mode optomechanical interaction described as a scattering process. A) In the Stokes-process a photon with angular frequency ω_0 creates a phonon in the mechanical resonator with angular frequency ω_m and a photon with lower frequency $\omega_1 = \omega_0 - \omega_m$. B) In the Anti-Stokes-Process the photon of the fundamental angular frequency ω_0 creates a photon with higher angular frequency $\omega 1 = \omega_0 + \omega_m$ by absorbing a photon at ω_m of the mechanical resonator.

Stokes-process are resonant in the cavity and the mechanical mode ω_m is resonant in the mirror and these three modes fulfill the condition,

$$\omega_0 \simeq \omega_1 + \omega_m \tag{2.1}$$

an instability can arise when the spatial overlap of the mechanical mode shape with the optical beat note is high enough. This optomechanical phenomenon can also be understood as a classical feedback effect that has been described by Evans et al. in [49] together with a schematic diagram shown in figure 2.2: The optical beat note at $\omega_0 - \omega_1$ amplifies the mechanical mode ω_m via radiation pressure. In return the mechanical mode ω_m increases the amplitude of ω_1 in the cavity via scattering of the fundamental mode. Above a certain threshold, the amplitude of ω_m, as well as the amplitude of ω_1 in the cavity will rise exponentially.

The threshold depends on several quantities that will be discussed in the next section.

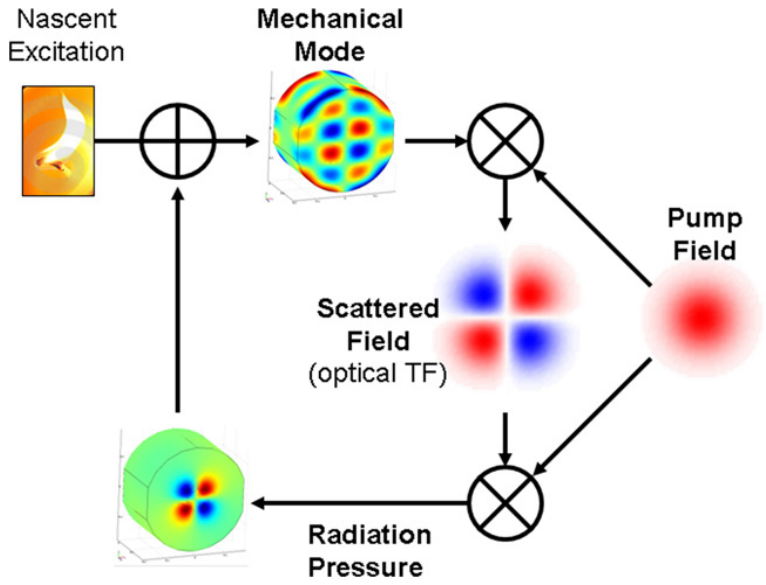

Fig. 2.2: Schematic of the parametric instability seen as a feedback loop. By nascent excitation of the cavity mirror a mechanical eigenmode at ω_m can be excited. A part of the fundamental optical mode at ω_0 (pump field) can be transferred by scattering at the mirror into a higher-order resonant optical mode ω_1 (scattered field $\widehat{=}Re[G_n]$ in equation 2.2). The beat note of the fundamental and the higher-order optical mode amplify the mechanical eigenmode of the mirror via radiation pressure. (figure taken from [49])

2.3 Parametric Gain

The parametric instability process can be quantified by a single value, the parametric gain. Evans et al. derived the parametric gain in 2010 by treating PI as a classical feedback problem [49]: By assuming that only a single mechanical mode of a single test mass in the cavity contributes to PI, they obtain the following expression for the parametric gain R_m by taking the real part of the open loop gain [49, 46]:

$$R_m = \frac{8\pi Q_m P}{M w_m^2 c \lambda_0} \sum_{n=1}^{\infty} Re[G_n] B_{m,n}^2 \tag{2.2}$$

Q_m is the quality factor of the mechanical eigenmode m with the angular frequency ω_m, P the circulating power in the fundamental cavity mode with wavelength λ_0, M the mass of the test mass and c the speed of light. The second term in the formula takes into account the sum of the optical modes n interacting with the mechanical mode m. G_n is the transfer function of the optical field n, leaving the test mass surface to the field incident on that surface after scattering. In a Fabry-Perot cavity, G_n is the cavity gain for the Stokes and anti-Stokes sideband field projected on the n^{th} cavity mode. $B_{m,n}$ is the geometrical overlap coefficient between the

surface deformation of the mechanical mode m and the optical beat note pressure distribution of the fundamental and higher-order optical mode n. $B_{m,n}$ is defined by the following integral over the mirror surface [49]:

$$B_{m,n} = \iint_{surface} f_0 f_n (\vec{u}_m \cdot \hat{z}) d\vec{r}_\perp \tag{2.3}$$

f_0 and f_n are the field distribution functions of the fundamental and the higher-order optical mode n, $\vec{u}_m$ the displacement function of the mechanical eigenmode and $\hat{z}$ the unit vector along the cavity direction.
R_m is the real part of the open loop gain. An instability occurs for $R_m > 1$ and optical damping for $R_m < 0$ [47, 49].
If a mechanical mode in a cavity becomes unstable with $R_m > 1$ its amplitude grows exponentially with a time constant τ_m [46]:

$$\tau_m = \frac{2Q_m}{\omega_m (R_m - 1)} \tag{2.4}$$

2.4 Observation of PI

Three-mode interaction in a large scale optical cavity was observed for the first time in 2008 in the High Power Test Facility [50] in Gingin, Western Australia [51, 52]. The parametric gain was below unity and proved the theory and model of parametric instability in high-power optical cavities. The first parametric instability was observed in 2009 by Grudinin et al. and Tomas et al. in solid state mm/µm-scale resonators [53, 54]. Two optical and one mechanical whispering gallery modes were responsible for PI. In both experiments a threshold power in the fundamental optical mode was necessary to observe this instability. This is in accordance with equation 2.2 which states that R_m is proportional to the optical power of the fundamental mode. Thus, if the optical power is sufficiently high an optical cavity can experience PI.
In a free-space cavity PI was observed for the first time in 2015 by Chen et al. [55]. A nano-gram membrane resonator was embedded in a high-finesse table-top cavity as coupling mirror between two cavities. By tuning the membrane position, PI was observed.
Its observation in the Advanced LIGO interferometer was published in the same year [46]. The frequency of the involved mechanical mode was identified as 15.54 kHz. Figure 2.3 shows the exponential growth of the unstable mechanical mode amplitude at the initial circulating power of 50 kW in the arm cavity. When the circulating power was reduced to 16 kW the amplitude decayed exponentially.
The observed instability caused the detection electronics to saturate. The time scale of the exponential growth with a time constant τ_m was of several minutes. This was

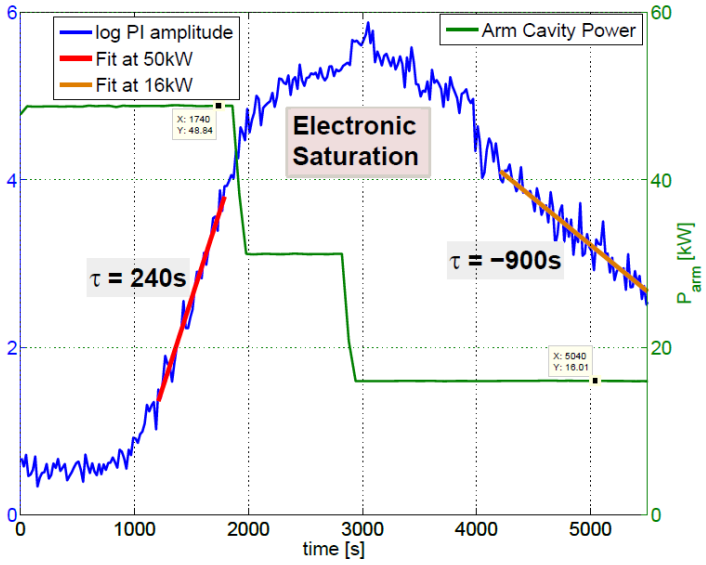

Fig. 2.3: First observation of PI in the Advanced LIGO interferometer. The logarithm of the amplitude of the unstable acoustic mode of 15.54 kHz is plotted in blue against the time. The circulating cavity arm power is shown in green. At an arm power of 50 kW the amplitude of the acoustic mode grows exponentially with an e-folding growth time $\tau_m = 240$ (fit in red). By reducing the arm power to 16 kW the amplitudes decays with $\tau_m = -900$ (brown fit). (figure taken from [46])

long enough to intervene manually in order to reduce the laser input power in the interferometer before its control was lost.
The measured time constant τ_m was used to calculate R_m=2 and the unstable mode quality factor of $Q_m = 1.2 \cdot 10^7$ based on equation 2.4.

2.5 PI mitigation strategies

PI sets an upper limit to the intra-cavity power in the arms, since the interferometer control is lost otherwise, as seen in the previous chapter. At the same time it is desirable to increase the intra-cavity power in order to increase the sensitivity of the detector. Thus, PI needs to be mitigated in order to prevent the loss of the interferometer control as well as to further increase the intra-cavity power.
Based on equation 2.2 one can think of several ways to prevent PI:

- **decreasing the intra-cavity power** P: This was done when the first PI occurred in the LIGO interferometer [46], but decreasing the intra-cavity power also results in a decrease of the detector's sensitivity.

- **decreasing the quality factor** Q_m **of unstable mechanical modes**: It can be achieved by damping these modes [56, 57]. One could also choose a

mirror material with lower mechanical mode quality factors, but it is not worth considering, since it will increase the thermal noise in the detector.

- **increasing cavity mirror mass** M: This is planned for Advanced Virgo for the Observation Run 5 [7] as well as for third generation detectors [5, 43].

- **using a laser with a higher wavelength** λ_0: It is not realistic since such lasers with the required optical power and low noise are not available. It would also mean that new optics with new coatings would be needed which are likewise not available.

- **changing the transfer coefficient** G_n : It can be achieved by changing the radius of curvature [58] of the mirror surface or its shape [59, 60, 61] to decrease the gain of higher-order optical modes in the cavity which are responsible for PI .

To summarize, strategies in order to prevent PI without decreasing the sensitivity of the detector consist either in decreasing the quality factor Q_m of unstable mechanical modes, or by decreasing G_n.
An overview of investigated strategies is presented in the next section.

2.5.1 Overview

Since the first description of PI in Gravitational Wave detectors by Braginsky in 2001 [47], several strategies to mitigate it were proposed. An overview of some proposed strategies can be found in [62].

Several active and passive strategies were presented aiming to decrease Q_m:
Passive strategies aim to change the cavity properties to prevent PI. Examples are studies of alternative test mass materials for Advanced GW detectors such as sapphire with lower acoustic mode densities instead of fused silica, which was presented in 2005 [63, 64]. In 2008, test mass ring dampers were proposed [65, 66]. Another type of dampers was demonstrated to be effective in Advanced LIGO-like test masses in 2015 [56]: resonant acoustic dampers, which have been implemented in the Advanced LIGO interferomter [67]. They were designed to reduce the Q-factor of potentially unstable test mass acoustic modes without a significant increase of thermal noise. Theoretical investigations have also been done to use rotative non-linear vibration absorbers that do not have a preferential suppression frequency [68].
In contrast to these approaches, active strategies actually sense the rise of PI in the cavity and damp it in a feedback: Braginsky proposed using the body of the test mass itself as additional Fabry-Perot cavity and pumping it by an external laser to

tranquilize PI based on dynamic back action [69]. This method was shown in [70] to be working in principle, but technically difficult to use in current GW detectors. In 2009 Ju et al. proposed in [62] using the direct radiation pressure of a laser beam to control PI. The damping force adds dissipation to the unstable mechanical mode and decreases in this way its effective quality factor. Blair stated in [4] that a laser source of 10 W per test mass would be required.
In the Gingin test facility an active strategy was investigated by damping unstable mechanical modes via optical feedback control with theoretical investigations demonstrated in [71] and experimental results in [72]. In this experiment a higher-order mode at ω_1 is injected out-of-phase into the cavity to mitigate PI. An active strategy that was tested in the LIGO interferometer was the damping of unstable mechanical modes via electrostatic actuation [73].

There were also several strategies presented that change G_n:
The fine tuning of the test mass radii of curvature was proposed in 2005 [74, 58] and experimentally demonstrated in the Gingin test facility as an effective strategy to tune the cavity away from instability in 2012 [75]. Theoretical investigations have been done to change the mirror surface shape in order to increase the round-trip losses of higher-order optical modes [59, 60, 61]. These mirrors would require a tighter mirror tilt stability though. It has also been proposed and investigated that thermal modulation of the test mass would prevent unstable mechanical modes rising exponentially [76, 77]. Moreover, Hardwick et al. demonstrated in 2020 that the thermal compensation of Advanced LIGO test masses has to be done dynamically in order to avoid instability of the 15 and 15.54 kHz mechanical modes at 170 kW intra-cavity power [78]. Zhang et al. did a study on the design of future GW detectors, which are PI-free with up to 3 MW optical intra-cavity power, by choosing carefully the cavity lengths, the test mass design and its radii of curvature [79].

In the next three sections I will present the strategies that have already been applied in Advanced Gravitational Wave Detectors.

2.5.2 Thermal Tuning

With first simulations C. Zhang et al. showed that by changing the radius of curvature of the cavity mirrors by thermal actuation, the cavity could be tuned to minimize the parametric gain [74]. J.Degallaix provided further simulations and proved the effectiveness of this approach to prevent instability of the cavity [58]. Shortly after the first observation of PI in the LIGO interferometers this method was applied to reduce the parametric gain under unity for the observed instability of 15.54 kHz [46]. Ring heaters were used for this purpose. As depicted in fig.2.4 ring heaters surround each test mass without physical contact and were designed to

compensate the radius of curvature change of the test masses due to absorption (Thermal Compensation System [80]). By changing the radius of curvature the optical beat note of the fundamental mode at ω_0 and higher-order optical mode at ω_1, which are involved in PI, is tuned out of the resonance condition (see equation 2.1) to stop the amplification of the unstable mechanical test mass mode at ω_m. Figure 2.5 shows the $\mathrm{TEM}_{00}\mathrm{TEM}_{03}$ beat note peak (Transverse Electromagnetic Mode) tuned in order to decrease the parametric gain below 1.
Since the Advanced GW detector test masses have a high density of acoustic modes, the detuning of one unstable mode can bring other acoustic modes to resonance [67]. The high density of acoustic modes combined with the fact that the intra-cavity power for the Advanced GW detector will be increased towards 1MW shows that this method will not be sufficient to prevent PI.

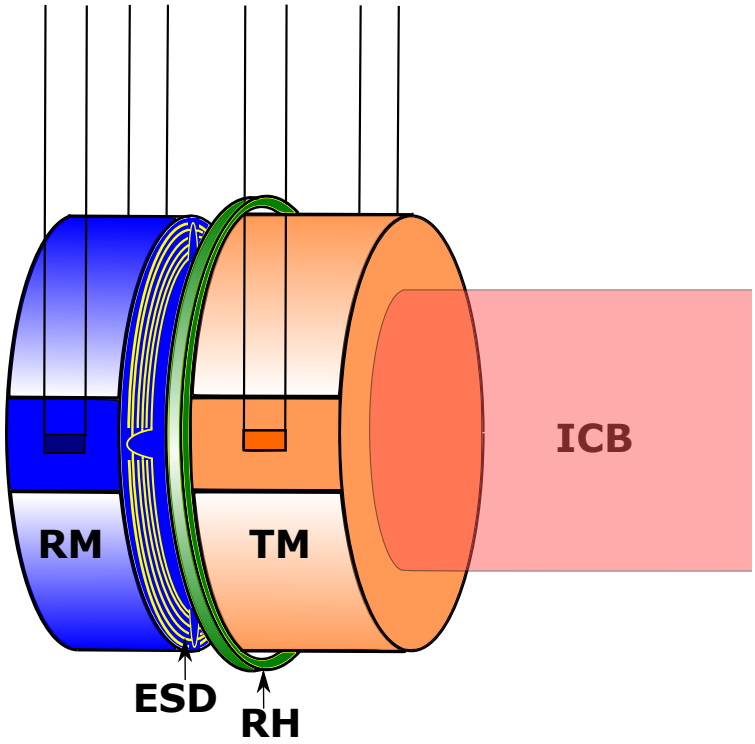

Fig. 2.4: Schematic of the suspended end test mass (TM) with the intra-cavity laser beam (ICB) and a ring heater (RH) as thermal actuator to change the radius of curvature of the TM. The reaction mass (RM) is also suspended and has four electrode combs of gold for the electrostatic drive (ESD). It provides longitudinal actuation on the TM. (figure based on fig.1 of [57])

2.5.3 Acoustic mode dampers

Another approach to prevent PI consists in damping the mechanical Q-factor of unstable modes passively. Metal rings (ring dampers) and coatings on the circumference of the test mass were investigated to decrease the Q-factor of acoustic modes of the test mass [65, 66]. But they only achieved sufficient damping by increasing the thermal noise significantly. The challenge of this approach is to provide good

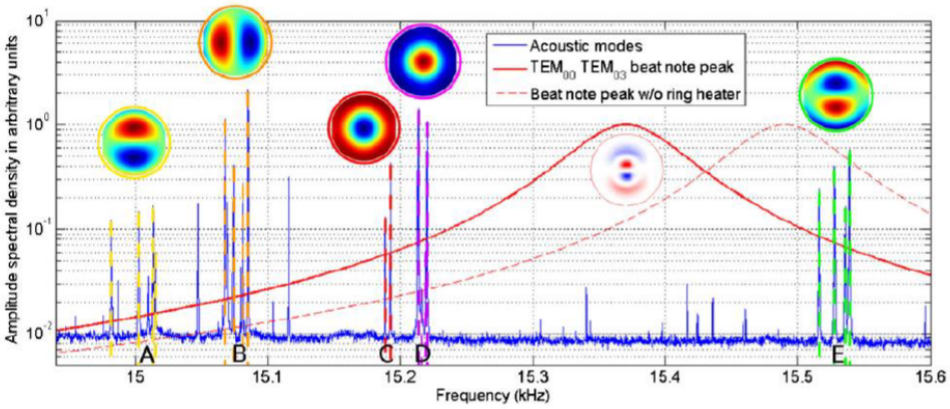

Fig. 2.5: The amplitude spectral density of different groups (A-E) of mechanical modes in the LIGO interferometer during O1 when the first PI was observed at 15,53kHz (E) are displayed. The corresponding mode shape simulation is shown on top of each group (inset). The $\mathrm{TEM}_{00}\mathrm{TEM}_{03}$ beat note peak (Transverse Electromagnetic Mode) is shown before thermal tuning was applied (red straight line). The beat note peak after thermal tuning is also shown (red dashed line), which was tuned to prevent PI. (figure taken from [4])

damping in the acoustic mode range (15-80 kHz) without a significant increase of thermal noise of the test mass below 100 Hz. Another solution is tuned dampers, known as acoustic mode dampers (AMD), which were investigated by Gras et al.[56] and optimized by Biscans et al.[67]. They are composed in principal of 3 components, as one can see in fig.2.6: a base that is attached to the test mass, a reaction mass and a piezoelectric plate between the base and the reaction mass. Epoxies are used for the assembly of the AMD and as the bond between the reaction mass and the AMD. The piezoelectric plate is orientated perpendicular to the cavity axis to limit the thermal noise injection into the cavity [67]. It is shunted with a resistor in order to convert the mechanical energy into electrical energy. The loss due to resistor shunting depends on the mechanical mode frequency and can be tuned by the resistor. The ensemble of the test mass and an AMD can be modelled as a coupled oscillator connected with a lossy spring. With 4 different AMD attached on each of the four test masses of the LIGO interferometer, no PI was observed except for a 10 kHz and 15kHz acoustic mode at an arm power level of 230 kW during O3 with a thermal noise degradation of at maximum 1% [67].

The simulation of Biscans et al. in Figure 2.7 shows that at design arm power of 750 kW in the LIGO interferometer the parametric gain of all acoustic modes from 15 kHz on should be decreased under unity with these four AMD attached on each test mass.

Next generation detectors are designed to increase their sensitivity by a factor of 10 with higher optical power in their cavities [5, 43]. Thus, more unstable modes are expected and stronger requirements on thermal noise are needed.

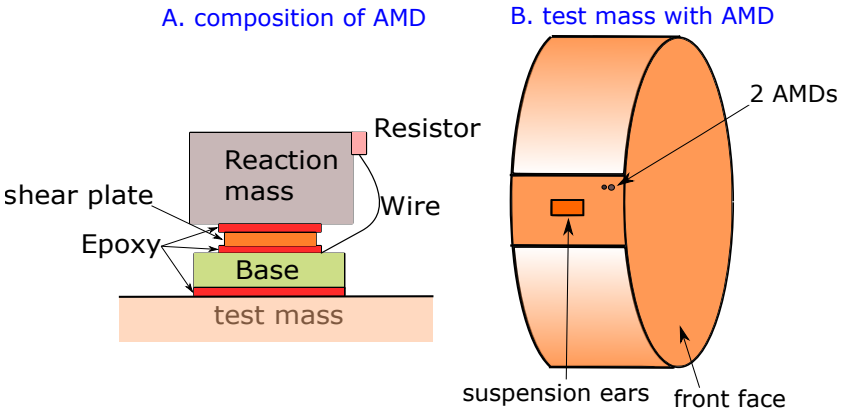

Fig. 2.6: Schematic of AMD. (A) Composition of AMD. The dimensions vary from the 4 designed AMD for each test mass of the LIGO interferometer. (B) A model of one test mass with two little AMD attached to the test mass. (figure based on fig.1 in [67])

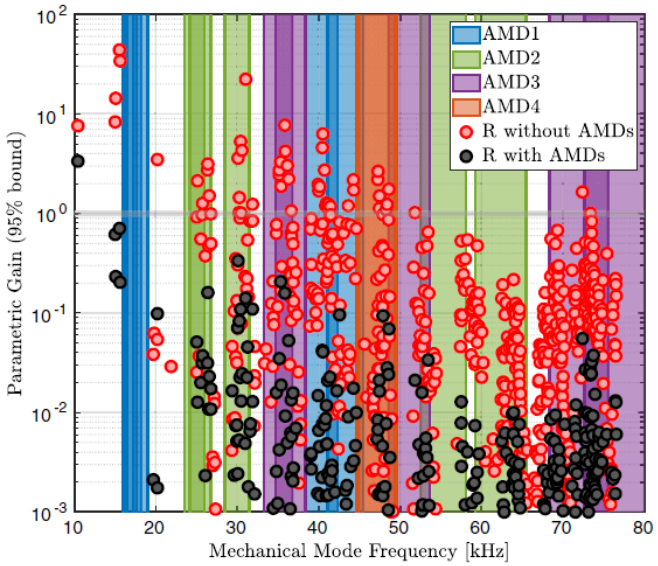

Fig. 2.7: Simulation of parametric gain with and without AMDs for one test mass of the LIGO interferometer for 750 kW circulating power in the arms. The frequency band for which each AMD is designed is shown. (figure taken from [67])

2.5.4 Electrostatic Actuators

Figure 2.4 shows electrode pairs in form of gold stripes deposited on the reaction mass. In Advanced LIGO each reaction mass has four of these electrode combs symmetrically ordered to control the position of the suspended test masses with a spacing of 5 mm between the two masses: A potential difference between the electrodes induces an electrostatic field that attracts the dielectric test mass. The control of PI with electrostatic forces was first proposed in [62] and Miller et al. studied in [73] the effectiveness of using the ESD in LIGO for this purpose. The idea of this approach is to add a dissipation to the unstable mechanical mode with a damping force. In this way the effective quality factor of the mechanical mode is decreased as discussed in greater detail in chapter 3.2.
Miller et al. estimated the required damping force and stated that this scheme does not introduce any thermal noise.

Successful damping of an unstable mode group at 15.54kHz in Advanced LIGO was reported in [57]. The unstable mode with a parametric gain of R = 2.4 was successfully damped to a gain of R = 0.18 with ESD forces. A damping force of 0.03 nN rms was needed to keep the mode damped. The required force was 10 times smaller than the required force predicted by Miller et al. [57]. No significant noise coupling into the main interferometer output was measured.
But ESD consist only of 4 actuators with fixed positions on the reaction mass. It means that this scheme cannot damp any mode efficiently, since the overlap of the created damping force field with the mechanical mode shape needs to be significant. Additionally, PI damping with ESD requires an individual control loop for each mode [61]. Thus, the complexity rises if PI involving different unstable modes should be controlled.

2.6 Conclusion

Parametric Instability is a nonlinear optomechanical phenomenon limiting the sensitivity of Advanced GW detectors by setting an upper limit for the circulating power in their arm cavities. Since its prediction as limiting factor of intra-cavity power in 2001, several PI mitigation strategies were proposed. These strategies focus either on reducing the mechanical quality factor of unstable cavity mirror eigenmodes, or on reducing the amplitude of resonant optical higher-order modes in the cavity responsible for PI. In 2014 PI was observed for the first time in the LIGO interferometer, causing the detection electronics to saturate. By changing the radius of curvature of the cavity mirrors, the parametric gain of the unstable mirror eigenmode of 15.54 kHz could be reduced below unity (thermal tuning). Due to the high density of

mechanical modes in the fused silica test masses, other modes can get unstable by tuning the beat note of the fundamental and higher-order optical mode. For this reason acoustic mode dampers were additionally attached to the LIGO test masses in order to decrease the Q-factor of unstable mechanical modes. But these dampers increased the thermal noise level of the detector by less than 1%. Active damping of the unstable mechanical mode at 15.54 kHz has been demonstrated with ESD. Since ESD consists only of 4 electrode combs it can only apply forces with a limited overlap with possibly unstable higher-order mechanical modes.

In order to increase the sensitivity of future GW detectors, it is crucial to develop PI mitigation strategies that are flexible and effective without increasing the noise level of the detector. A scheme using the radiation pressure force of a laser to damp unstable mechanical modes as proposed in [62, 4], is promising. We propose to rapidly deflect the damping beam in order to be flexible and to damp modes with arbitrary shapes with a high overlap. In the next chapters such a system is presented. First experimental results are presented on the way towards PI mitigation in GW detector interferometers based on radiation pressure of a movable laser beam.

3 Concept of active PI mitigation strategy based on radiation pressure

3.1 Introduction

We propose a flexible active PI mitigation strategy based on radiation pressure. Its principle is depicted in Figure 3.1 and a first presentation of this concept can be found in [81]. The GW detector interferometers have a Fabry-Perot cavity in each arm consisting of mirrors M1 + M2 and M3 + M4. Each of these cavities can host PI involving unstable mechanical modes on each of the mirrors. Our strategy consists in damping the rising mechanical mirror mode due to PI via a radiation pressure force applied by a small and movable auxiliary laser beam. The beam is injected at the backside of the mirror M1 and M3 and reflected on its high reflectivity coating. To inject no noise, the wavelength of the auxiliary laser should be chosen in such a way that it does not resonate in the cavity. Nonetheless, the laser beam should be reflected by the coatings of the mirror. The small laser beam is deflected rapidly to address different lobes of the mechanical mode shape during one period.
If a mechanical mode in the end mirrors M1 and M4 becomes unstable due to PI, the auxiliary laser beam can damp this mode directly. Moreover, we expect to mitigate PI also involving the input mirrors M2 and M4: it has been experimentally demonstrated in [82] that PI can be generated by introducing a higher-order optical mode into the cavity. PI has also been damped by modulating the frequency of the higher-oder mode in [83]. Using the auxiliary laser beam, the surface of M1 and M3 can be reshaped to generate a frequency-modulated higher-order mode by scattering of the intra-cavity fundamental mode. Properly reshaping the mirror surface can also scatter the higher-order mode involved in PI into a non-resonant optical mode. Depending on the cavity configuration and the considered PI, one of these two optical mitigation methods can be used.
In order to monitor the mechanical mode shape of unstable modes on the mirror, the same laser beam can be used as discussed in detail in chapter 5.

In this chapter our active damping strategy based on radiation pressure is presented. A first approximation of the necessary laser power is derived based on the equation of

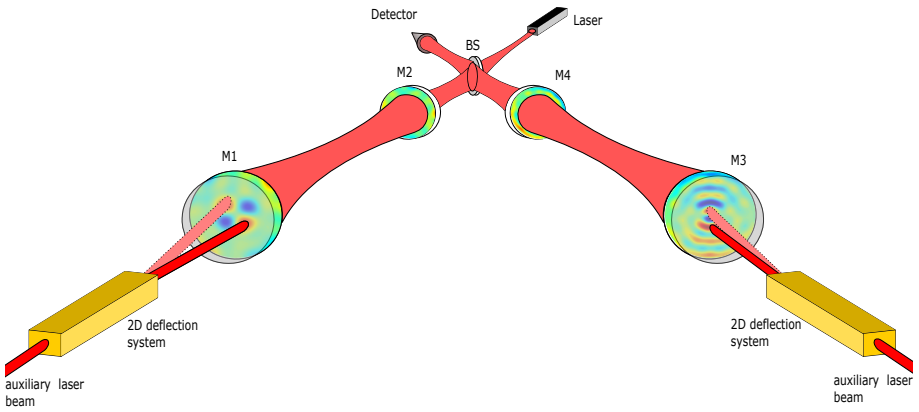

Fig. 3.1: Schematic of the PI mitigation strategy based on radiation pressure. The input laser is split with a beam splitter (BS) into two arms. Each arm of a gravitational wave detector interferometer contains a Fabry-Perot cavity consisting of mirrors M1 + M2 and M3 + M4 . Arising PI will be damped via radiation pressure by reflecting an auxiliary small beam at the highly reflective coating of mirror M1 and M3. The auxiliary beam will be deflected with a fast 2D deflection system to address the different lobes of the growing mechanical eigenmodes of the mirror.

motion in section 3.2. Section 3.3 discusses possible mechanisms of noise coupling of the damping system into the interferometer. In section 3.4 possible damping schemes of unstable acoustic modes are presented. Some considerations are presented that need to be taken into account when choosing an appropriate damping pattern for an unstable mode. This chapter is concluded in section 3.5 by summarizing the requirements for a 2D deflection system used for active PI mitigation.

3.2 Theory

Each mirror of the Fabry-Perot cavity is effectively a solid cylinder with internal eigenmodes. An eigenmode can be modeled by a damped harmonic oscillator. If a radiation pressure force F_{rad} is applied to the mirror the equation of motion is given by

$$\mu_m \ddot{x} + \frac{\omega_m}{Q_m} \mu_m \dot{x} + k_m x - F_{rad} = 0 \tag{3.1}$$

with x, the amplitude of the acoustic mode, μ_m, the mass of the mirror that contributes to the motion, ω_m, an angular eigenfrequency, Q_m the quality factor of this eigenmode and k_m the spring constant of the mirror. Assuming a viscous damping force $F_{rad} = K_m \dot{x}$, with K_m the viscous damping constant we can write

$$\mu_m \ddot{x} + \frac{\omega_m}{Q_{eff}} \mu_m \dot{x} + k_m x = 0 \tag{3.2}$$

by defining an effective quality factor Q_{eff}, as demonstrated in [73] by

$$Q_{eff} = \left(\frac{1}{Q_m} + \frac{K_m}{\omega_m \mu_m} \right)^{-1} \tag{3.3}$$

Thus, by applying a viscous damping force, the quality factor of unstable mirror modes is reduced. This damping force is proportional to the velocity of the mirror displacement. That means, when pointing on one lobe of an unstable eigenmode, the optical power should be modulated with the frequency of the eigenmode but with a phase shift of $90°$.
For a thermally excited mechanical mode, the one-dimensional amplitude x in RMS can be derived from the equipartition theorem as [73]

$$x = \sqrt{\frac{\kappa_B T}{\mu_m \omega_m^2}} \tag{3.4}$$

with the Boltzmann constant κ_B and the mirror temperature T.
In order to reduce the quality factor of a thermally excited unstable mode Q_m to Q_{eff}, the required damping force F_{rad} can be calculated. The RMS-magnitude of F_{rad} can be expressed as

$$F_{rad} = x \omega_m^2 \mu_m \left(\frac{1}{Q_m} - \frac{1}{Q_{eff}} \right) \tag{3.5}$$

in analogy to the derived expression for the required force of ESD [73].
One needs to keep in mind that the derived force F_{rad} is based on a simplified model. It does not take into account the radiation pressure force amplifying the eigenmode due to PI. In [57] the required electrostatic force to damp an unstable mechanical mode in the test mass has been measured to be ten times smaller than the predicted force based on equation 3.5.
Equation 3.5 is used, though, to approximate the required damping force. The auxiliary laser power P, which is needed to reduce the quality factor of a mirror oscillation, can be estimated based on the same equation. It is useful to introduce an overlap coefficient b_m, representing the spatial overlap of the exerted radiation pressure force distribution with the mechanical mode shape. Thus, the final required radiation pressure force is a portion of the total radiation pressure F_0, delivered by the laser beam with $F_{rad} = b_m F_0$. Assuming an unstable mirror mode, which has an amplitude n times higher than in thermal equilibrium, P equals

$$P = \frac{n c F_{rad}}{2} \frac{1}{b_m} = \frac{n \omega_m c \sqrt{\mu_m \kappa_B T}}{2 Q_{eff}} \frac{1}{b_m} \tag{3.6}$$

neglecting $\frac{1}{Q_m}$ in eq. 3.5 as $\frac{1}{Q_{eff}} \gg \frac{1}{Q_m}$. Figure 3.2 displays a plot based on equation 3.6 of the required laser power to damp modes of a GW test mass for frequencies in the range from 10 to 200 kHz. Assuming values from current gravitational wave

detectors [62, 4] with $\mu_m = 10$ kg, $Q_{eff} = 10^5$ and $T = 300$ K, the required laser power for $n = 5, 10$ and $b_m = 0.2, 1$ is plotted. It can be seen that a laser beam with

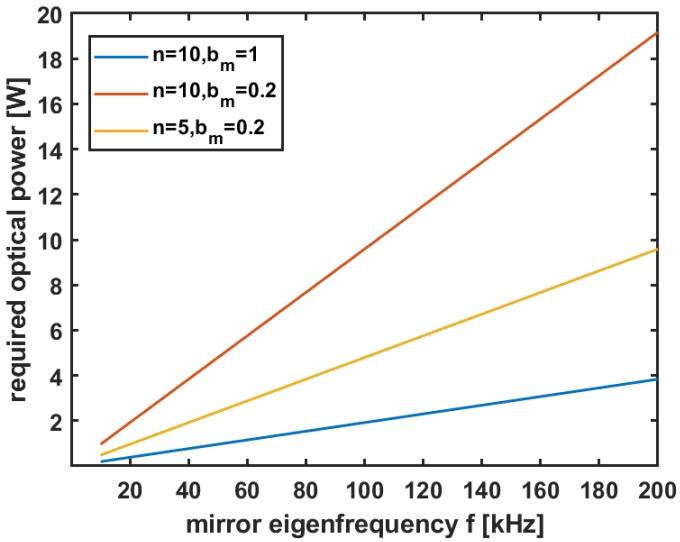

Fig. 3.2: Simulation of required optical power to damp mechanical modes as function of the test mass eigenfrequency. It is done based on equation 3.6 for current GW detector test masses with $\mu_m = 10$ kg, $Q_{eff} = 10^5$ and $T = 300$ K for $n = 5, 10$ and $b_m = 0.2, 1$.

an optical power of several Watts should be sufficient to actively damp unstable mechanical modes of the test masses of gravitational wave detectors.
Since the auxiliary laser beam will change its position on the mirror, the overlap coefficient b_m does not only include the spatial distribution of the applied force, but it has also a temporal dimension and will be smaller than 1. In order to optimize this damping strategy the scan pattern of the laser beam on the mirror should be chosen in such a way as to obtain a b_m as close as possible to 1.
The observed time constants of acoustic modes involved in PI were measured to be between 50 ms and several hundreds of seconds [62]. Consequently, if the rising mechanical modes of the mirror can be detected and damped before its amplitude rises significantly, then even smaller forces should be sufficient. Thus, a reliable and precise method of acoustic mode shape sensing is necessary for our active damping strategy of PI based on radiation pressure.

3.3 Noise coupling

Since we will apply radiation pressure on the coating of the test masses of the detector, noise coupling into the interferometer needs to be considered. It is important to state that the beam will only apply radiation pressure when PI arises. Since the auxiliary laser beam is reflected off the high reflectivity coating of the cavity

mirror, no significant coupling of the laser beam into the cavity is expected. The transmission coefficient of the end test mass of Advanced Virgo is for example 1 ppm [26]. For an auxiliary laser beam of 10 W there would be still 10 μW of the beam entering the cavity. For this reason the wavelength of the auxiliary laser should be chosen in such a way that the entering beam is not resonant in the cavity. It might be necessary to lock the auxiliary laser wavelength to the main interferometer laser wavelength. In this way it will not be amplified and it can be filtered out. The intensity noise of the auxiliary laser, though, could be converted into displacement noise Δz_n of the interferometer mirrors via radiation pressure [84, 85]:

$$\Delta z_n = \frac{2P}{mc(2\pi f_n)^2}\mathrm{RIN} \tag{3.7}$$

RIN is the relative intensity noise of the laser, P the optical power of the beam pointing on the mirror with mass m and f_n is the frequency of the noise.
If the requirement of the intensity noise contribution to the detector sensitivity is set to 10 %, as it is set for the photon calibrators in LIGO and Virgo [86, 85], the RIN of the auxiliary laser can be estimated. For Advanced Virgo, with $m = 40$ kg, a cavity arm length of $L = 3$ km and a strain sensitivity of $h = 5 \cdot 10^{-24}\frac{1}{\sqrt{\mathrm{Hz}}}$ for $f_n = 100$ Hz, the maximal RIN at an average optical power of $P = 10$ W should be

$$RIN \leq \frac{hLmc(2\pi f_n)^2}{20P} \leq 4 \cdot 10^{-7}\frac{1}{\sqrt{\mathrm{Hz}}} \tag{3.8}$$

This specification is similar to the one obtained for the RIN of the photon calibrator lasers [86, 85], thus an auxiliary laser with such a RIN would be sufficient.

The amplitude modulation of the auxiliary laser beam at the frequency of the unstable mechanical mode and residual amplitude modulations due to the deflection rate of the laser beam are at high frequencies above the detection band of the interferometer.
Thus, no significant noise coupling into the detection band of the GW detector is expected with this active PI mitigation strategy, if a laser with low RIN is used.

3.4 Considerations for a damping pattern

There are numerous scan patterns which could be employed to damp an acoustic eigenmode of a large mirror with the radiation pressure of a laser beam.
Figure 3.3 shows six simulated mode shapes of eigenmodes of the Advanced Virgo test masses. It shows the mirror surface displacement perpendicular to the page. The plots are ordered by their frequency from 5 to 63 kHz. It can be seen that with

increasing eigenmode frequency the mode shape gets more complex and has smaller lobes.

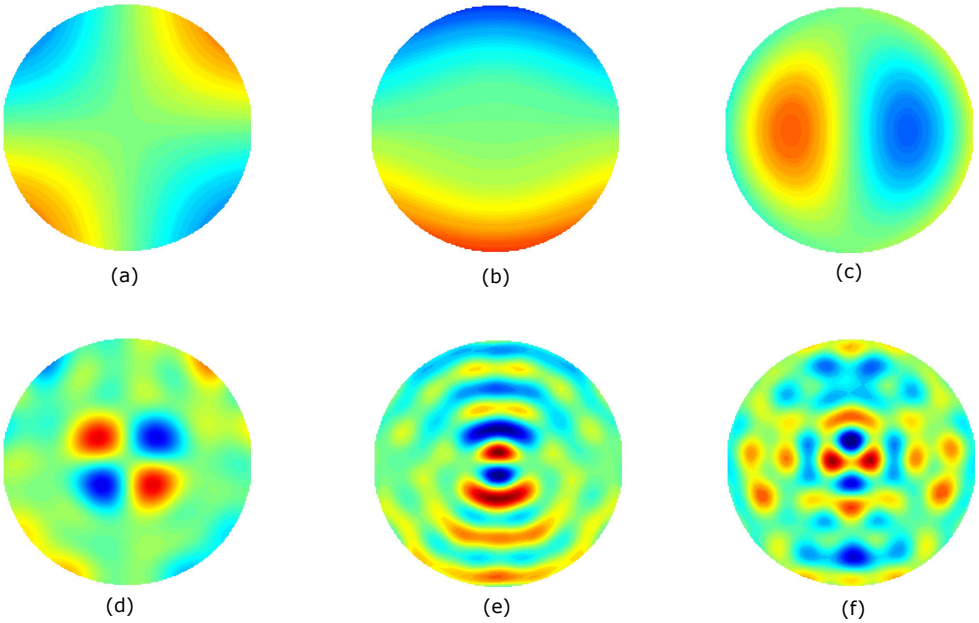

Fig. 3.3: Simulated mode shape of 6 eigenmodes of the Advanced Virgo test masses ordered by frequency from 5-63 kHz. The deformation of the surface is perpendicular to the page. Red represents a deformation out of the page and blue a deformation into the page.

In order to find the optimal method to damp unstable modes with shapes like the ones depicted in figure 3.3 a numerical model needs to be developed. This model should include the rise of PI in a cavity combined with the application of local viscous damping forces on a cavity mirror. Some consideration concerning possible scan patterns are given in this section.

3.4.1 One-directional radiation pressure force

The laser beam can only apply a force in one direction by pushing the mirror (let us define a negative sign for this direction). There are various damping approaches that can be considered. In figure 3.4 two damping schemes are presented with a force that has a phase shift of $\pi/2$ to the mirror displacement:
On the one hand one could apply a damping force on a lobe of a mechanical mode only when its surface displacement velocity is positive. So for a mechanical drum mode with a mode shape depicted in figure 3.4 (inset), a damping force during maximal half the period of the mechanical mode frequency can be applied. For mode shapes with several lobes (see figure 3.3) the laser beam could switch its position between lobes which are in phase and in anti-phase in order to damp during the whole period of the unstable acoustic mode frequency. It should be noted that for

this case the derived damping force in section 3.2 is not valid, since the damping force is nonlinear.
On the other hand an offset radiation pressure force can be added (figure 3.4B). In this way the laser beam can damp any lobe of a mechanical mode at any time. This means that the mirror position would have to be corrected as the auxiliary laser applies a DC force on the mirror.

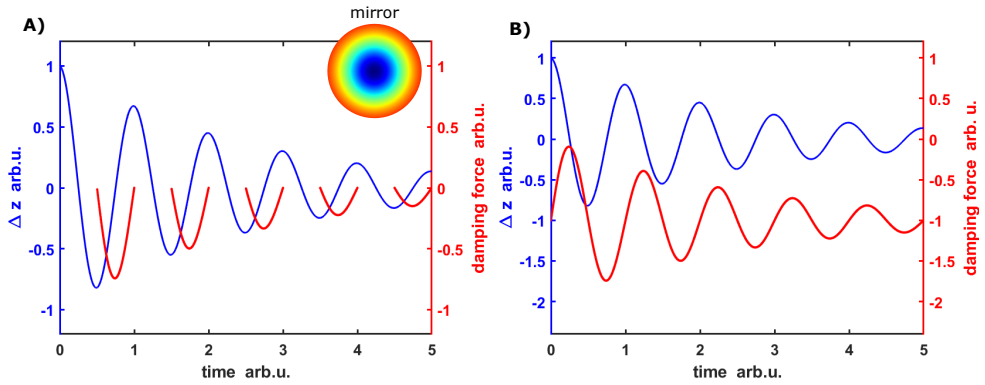

Fig. 3.4: Principle of viscous damping force application with a small laser beam on the center of an unstable mechanical drum mode of the cavity mirror (inset). A) Modulated damping force only during half of the mode period with surface displacement Δz of the mirror. B) Modulated damping force during the whole mode period with an offset of -1. (both damping forces and Δz are normalized)

3.4.2 Overlap of the auxiliary laser beam shape and the mechanical mode shape

In order to damp efficiently a rising mechanical mirror mode, the overlap between the spatially applied damping force and the mode shape should be high. Since the movable laser beam is acting on different positions on the mirror, the overlap factor has also a temporal component. To calculate the overlap factor b_m of the laser beam shape with the mechanical mode shape the following expression is used adapted from [48]:

$$b_m = \sum_i^N o_i \frac{t_w\, n_p}{T_m} = \sum_i^N \frac{V(\int f_L(\vec{u}_\perp) u_z d\vec{r}_\perp)^2}{\int |f_L|^2 d\vec{r}_\perp \int |\vec{u}|^2 dV} \frac{t_w\, n_p}{T_m} \tag{3.9}$$

o_i is the overlap factor of the laser beam shape with the mechanical mirror mode shape when radiation pressure is exerted at a distinct position of the mirror. N is the number of addressed mirror positions with the laser beam, t_w the duration that the laser stays on a mirror position, T_m the period of the mechanical mode frequency and n_p the amount a given scan pattern of the laser beam is repeated during one mechanical mode period. f_L is the optical field distribution over the mirror surface. Vector $\vec{u}$ is the spatial vector of displacement in the mirror mode, u_z is the component of $\vec{u}$, normal to the mirror surface, $\int d\vec{r}_\perp$ corresponds to the integration over the mirror surface and $\int dV$ over the mirror volume V.

Figure 3.5 shows three simulated eigenmode shapes of the Advanced Virgo test masses taken from figure 3.3. Possible scan patterns with a laser beam that has a Gaussian beam profile are added. A laser $\frac{1}{e^2}$-beam diameter of $\frac{1}{6}$ of the mirror diameter is assumed. It corresponds to the obtained resolution of the beam deflection system presented in the following chapter. The beam is depicted as black dashed circles filled with red. An overlap coefficient is calculated for each pattern for n_p=1 and a constant t_w so that the beam stays on each position for a duration equal to the period of the eigenmode frequency divided by the number of beam positions ($t_w = \frac{T_m}{N}$). Each beam position is chosen in such a way that the center of the Gaussian laser beam profile points at the position of the lobe with the maximal amplitude.

It can be seen that b_m is the highest with a value of 0.16 for the scan pattern depicted in figure 3.5B) since the addressed lobe shape has a similar size with the laser beam. In order to increase the overlap coefficient it would be optimal to adapt the beam size according to the addressed lobe size which is difficult to realize. It would also be possible to point on several positions of the lobes depicted in plot A), but a complete model describing the impact of locally applied damping forces on an unstable mirror mode due to PI is necessary to demonstrate which damping pattern is the most efficient one.

Since the size of the lobes decreases with an increasing eigenmode frequency (see figure 3.5C + D and figure 3.3) it is desirable to have a small laser spot which does not cover several lobes of a mode shape. In figure 3.5C + D) it can be seen that the laser beam covers partially the lobes which are in anti-phase. This does not only decrease the overlap coefficient as already mentioned but will decrease also the efficiency of the applied damping force since the applied radiation pressure force is partially not applied in the correct phase. The difference of the overlap factor for the two demonstrated patterns in plot C (b_m=0.08) and D (b_m=0.05) is due to the fact that the overlap o_i of the laser beam and the two lobes in the center is lower than o_i for the two outer addressed lobes.

Thus, the overlap factor b_m is larger when only lobes that have a high overlap o_i with the laser beam are addressed.

3.4.3 Commutation time of the laser beam

Another possible pattern would be to scan the whole mirror with a locally adapted radiation pressure. The demonstrated scan pattern in the previous section could also be applied several times during one period T_m, so that n_p>1. This implies that the beams stay shorter on each position if the duration t_w is chosen to be equal for each mirror position as $t_w = \frac{T}{Nn_p}$. Since it takes some time to change the beam position, this commutation time t_c, would accumulate so that the effective time the radiation

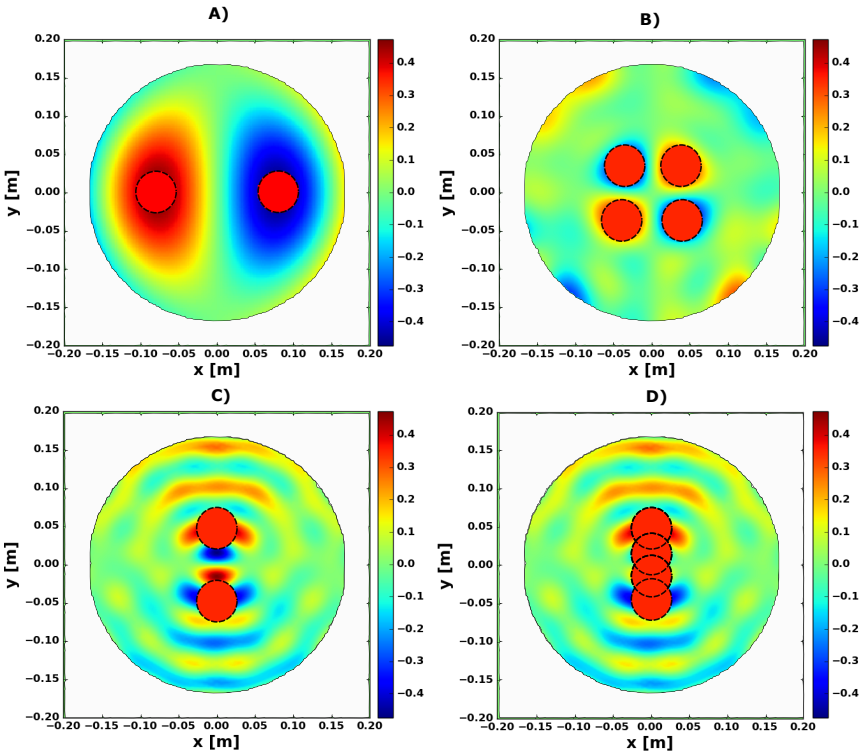

Fig. 3.5: Possible scan patterns with a laser beam diameter of $\frac{1}{6}$ of the mirror radius (black dashed circle filled with red) to damp acoustic eigenmodes of the Virgo test masses (taken from figure 3.3). An overlap-factor b_m is calculated for each pattern for a Gaussian laser beam profile based on equation 3.9 with n_p=1 and t_w=const A) for a 14.7 kHz mode with b_m=0.10 B) for a 39.8 kHz mode with b_m=0.16 C) for a 60 kHz mode with b_m=0.08 D) for the same mode as C) with a different pattern with b_m=0.05.

pressure force is applied would decrease. Thus, the overlap factor b_m from equation 3.9 can be adapted to include the commutation time t_c:

$$b_m = \sum_i^N o_i \frac{t_w - (N n_p t_c)}{T_m} \tag{3.10}$$

From equation 3.10 results, that b_m decreases if the amount of addressed mirror positions N increases and or if the repetition coefficient n_p increases. The demonstrated scan pattern in figure 3.5B) has for instance an overlap coefficient of b_m=0.14 for n_p=10 compared to b_m=0.16 for n_p=1, taking $t_c = 50$ ns.
Consequently, regarding the effective time the radiation pressure force is applied, it is preferable to choose a limited number of N. In any case, a beam deflection system is required that has a commutation time far below the period of the unstable eigenmode frequency in order to point at several lobes of a mode shape during one period.

3.4.4 Symmetry of applied radiation pressure

When choosing the positions where radiation pressure should be applied, the overlap between eigenmode lobes and the Gaussian beam shape are not the only important issue to consider. The scan pattern should preferably also be symmetric. When damping a mechanical mode, as depicted in figure 3.6, the radiation pressure force averaged over the mode period is not applied symmetrically on the mirror. In fact, the scan pattern depicted in figure 3.6B) could tilt the mirror, since the radiation pressure force is localized on the center and on the top of the mirror surface. It should be kept in mind that even the scan pattern depicted in figure 3.5A) could excite torsional oscillations of the suspended mirror, when the radiation pressure force is exerted during one half of the period on the left lobe and during the other half of the period on the right lobe. These oscillations are at high frequency, though. The symmetry of the force-application points on the mirror, however, minimizes the rotation of the mirror.

For further investigations, it would be possible to simulate the effect of exciting torsional oscillations for different mode shapes with different scan patterns. And as a further step, a model needs to be developed describing the impact of a damping force on a large test mass with unstable eigenmodes due to PI. Such a model would also consider the coupling of the test mass with the optical modes in the cavity.

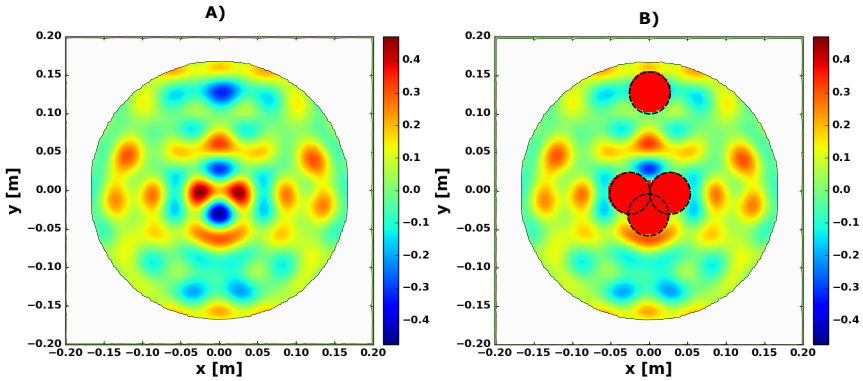

Fig. 3.6: A) A simulated Virgo test mass eigenmode shape with a frequency of 63.8 kHz B) with a possible scan pattern with a laser beam diameter of $\frac{1}{6}$ of the mirror radius (black dashed circle filled with red) to damp this eigenmode. Only lobes with a high overlap coefficient o_i are chosen for a Gaussian laser beam profile based on equation 3.9 with n_p=1 and t_w=const. obtaining b_m=0.06.

3.5 Conclusion

We propose an active PI mitigation technique based on radiation pressure provided by a small and movable laser beam. The required optical power of the laser beam has been estimated to be of several Watts. Unlike in the technique based on electro-static actuators [73], a large variety of modes can be damped since the force can be applied with a large overlap by the movable beam. The beam size should be chosen in such a way to damp unstable eigenmodes with small lobes in their mode shape (for high ω_m) as well as with large lobes (for low ω_m) with a significant overlap. It is necessary to monitor the rising of unstable acoustic modes to keep the required laser power low. The mode shape should be sensed to choose an adequate scan pattern for the auxiliary laser beam. Different scan patterns have been presented with some considerations which need to be taken into account. In order to find an optimal pattern a model needs to be developed describing the locally applied radiation pressure on a mirror with unstable eigenmodes due to PI.
Noise can be coupled into the interferometer by the conversion of intensity noise of the auxiliary laser beam into displacement noise of the mirror via radiation pressure. A laser with a power stabilization like the one used for current GW detectors, is sufficient to introduce no significant noise into the detection band.
In summary, a 2D beam deflection system is demanded with the following characteristics for the proposed PI mitigation technique:

- **high speed**: aiming at damping acoustic eigenmodes with frequencies ranging from tens to hundreds of kHz, the auxiliary laser beam should be deflected with a rate of some MHz to act on several lobes of the mode shape during one period of the highest mechanical mode frequency.

- **in random access**: in order to optimize the overall overlap of the exerted radiation pressure force and the mechanical mode shape, the beam deflection pattern should be easily adjustable.

- **high power**: the required damping force of some nN demands a deflected laser beam of several Watts.

- **large scan range with a small beam spot**: a small ratio of the beam divergence to the scan range is important. The large scan range is necessary to access every point of the mirror. At the same time the beam spot should be small compared to the mirror diameter in order to address even small lobes of a mechanical mode shape with a high overlap.

4 Fast beam deflection

4.1 Introduction

In the previous chapter we stated that the auxiliary damping laser beam needs to be deflected rapidly in order to efficiently damp mechanical modes in the kHz-range. This demands a fast laser deflection in 2D. In many other applications, like optical coherence tomography [87], holographic memory systems [88], optical switches and interconnects [89], as well as 3D laser imaging microscopy [90], a fast laser deflection is essential. There are beam deflectors that are mechanically driven including for example rotating polygon mirrors [91, 92], galvano-scanners [91, 92] and piezo-scanners [91, 92]. Another group of deflectors uses an optically transparent medium to change the incident beam direction by changing the optical properties of this medium. Examples are spatial light modulators [93], electro-optic modulators [94] and acousto-optic modulators (AOMs) [95]. A third group of deflectors recombine several beams with a different relative phase in order to change the output beam direction as for example in optical phased arrays (OPAs) [96]. An overview of the different laser scan methods and their classification can be found in [97, 91, 92, 94]. Mechanically driven deflectors provide a large scan range in 2D but they are limited in speed because of inertia associated with the mass of moving parts. One dimensional rapid beam deflection can be obtained for example with OPAs and has been demonstrated for 40 MHz steering speed, but for a small scan range of 4.2 mrad [98]. An OPA system with a larger scan range of 19 degrees (331 mrad) has been developed, but with a lower speed of 2 MHz [99]. Electro-optic modulators based on KTN crystals have a steering speed of up to 400 kHz with a deflection range of up to 200 mrad [100, 100, 101]. A one dimensional electro-optic system has also been demonstrated with scanning speeds of up to 500 MHz at the expense of a reduced scan angle of 1-2 mrad [102]. And even a 2D electro-optic deflector has been developed with a 13 MHz scan speed and a scan range of 2-3 mrad [103] that has been improved up to 7 mrad [104].

Even though these systems offer a fast deflection, they have been tested for relatively low optical power ($\sim$ mW) and in sinusoidal scan mode. Another way to deflect high power beams in arbitrary directions is the use of AOMs. In this chapter rapid beam deflection based on AOMs is presented. Two different experiments are demonstrated using two different AOM drivers. Its content is based on the paper "High speed, high

power 2D beam steering for mitigation of optomechanical parametric instability in gravitational wave detectors" [105] by Thomas Harder, Margherita Turconi, Rémi Soulard and Walid Chaibi, submitted to Optics Express.
In Section 4.2 the physical principles of an AOM are discussed. Section 4.3 demonstrates a first approach of fast modulated AOM driver signal generation based on optical heterodyne detection. It discusses the implementation and results of an Mach-Zehnder interferometer with an AOM and an electro-optic phase modulator in each arm for this purpose. The use of this driver signal for one dimensional beam deflection with an AOM is discussed in section 4.4. In a subsequent conclusion the results are compared with a model and the limits of using a system based on this technique for our active PI mitigation are discussed. Section 4.5 presents a second approach to generating fast changing AOM driver signals based on a software-defined radio. Its application in a 2D deflection system based on two AOMs is discussed in section 4.6. In this section the implementation and results of these two AOMs with large deflection range and high rapidity are discussed.

4.2 Acousto-optic modulators

Acousto-optic modulators are based on the phenomenon of acousto-optical (AO) diffraction. Brillouin described theoretically the diffraction of light by acoustic waves in 1922 [106]. Independently R. Lucas and P. Biquard [107] as well as P. Debye and F.W. Sears [108] observed experimentally the same phenomenon. Ten years later, C.V. Raman and N.S. Nagendra Nath extended the theoretical description of acousto-optic interaction in isotropic media [109, 110] as they differentiated two regimes of AO interaction: The Bragg-regime for typically high acoustic frequencies and big AO interaction lengths describing the diffraction in two orders, the zero and first order. The Raman-Nath regime for typically small acoustic frequencies and small AO interaction lengths describes the diffraction into many diffraction orders symmetrically distributed around the zero order. Since the diffraction efficiencies (intensity of the diffracted beam divided by intensity of the incoming beam) in the Raman-Nath regime are quite low, AOM devices are mainly built in the Bragg regime.
The fundamental mechanism for acousto-optic interaction is the elasto-optic effect [92, 91]: In the presence of an acoustic wave in a medium, its refractive index changes locally. This is the case, because the pressure distribution of an acoustic wave creates regions with higher and lower density inside the medium. And the density of a medium is directly related to the refractive index.
The diffraction of light on acoustic waves can be explained in several ways. The propagating acoustic wave can be conceived as a grating of spatial modulated refractive index. The incident light beam will be diffracted at this propagating grating. Alternatively, light and sound can be described as particles: photons and

phonons, respectively. Thus, diffraction is the scattering of photons and phonons under conservation of energy and momentum.
In the following some important relations for laser beam diffraction with an AOM will be derived (isotropic beam diffraction is supposed) by describing light and sound as particles.

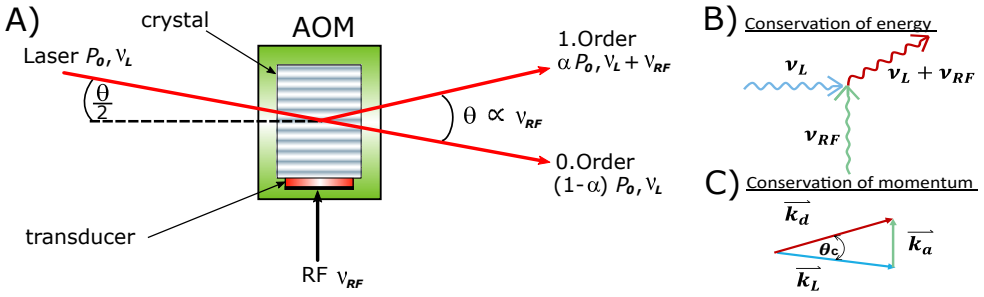

Fig. 4.1: Schematic of an AOM with isotropic diffraction. A) The components of an AOM. A radio frequency ν_{RF} is applied to a transducer which vibrates with this frequency and creates a grating of moving acoustic waves in the crystal. A part α of the incoming laser beam power P_0 with frequency ν_L is diffracted at the grating into the 1st diffraction order. The laser frequency is increased by the radio frequency. The diffraction angle θ is proportional to the radio frequency. (Beam refraction between the medium outside the crystal and inside is not shown for simplification purpose.) B) The frequency shift of the deflected beam is due to phonon absorption by conservation of energy. C) The diffraction angle is a result of the conservation of momentum.

Figure 4.1 shows a simplified schematic of an AOM. It consists basically of a crystal, a transducer and a casing. The transducer is bound to the crystal. A radio frequency (RF) ν_{RF} is applied to the transducer, which will start to vibrate and create a propagating acoustic wave in the crystal. A portion α of the incoming laser beam with frequency ν_L and power P_0 will be diffracted into the 1st order. α describes the diffraction efficiency DE of the AOM

$$DE = \frac{P_1}{P_0} = \alpha \tag{4.1}$$

with P_1, the optical power in the diffracted beam. The frequency of the diffracted beam will be shifted by the radio frequency according to the conservation of energy (see fig. 4.1B). The diffraction angle θ_c (inside the crystal) is proportional to the applied radio frequency ν_{RF} and is the result of the conservation of momentum.

$$\vec{k_d} = \vec{k_L} + \vec{k_a} \tag{4.2}$$

The magnitude of the diffracted wave vector $\vec{k_d}$, the incident laser wave vector $\vec{k_L}$ and the acoustic wave vector $\vec{k_a}$ is given by

$$k_L = \frac{2\pi n_L}{\lambda_L} \quad k_d = \frac{2\pi n_d}{\lambda_d} \quad k_a = \frac{2\pi}{\Lambda} \tag{4.3}$$

for the incident laser wavelength $\lambda_L = \frac{c}{\nu_L}$, the diffracted laser wavelength $\lambda_d = \frac{c}{\nu_L + \nu_{RF}}$ and the acoustic wavelength $\Lambda = \frac{V_a}{\nu_{RF}}$. n_L and n_d are the refractive indices of the crystal for λ_L and λ_d, c is the speed of light, V_a the acoustic velocity in the crystal and ν_{RF} the frequency of the acoustic wave, which is equal to the radio frequency. Since $\nu_L \gg \nu_{RF}$ the frequency of the diffracted beam can be approximated with ν_L, which gives $k_d = k_L$. The diffraction angle θ_c can be determined in the isosceles triangle in fig. 4.1C) as

$$\sin\left(\frac{\theta_c}{2}\right) = \frac{k_a}{2k_d} = \frac{\lambda_L}{2n_L\Lambda} = \frac{\lambda_L \nu_{RF}}{2n_L V_a} \tag{4.4}$$

The angle θ shown in figure 4.1A) between the zeroth and first order beam outside the crystal is obtained by using the Snell's law with the index of refraction of air $n_a = 1$:

$$n_a \sin\left(\frac{\theta}{2}\right) = n_L \sin\left(\frac{\theta_c}{2}\right) \tag{4.5}$$

For a small-angle approximation of $\sin a \approx a$, which is a good approximation for most AOM, we get a diffraction angle θ:

$$\theta = \frac{\lambda_L \nu_{RF}}{V_a} \tag{4.6}$$

The rapidity of an AOM is characterized by its rise time t_R. It equals the time it takes the acoustic wave to pass through the beam. For a Gaussian beam with a $\frac{1}{e^2}$ waist radius w_b it is:

$$t_R = \frac{2w_b}{V_a} \tag{4.7}$$

The conventional rise time t_r is defined as the time it takes the intensity to rise from 10% to 90% which is [91]:

$$t_r = 0.64\frac{2w_b}{V_a} \tag{4.8}$$

In order to increase the rapidity of an AOM, the beam has to be focused into the AOM, furthermore, crystals with a high acoustic velocity V_a should be used.

When an AOM is used as a deflector, the driver frequency is varied to change the diffraction angle. The scan angle $\Delta\theta$ can be derived from equation 4.6 as function of the frequency variation of the AOM driver frequency $\Delta\nu_{RF}$:

$$\Delta\theta = \frac{\lambda_L}{V_a}\Delta\nu_{RF} \tag{4.9}$$

For this case, $\vec{k_L}$ in the vector diagram shown in figure 4.1C) is unchanged since the incident beam is fixed. The length of $\vec{k_d}$ does not change (since $\nu_L \gg \nu_{RF}$), but θ changes. In order to conserve momentum, the angle of $\vec{k_a}$ should also change. This means that the acoustic wave vector $\vec{k_a}$ should also have an angular spread of $\delta\phi$ so

that the momentum conservation can be fulfilled for different RF frequencies. The

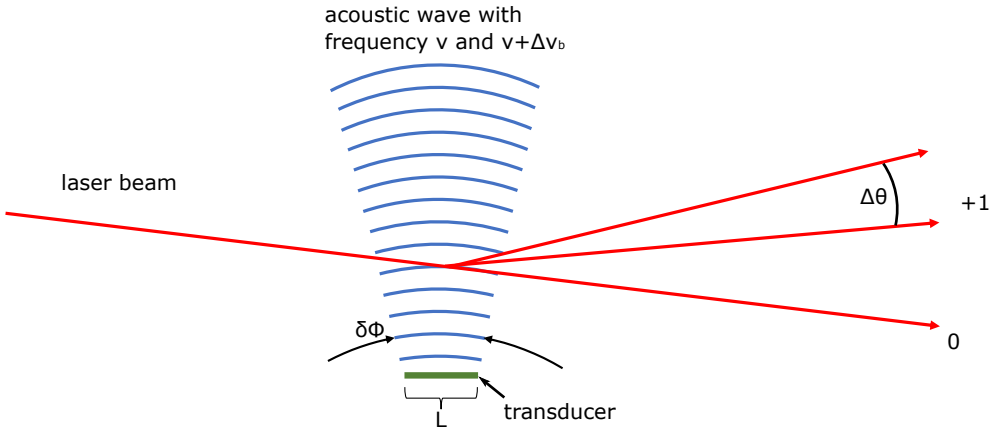

Fig. 4.2: Schematic figure of beam deflection in an AOM used as beam deflector. Changing the acoustic wave frequency from ν to $\nu + \nu_b$ changes the diffraction angle by $\Delta\theta$. In order to conserve momentum, the acoustic wave has an angular spread of $\delta\phi$ introduced by the diffraction of the wave by the finite aperture of the transducer of length L

angular spread $\delta\phi$ can be obtained by reducing the transducer length L. It is given by

$$\delta\phi \approx \frac{\Lambda}{L} \tag{4.10}$$

considering the diffraction of a wave on a rectangular aperture. Thus, a large scan angle is obtained by decreasing the transducer length L in the interaction plane. But a small interaction length between the acoustic and the light wave will decrease the diffraction efficiency.

To overcome this limitation an array of transducers can be used [111, 95], as depicted in figure 4.3 . All transducers have the same distance from each other. The driver signal $\mathrm{RF}_{\mathrm{in}}$ of each transducer has a fixed phased shift of β. The phase shift can be introduced for example by a RF delay line providing a constant time delay [112]. A resultant acoustic wave front is built, which has an inclination of α with respect to the single wave fronts of the transducer. When the acoustic frequency ν_{RF} increases, α decreases also. In this way the incident beam angle θ increases, providing the conservation of momentum. In this manner a higher diffraction efficiency in a larger acoustic bandwidth can be provided.

The phenomenon of acousto-optic diffraction gives rise to several applications. By modulating for example the amplitude of the driver radio frequency, the diffraction efficiency will be modulated. In this way, an AOM can be used as amplitude modulator. As the frequency of the diffracted beam is shifted by the driver radio frequency, an AOM can be used as frequency shifter. Furthermore, an AOM can be used as a deflector by modulating the driver frequency. There are various other applications like tunable filters [113], spectrum analysers [114] and signal processors [115] that can be performed with AOM. An overview of different AOM devices can

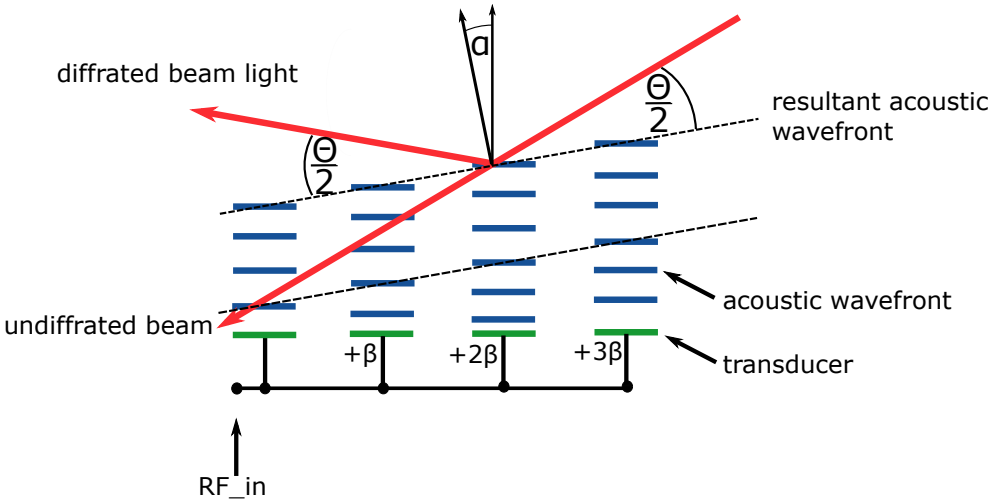

Fig. 4.3: Schematic of acousto-optic diffraction with a phased array of transducers. Each transducer is driven with the driver signal $\mathrm{RF_{in}}$, but with a constant phase shift of β to the adjacent transducers. By this means a resultant acoustic wavefront in the AO crystal is built, that inclines with a changing driver frequency in order to conserve momentum for beam diffraction.

be found in [116, 91]. The choice of the crystal, its size, orientation and form, depends on the application. Commercial AOMs that are designed for deflection have scan ranges up to 50 mrad with a steering speed of hundreds of kHz up to some MHz, depending on the beam diameter. AOMs designed for amplitude modulation attain higher repetition rates up to hundreds of MHz at the expense of the scan range [117]. The fact that AO deflectors have usually bigger rise times than AO modulators comes from the choice of the crystals and the direction of the propagating acoustic wave, especially in birefringent crystals. To obtain larger scan ranges slow acoustic velocities are chosen (see eq. 4.9), but this implies bigger rise times (from eq. 4.8). In order to obtain a large scan range with high rapidity, a compromise between a deflector and a modulator should be chosen.

In order to be capable of deflecting with an AOM with high rapidity it is crucial to have a fast modulated driver signal.

4.2.1 AOM driver

Commercial AOM drivers are either voltage controlled oscillators with rather slow commutation times in the µs range [117], or direct digital synthesizers (DDS) with commutation times of hundreds of ns [117, 118, 119]. Additional delay is added by programming data to the DDS chip and is limiting the maximal output rate. A frequency generator, based on a field-programmable gate array (FPGA) and a DDS, has been presented with consecutive frequency changing of less than 1 µs [120] even if the frequency change at the DDS is done below 100 µs [121]. These solutions

are not fast enough to obtain deflection rates up to 10 MHz. The investigated AOMs have a nominal rise time of 33 ns for a 210 μm beam spot, which should be the only limiting factor of the designed system.

Two different solutions are proposed and tested to generate fast modulated radio frequencies in order to obtain rapid beam deflection with AOMs.

4.3 Generation of fast modulated RF signals through optical heterodyne detection

Since the DDS available in the laboratory were limited to change the generated radio frequency with a rate of several kHz, they did not satisfy our requirements. But a phase modulator with a nominal electro-optic bandwidth of several GHz was available. For this reason, in a first approach we generated fast modulated radio frequencies by heterodyne detection as we took advantage of the rapidity of the phase modulator.

4.3.1 Theory

Heterodyne detection, which was originally developed for radio communication, can also be used with optical waves [122, 123]. It consists in the interference of two distinct frequencies. The beat note will have a fast oscillating component with a sum of both frequencies and a slow oscillating part with the difference of both frequencies. This technique can be used to create optically a fast modulated signal, by modulating one of the two interfering frequencies. The optical beat note is created in a Mach-Zehnder Interferometer and converted with a photodiode into an electric signal.
Figure 4.4 depicts a setup. Using a beam splitter (BS), the laser beam is split into two arms. In one arm the beam crosses an electro-optic phase modulator (EOM). It is being used to modulate the phase of the incoming laser and is driven by a radio frequency $\mathrm{RF}_{\mathrm{mod}}$. In the other Mach-Zehnder arm the beam crosses an AOM driven by a fixed radio frequency $\mathrm{RF}_{\mathrm{car}}$. The zero diffraction order is damped and the first order, which has a shifted frequency, is recombined with the beam of the phase modulator arm in a second beam splitter. Now recombined, the optical signal is transformed into an electrical signal by a photodiode. The electrical signal obtained at the output of the photodiode can be derived in the following way: Taking only the

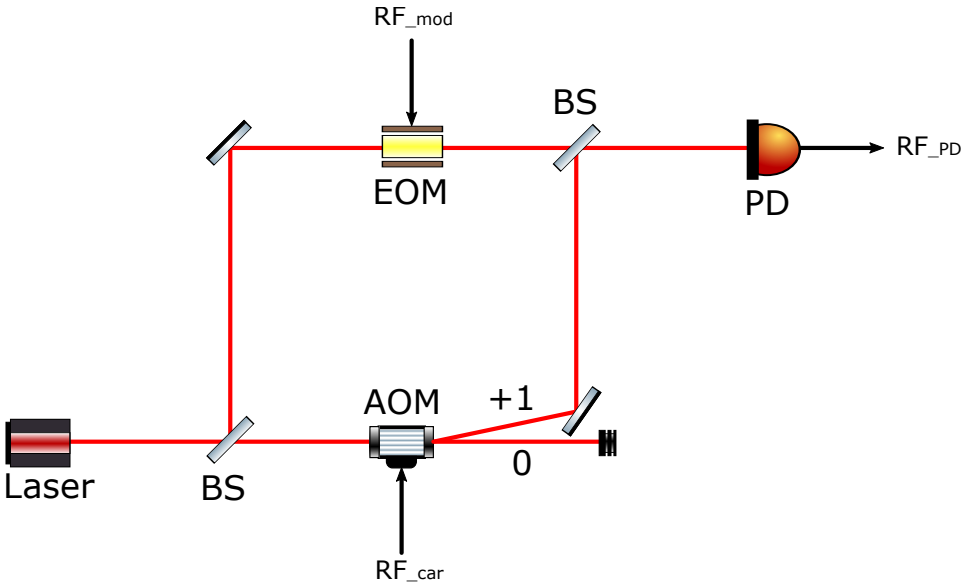

Fig. 4.4: A Mach-Zehnder Interferometer to create fast modulated radio frequencies. The laser beam is split by a beam splitter (BS) into two arms. One arm contains an electro-optic phase modulator (EOM) while the other arm contains an AOM. While the phase modulator is driven by a radio frequency ($\mathrm{RF_{mod}}$) the AOM is driven by a radio frequency ($\mathrm{RF_{car}}$).The first order deflected beam is shifted by $\mathrm{RF_{car}}$. The photodiode (PD) captures the optical signal and transforms it in an electric signal $\mathrm{RF_{PD}}$ which has a carrier frequency of $\mathrm{RF_{car}}$ modulated at the frequency of $\mathrm{RF_{mod}}$.

electric field into consideration, the temporal evolving electromagnetic wave hitting the photodiode coming from the phase modulator arm y_{PM} can be described as

$$y_{PM}(t) = A_1 \cos(2\pi\nu_L t + \phi_0 \sin(2\pi\nu_{mod} t) + \phi_{PM}) \tag{4.11}$$

with the amplitude A_1, the laser frequency ν_L, a phase shift ϕ_0 introduced by the phase modulator with a modulation frequency ν_{mod}, which is equal to the applied radio frequency $\mathrm{RF_{mod}}$ and a constant phase ϕ_{PM}. The electromagnetic wave coming from the AOM y_{AOM} can be described as

$$y_{AOM}(t) = A_2 \cos(2\pi(\nu_L + \nu_{car})t + \phi_{AOM}) \tag{4.12}$$

with the amplitude A_2 and the carrier frequency ν_{car} which is equal to the driver frequency $\mathrm{RF_{car}}$ and a constant phase ϕ_{AOM}. The superposition of both waves $y = y_{AOM} + y_{PM}$ gives

$$y(t) = 2A_1A_2 \cos\left(\frac{2\pi(2\nu_L + \nu_{car})t + \phi_0 \sin(2\pi\nu_{mod}t) + \phi_{AOM} + \phi_{PM}}{2}\right) \cos\left(\frac{2\pi\nu_{car}t - \phi_0 \sin(2\pi\nu_{mod}t) + \phi_{AOM} - \phi_{PM}}{2}\right) \tag{4.13}$$

It can be seen in eq. 4.13 that you have one cosine term describing a fast oscillation with the double of the laser frequency and one cosine term describing an oscillation with the carrier frequency ν_{car}. Both terms have a modulated phase with a frequency of ν_{mod}. The photodiode captures the intensity I of the electromagnetic wave y

$$I(t) = c\epsilon_0 y^2(t) \tag{4.14}$$

with the speed of light c and the permittivity of free space ϵ_0. The photodiode will only resolve the low frequency oscillation of the second term and captures the average of the fast oscillating term, which gives a factor of $1/2$, so that

$$I(t) = 2A_1^2 A_2^2 c\epsilon_0 \cos^2\left(\frac{2\pi\nu_{car}t - \phi_0\sin(2\pi\nu_{mod}t) + \phi_{AOM} - \phi_{PM}}{2}\right) \tag{4.15}$$

with $\cos^2 x = \frac{1+\cos 2x}{2}$ we can write

$$I(t) = A_1^2 A_2^2 c\epsilon_0 + A_1^2 A_2^2 c\epsilon_0 \cos(2\pi\nu_{car}t - \phi_0\sin(2\pi\nu_{mod}t) + \phi_{AOM} - \phi_{PM}) \tag{4.16}$$

The electric signal $\mathrm{RF_{PD}}$ at the output of the photodiode is proportional to I. As we are interested in the time-varying part of I, $\mathrm{RF_{PD}}$ can be written as

$$\mathrm{RF_{PD}}(t) = A_{PD}\cos(\omega_{car}t + \phi_0\sin(\omega_{mod}t)) \tag{4.17}$$

with an amplitude $A_{PD} \propto A_1^2 A_2^2 c\epsilon_0$, which is modulated with the angular frequency $\omega_{car} = 2\pi\nu_{car}$ and a time dependent phase term with ϕ_0, which is modulated with an angular modulation frequency of $\omega_{mod} = 2\pi\nu_{mod}$. Since we use the AC output of the photodiode, the constant $A_1^2 A_2^2 c\epsilon_0$ from eq. 4.16 which adds an offset to the signal is neglected. The amplitude A_{PD} depends on the deflection efficiency of the AOM and the insertion losses of the phase modulator. It has minor importance since the electric signal of the photodiode can be amplified before driving an AOM. ν_{car}, the frequency of RF_{car}, is chosen in a way to fit the carrier frequency of the AOM, which is driven with this fast modulated frequency. The phase term is modulated in time and adds a frequency component to ω_{car}, as the time derivative of the phase is a frequency. The instantaneous frequency ν_i of $\mathrm{RF_{PD}}$ equals

$$\nu_i(t) = \nu_{car} + \frac{1}{2\pi}\frac{d}{dt}\phi_0\sin(\omega_{mod}t) \tag{4.18}$$

which gives

$$\nu_i(t) = \nu_{car} + \phi_0\nu_{mod}\cos(\omega_{mod}t) = \nu_{car} + \Delta\nu_{car}\cos(\omega_{mod}t) \tag{4.19}$$

Eq. 4.19 shows that the product of $\phi_0\omega_{mod}$ gives the maximal frequency deviation $\Delta\nu_{car}$ of the modulated signal $\mathrm{RF_{PD}}$. ϕ_0 is technically limited by the maximal RF input power level of the EOM.

Eq. 4.17 can also be represented exponentially, where $\mathrm{RF_{PD}}$ is the real part of this representation

$$\mathrm{RF_{PD}}(t) = \Re[A_{PD} e^{i(\omega_{car} t + \phi_0 \sin(\omega_{mod} t))}] \tag{4.20}$$

This is a periodic function with a periodicity of $\frac{2\pi}{\omega_{mod}}$, which can be expanded by a Fourier series:

$$A_{PD} e^{i\omega_{car} t} e^{i\phi_0 \sin(\omega_{mod} t)} = A_{PD} e^{i\omega_{car} t} \sum_{n=-\infty}^{\infty} C_n e^{in\omega_{mod} t} \tag{4.21}$$

with

$$C_n = \frac{\omega_{mod}}{2\pi} \int_{-\pi/\omega_{mod}}^{\pi/\omega_{mod}} e^{i\phi_0 \sin(\omega_{mod} t)} e^{-in\omega_{mod} t} dt \tag{4.22}$$

by substituting $\omega_{mod} t = x$ we get

$$C_n = \frac{1}{2\pi} \int_{-\pi}^{\pi} e^{i(\phi_0 \sin x - nx)} dx = J_n(\phi_0) \tag{4.23}$$

where C_n is the integral representation of the Bessel functions $J_n(\phi_0)$ of the first kind with the order n. Figure 4.5 shows a modulated signal described by the equation 4.17 with ν_{car} = 110 MHz, ν_{mod} = 10 MHz and $\phi_0 = \pi$. In the time domain one can see that the sinusoidal modulation of the phase ϕ_0 results in a modulation of the frequency ν_{car}. In the frequency domain (fig. 4.5B) this phase modulation adds side bands with peaks that have a relative distance of ν_{mod}. The amplitude of each side band peak $A_{\nu_{car}+n\nu_{mod}}$ can be determined by the Bessel functions as derived in eq. 4.23

$$|A_{\nu_{car}+n\nu_{mod}}| = A_{PD} \, |J_n(\phi_0)| \tag{4.24}$$

As the intensity is proportional to A^2, we measure

$$|A_{\nu_{car}+n\nu_{mod}}|^2 = A_{PD}^2 \, |J_n(\phi_0)|^2 \tag{4.25}$$

with a spectrum analyzer.

As explained above, a fast modulated driver frequency for an AOM can be built.

4.3.2 Experimental setup

A Mach-Zehnder Interferometer is set up as depicted in fig. 4.6. We used a fiber seed laser (NKT Photonics Koheras Adjustik) with a wavelength of λ = 1064 nm and a fiber amplifier (Manlight) to have a power level of around 100 mW. The beam is split with a fiber 50/50 splitter. One arm is connected to an electro-optic fiber phase modulator (Photoline NIR-MPX-LN-05-P-P-FA-FA). Using a set of two lenses L1 and L2, the other arm is collimated into the AOM (AA opto-electronic) in free space. Its first order diffracted beam size is adjusted with lens L4 to fit the beam size

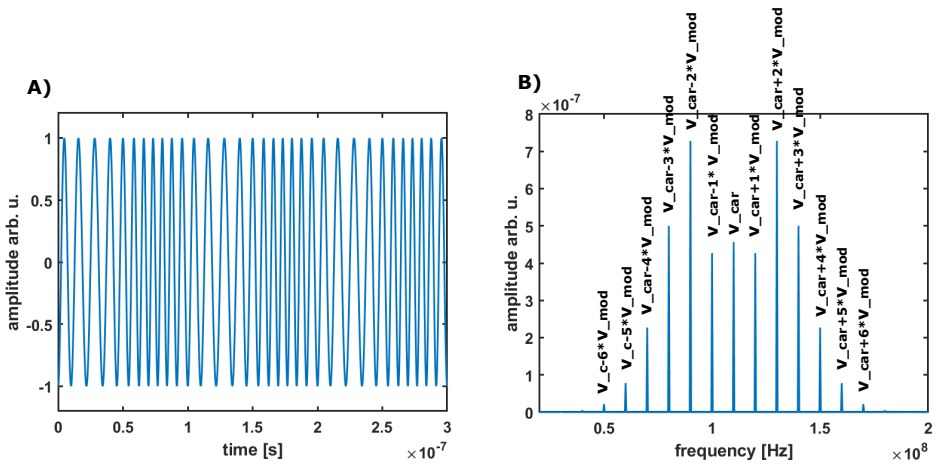

Fig. 4.5: A modeled modulated frequency signal described by eq. 4.17 with $\nu_{car} = 110$ MHz, $\nu_{mod} = 10$ MHz and $\phi_0 = \pi$ in time domain (A) and in frequency domain (B).

of the phase modulator arm. Both arms are recombined with a 50/50 beam splitter and focused with lens L5 into the photodiode (PD). The phase modulator (EOM) is driven with a radio frequency $\mathrm{RF_{mod}}$ in the range between 1 and 20 MHz. The RF signal is amplified to maximal 28 dBm, the maximal RF input power of the EOM given by the manufacturer. The AOM is driven with a fixed radio frequency $\mathrm{RF_{car}}$ of 110 MHz.

4.3.3 Results

In the first place we investigated the different optical components of our experimental setup: For our Mach-Zehnder interferometer we used an available AOM in our laboratory of the brand AA acousto-electronics that was not further specified. It had a measured transmission coefficient of around 67% for the laser wavelength of 1064 nm without any applied driver signal. A possible reason for this low transmission coefficient could be the fact that this AOM had been designed for a different wavelength. But since we only wanted to add a fixed frequency shift of 110 MHz to the optical signal and we amplified the electrical signal of the photodiode after the interferometer anyway, the low transmission coefficient of the AOM was of minor importance. For a RF input power level of 33 dBm at 110 MHz we measured a polarisation independent deflection efficiency of $DE = 44\%$. In the next step we measured the optical output of the fiber phase modulator. Figure 4.7 shows the photodiode output voltage measuring the optical output of the phase modulator for a driver signal $\mathrm{RF_{mod}}$ with a power level of 28 dBm at a frequency of $\nu_{mod} = 5$ MHz. In subplot A) one can see that the phase modulator also creates an amplitude modulation of the optical signal. The RMS amplitude of the modulation is 6% of the mean DC value. Subplot B) shows the Fourier transform of the measured amplitude

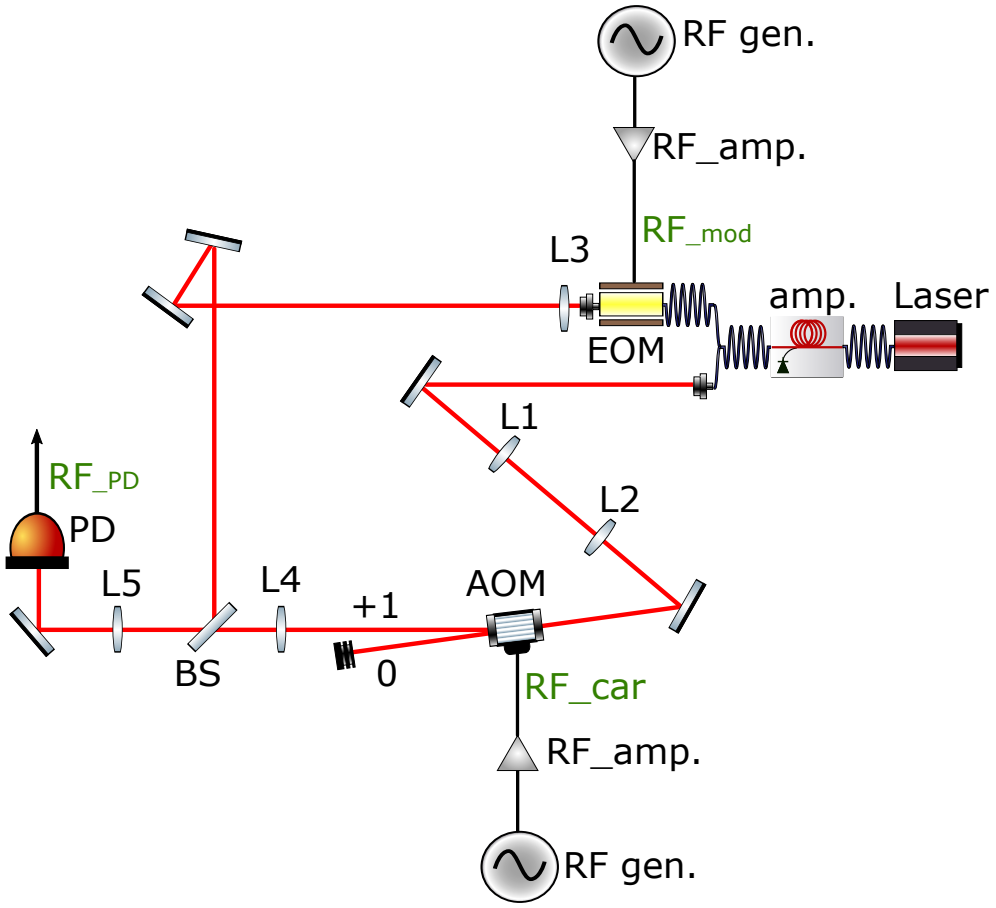

Fig. 4.6: Experimental setup of an Mach-Zehnder Interferometer to create optically a fast modulating signal, which is transformed with a photodiode into an electrical signal ($\mathrm{RF_{PD}}$). The fiber seed laser is amplified with a fiber amplifier (amp.) and split into two arms. One arm is connected with an electro-optic fiber phase modulator (EOM) which is driven by a driver frequency of ($\mathrm{RF_{mod}}$). The other arm is guided in free space and collimated with a set of lenses L1 +L2 into the AOM. The AOM is driven with a radio frequency $\mathrm{RF_{car}}$ of 110 MHz. The first order diffracted beam is adjusted with lens L4 and recombines with the EOM arm beam in a 50/50 beam splitter (BS). The superposition of both beams is focused with lens L5 into the photodiode (PD). Both radio frequency signals are generated by two RF generators and amplified with RF amplifiers (RF amp.) to the desired power level.

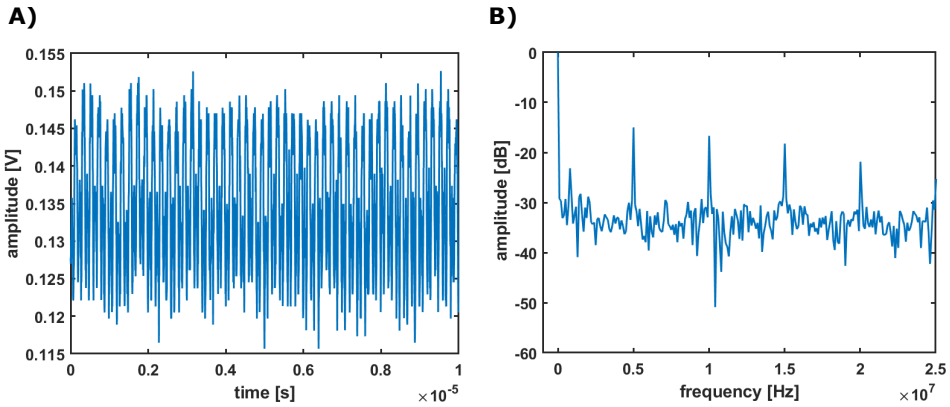

Fig. 4.7: Residual amplitude modulation of phase modulator with $\nu_{mod} = 5$ MHz at a RF input power of 28 dBm. A) Optical signal at the PM output captured with a photodiode and with an oscilloscope B) the calculated frequency spectrum

modulation. The spectrum shows an amplitude modulation at the modulation frequency $\nu_{mod} = 5$ MHz with its higher harmonic oscillations of 10 MHz, 15 MHz, 20 MHz, etc. with decreasing amplitudes. An additional amplitude oscillation between 700 and 800 kHz is present (not shown here). By measuring the spectrum of the laser we observed also amplitude oscillations at these frequencies. This allowed us to conclude that these power oscillations were coming from our laser. It could be due to relaxation oscillations in the active fiber of the laser.

In the next step we analysed the electrical signal $\mathrm{RF_{PD}}$ after the Interferometer. There was only an oscilloscope available in the laboratory at that time with a bandwidth of 70 MHz. For this reason we chose a carrier frequency of $\nu_{car} = 60$ MHz. The power level of $\mathrm{RF_{mod}}$ is set to the maximum power input of the EOM of 28 dBm. Figure 4.8 shows the AC part of $\mathrm{RF_{PD}}$, measured with an oscilloscope and a spectrum analyzer for different modulation frequencies ν_{mod}. In the left column a modulated signal with a carrier frequency of 60 MHz can be seen. The measured frequency modulation corresponds to the expected signal in figure 4.5A. However, figure 4.8 shows a superposed amplitude modulation with a frequency of ν_{mod}. As already mentioned and depicted in figure 4.7, this amplitude modulation is introduced by the phase modulator. In the right column of the figure the measured frequency spectrum of $\mathrm{RF_{PD}}$ is shown. It is not symmetric around $\nu_{car} = 60$ MHz.

The peaks at frequencies higher than 60 MHz ($\nu_{car} + n\nu_{mod}$ with n = 1,2,3...) are smaller compared to their corresponding peaks at frequencies smaller than 60 MHz ($\nu_{car} - n\nu_{mod}$). This amplitude modulation is amplified in the data acquired with the oscilloscope, since it has a bandwidth of 70 MHz. The spectrum analyzer has a bandwidth of 1.3 GHz and displays a more reliable spectrum of the measured modulation.

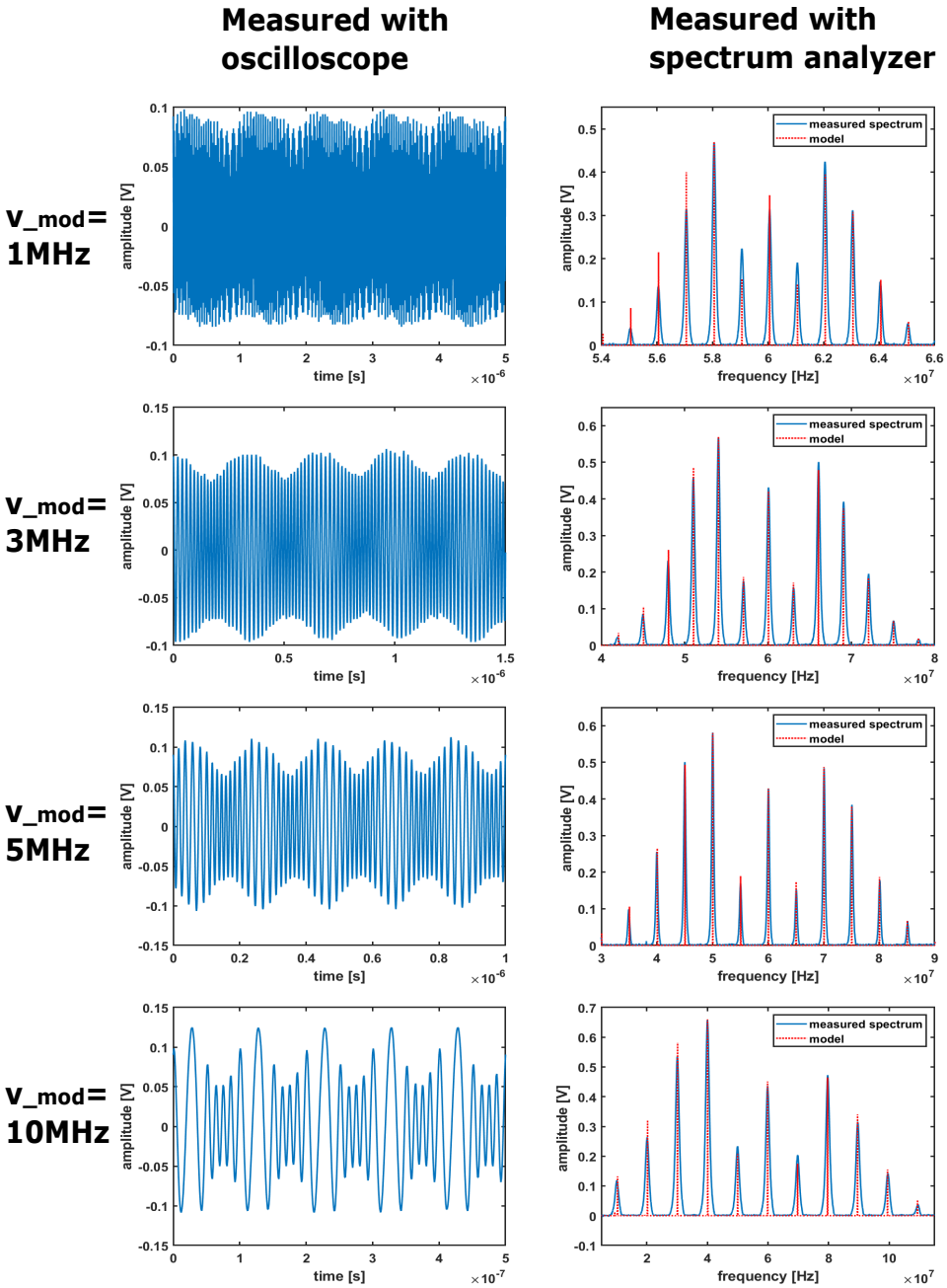

Fig. 4.8: Optical beat note captured with a photodiode at the output of the Mach-Zehnder inteferometer as depicted in fig. 4.6 with ν_{car}=60 MHz and ν_{mod} = 1,3,5 and 10 MHz at a EOM input power of 28 dBm. $\mathrm{RF_{PD}}$, the output of the photodiode is displayed with an oscilloscope (left column) and with a spectrum analyzer (right column) that is compared with a modeled spectrum based on equation 4.26, with $\phi_0 = 3.45$ including an amplitude modulation with the phase $\phi_a = \frac{\pi}{2}$ and $m = 0.15$ for ν_{mod} = 1,3,5 MHz and $m = 0.3$ for ν_{mod} = 10 MHz.

In order to take the residual amplitude modulation (RAM) into account in the description of $\mathrm{RF_{PD}}$, equation 4.17) can be expanded:

$$\mathrm{RF_{PD}}(t) = A_{PD}\cos(\omega_{car}t + \phi_0\sin(\omega t))(1 + m\cos(\omega_{mod}t - \phi_a)) \tag{4.26}$$

with m, the coefficient of the amplitude modulation and ϕ_a the associated phase shift.
The frequency spectra depicted in figure 4.8 are modeled with the Fourier transform of equation 4.26 by choosing the coefficients empirically. The measurement shows a good agreement for the modeled spectrum of $\mathrm{RF_{PD}}$ with $\phi_0 = 3.45$ taking into account the amplitude modulation with a phase shift of $\phi_a = \frac{\pi}{2}$ and the modulation coefficient $m = 15\%$ for ν_{mod}= 1, 3 and 5 MHz and m =30% for $\nu_{mod} = 10$ MHz.
It can be seen that the RAM is the reason why the spectrum around $\nu_{car} = 60$ MHz shown in the measured spectrum is asymmetric. The measured RAM of 15% for ν_{mod} up to 5 MHz and even 30% for $\nu_{mod} = 10$ MHz seem to increase with higher modulation frequencies.

The RF input power of the phase modulator which defines ϕ_0 is constant. Therefore the maximal frequency variation $\Delta\nu_{car}$ depends on the modulation frequency ν_{mod} (see equation 4.19). $\Delta\nu_{car}$ for $\nu_{mod} = 1$ equals 3.45 MHz, which increases up to 34.5 MHz for $\nu_{mod} = 10$ MHz. As expected for a modulation with $\phi_0 = \pi$ (figure 4.5B), the frequency peaks of $\nu_{car} \pm 2\nu_{mod}$ have the highest amplitude, followed by $\nu_{car} \pm 2\nu_{mod}$.

For further investigations the RF input power of the phase modulator is varied. The driver frequency ν_{car} of the AOM is set to 110 MHz and ν_{mod} the driver frequency of the EOM is set to 5 MHz. Likewise, the spectrum of the photodiode output voltage is measured with a spectrum analyzer. Figure 4.9 shows the power of the frequency peak of ν_{car}, $\nu_{car}+\nu_{mod}$ and $\nu_{car}+2\nu_{mod}$ (see figure 4.5B) in the measured spectrum for different RF input powers of the phase modulator. The phase shift ϕ_0 corresponding to each power level of $\mathrm{RF_{mod}}$ is obtained in the following way: The $\mathrm{RF_{mod}}$ input voltage (RMS) is first calculated by taking the 50 Ohm impedance of the RF input into consideration. V_π, the voltage which needs to be applied at the RF input port in order to shift the optical signal in the PM by π is given by the manufacturer with 5 V (RMS). Taking this parameter into account, ϕ_0 is calculated for each $\mathrm{RF_{mod}}$ input power.
The obtained results are in accordance with the derived expression in equation 4.25, which states that the power of the frequency peaks in the frequency domain follows the square of the Bessel functions of the first kind.

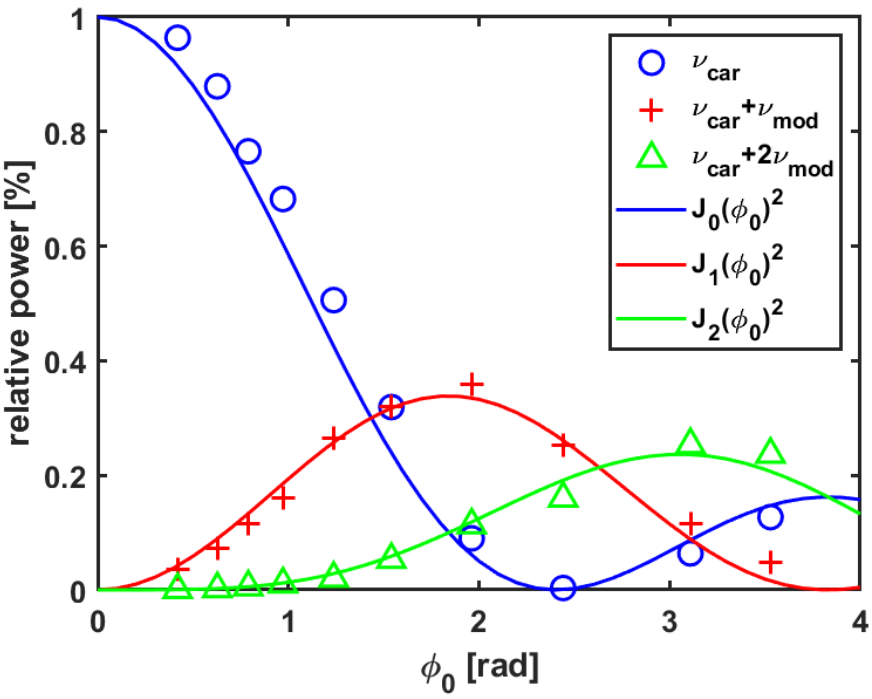

Fig. 4.9: Relative power of the carrier and frequency side bands (divided by total power) $\nu_{car} + n\nu_{mod}$ for n = 0, 1, 2 of the measured spectrum of the amplified photodiode signal after the interferometer with ν_{mod} = 5 MHz with a $\mathrm{RF_{mod}}$ input power in the range from 9.5 to 28 dBm and ν_{car} = 110MHz for V_π(RMS) = 5 V.

4.3.4 Conclusion

Optical heterodyne detection gives the opportunity to generate fast modulated radio frequencies of several MHz due to the high bandwidth of the used phase modulator. We are able to create a sinusoidal modulated radio frequency with a maximal frequency deviation ν_{car} of up to 34.5 MHz at a modulation frequency of 10 MHz. The radio frequency is created in a Mach-Zehnder Interferometer by converting an optical beat note. In one arm the beam is frequency shifted with an AOM and the beam in the other arm is phase modulated with an electro-optic phase modulator. An electric signal is obtained by converting the optical signal with a photodiode. The maximal frequency deviation depends on the modulation frequency and is limited by the maximal input power of the phase modulator which is 28 dBm for the used phase modulator corresponding to a maximal phase shift of 3.45 rad. It results in a maximal frequency deviation of 3.45 MHz for a modulated signal at 1 MHz and increases to 34.5 MHz for a modulation at 10 MHz. The carrier frequency ν_{car} of the created radio frequency is defined by the driver frequency of the AOM used in the Mach-Zehnder Interferometer. It can be chosen arbitrarily, given that the diffraction efficiency for this driver frequency is not zero. Since the phase modulator introduces an amplitude modulation, the obtained signal $\mathrm{RF_{PD}}$ will have an amplitude modulation that needs to be taken into consideration.

4.4 Fast 1D beam deflection with optically created driver signal

In this section we analyse 1D deflection of one AOM driven by the converted optical beat note, which is created in a Mach-Zehnder Interferometer (see figure 4.6). The driver frequency can be continuously changed for example in a sinusoidal way or by switching between discrete frequencies up to several MHz. Before we had the funds to buy an appropriate AOM with high rapidity and a large scan angle, an AOM that was already available in the laboratory was used to do fast beam deflection. Manufacturers often do not state the maximal modulation frequency at which the driver frequency of the AOM can be modulated. Instead, they just state an amplitude modulation bandwidth, or the rise time of the AOM. The rise time defines the time it takes an AOM to deflect a beam, when the driver signal power is switched from no power to full power. But we are interested in the commutation time or transition time, when the driver frequency is changed. This experiment enables us to get familiar with the limits of an AOM concerning its rapidity and to discover the limits of the optically generated fast modulated driver signal.

4.4.1 Experimental setup

The optical setup for fast beam deflection is basically the one shown in figure 4.6. One AOM is added to deflect the laser beam in one dimension with the optically created driver signal. Figure 4.10 shows a schematic of the setup. The laser beam guided in a fiber is split before entering the Mach-Zehnder Interferometer. One part is focused with a set of two lenses (L1 and L2) into an AOM (AA opto-electronics MT110-A1.5-1064) in free space. By changing the relative position of both lenses and their distance to the AOM, the beam waist in the AOM can be changed. The photodiode PD1 captures the optical beat note created in the Mach-Zehnder interferometer and converts it into the electric signal $\mathrm{RF_{PD}}$. The AOM is driven by the electric signal $\mathrm{RF_{PD}}$ which is intensified with an RF amplifier. The first order diffracted beam is split with a 50/50 beam splitter in order to capture the deflected beam scan with two photodiodes (PD2 and $\mathrm{PD_{trig}}$) at the same time. Photodiode PD2 is mounted on a horizontal translation stage to capture different positions of the horizontal fast deflected beam. As the beam is deflected at a fixed frequency of several MHz, the photodiode is placed on different positions along the deflection pattern and the temporal evolution of the beam passing through the photodiode is captured with a fixed trigger, which is given by photodiode $\mathrm{PD_{trig}}$. When these single temporal photodiode signals are put together with the information of the relative photodiode position, a spatial scan pattern can be constructed.

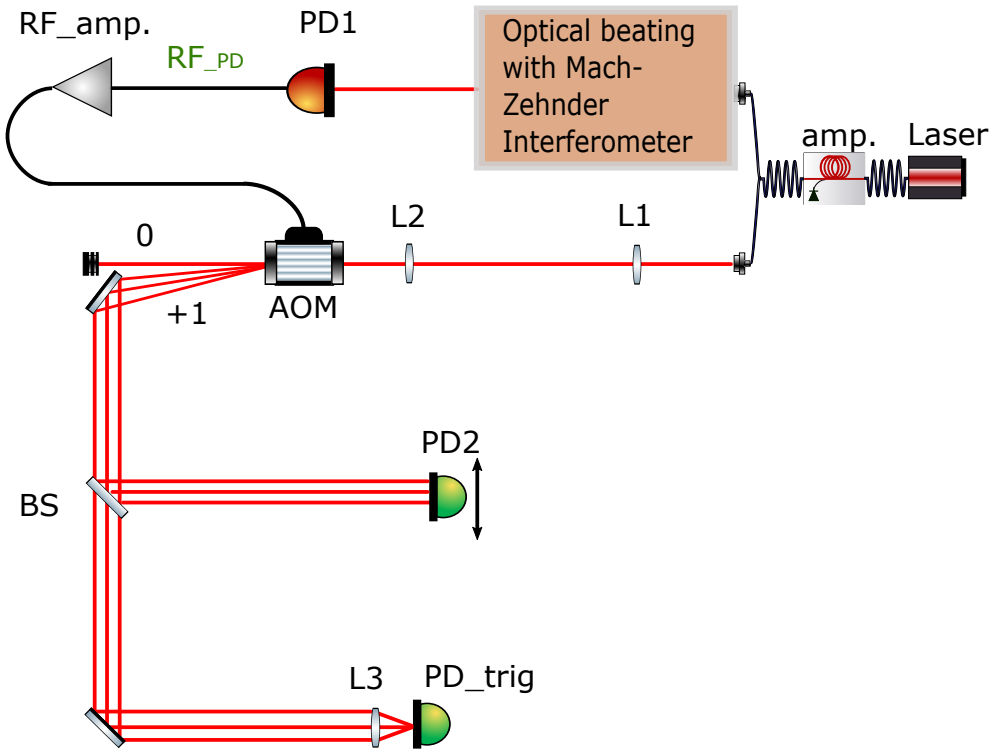

Fig. 4.10: Experimental setup of a fast deflection based on an AOM. The AOM driver is created optically in a Mach-Zehnder Interferometer as presented in 4.3.2. The laser beam is guided in a fiber and split into two arms. In one arm an optical beat note is created in a Mach-Zehnder Interferometer, which is converted into an electric signal $\mathrm{RF_{PD}}$ by a photodiode (PD). The electric signal $\mathrm{RF_{PD}}$ is amplified ($\mathrm{RF_{amp.}}$) and serves as driver of the AOM. The beam in the other arm is focused with two lenses L1 and L2 into the AOM. The zero order diffracted beam is blocked and the first order is split by a beam splitter (BS) into two arms in order to capture the beam with two photodiodes (PD2 and $\mathrm{PD_{trig}}$) at the same time. The photodiode PD2 is mounted on a horizontal translation stage to scan the horizontal deflection pattern, whereas $\mathrm{PD_{trig}}$ is used to have a common trigger for various scan positions of PD2

4.4.2 Results: Sinusoidal beam deflection

In the first step the AOM is analysed. An AOM from AA opto-electonics designed for amplitude modulation or fixed frequency shift is used at a driver frequency of 110 MHz. The acoustic velocity in the AOM crystal is 4200 m/s with a nominal rise time of 160 ns per 1mm beam diameter. Even though this AOM is not designed for deflection, we used it because it was available in our laboratory. This experiment has been done to get familiar with AOMs and their performance before adequate AOMs and AOM drivers were chosen and bought.

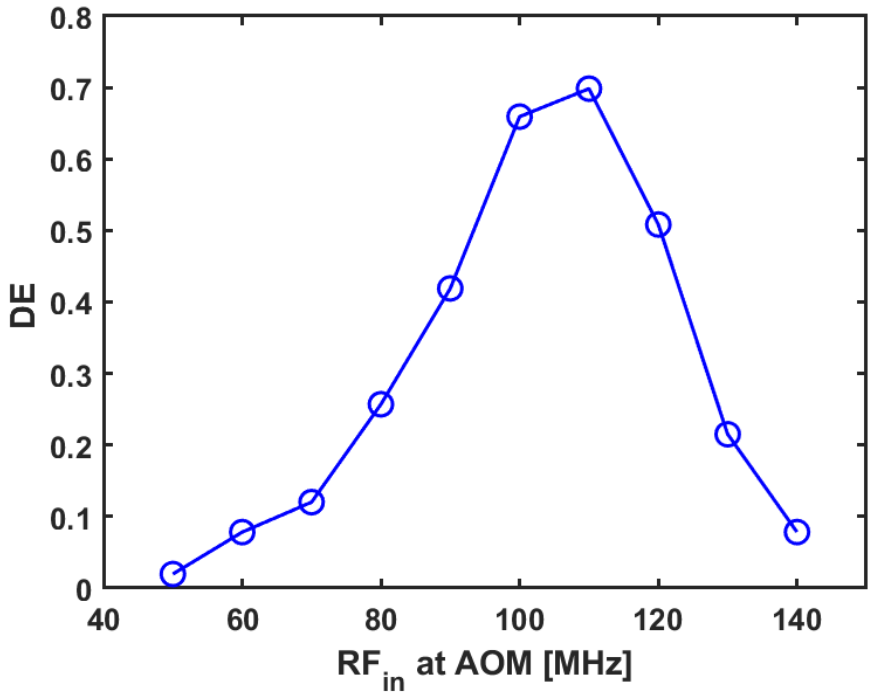

Fig. 4.11: Deflection efficiency (DE) of AOM (MT110-A1.5-1064 AA opto-electronics) as function of ($\mathrm{RF_{in}}$) at a RF input power of 33 dBm for a 240 µm waist diameter in the AOM.

The measured deflection curve of the used AOM is shown in figure 4.11. For this measurement the AOM RF input power is put to 33dBm, the maximal input power of the AOM and the beam waist diameter in the AOM is 240 µm. As expected the deflection efficiency has its peak at the driver frequency of 110 MHz and decreases fast around that driver frequency. From equation 4.9 we can calculate a scan angle of 2.5 mrad per $\Delta\nu_{car}$ = 10 MHz for this AOM. We can conclude that this AOM has only a small deflection range with an important deflection efficiency. The fact that the deflection curve is not symmetric around 110 MHz may be due to the design of the AOM-crystal and transducer. This AOM is designed for amplitude modulation or frequency shifting with a fixed carrier frequency. This explains the

fact that the deflection efficiency is only high at driver frequencies close to the carrier frequency.

In figure 4.12 the measured deflection pattern for different modulation frequencies ν_{mod} is shown. The deflection angle for the carrier frequency of 110 MHz is set as $\theta = 0$. The photodiode is moved in 500 µm steps along the deflection direction. At each position the temporal evolution of the intensity is measured with the same trigger which is retrieved from a reference photodiode (see fig. 4.10). The displayed deflection pattern is obtained by merging the single measurements. The photodiode has a distance of around 90 cm from the AOM which results in the shown deflection angles. These measurements were done with a beam waist diameter in the AOM of approximately 240 µm with a constant EOM input power of 28 dBm. The RF input power of 28 dBm at the phase modulator corresponds to $\phi_0 = 3.45$ rad, as shown in the results on figure 4.9.

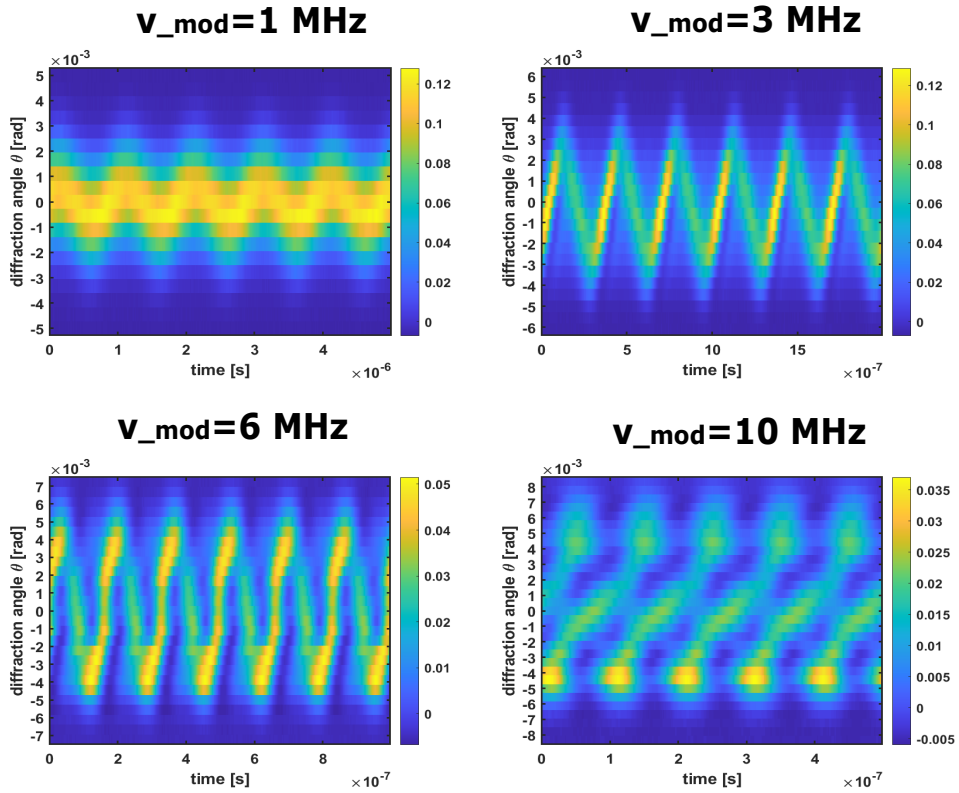

Fig. 4.12: Deflection pattern for a sinusoidal modulated driver signal of the AOM. The measurement is done with a $\mathrm{RF}_{\mathrm{mod}}$ input power of 28 dBm at the EOM and a beam diameter of around 240 µm. The carrier frequency is modulated with a frequency of $\nu_{mod} = 1$, 3, 6 and 10.(The unit of the color bar is arbitrary.)

We obtain a sequential deflection pattern with a sinusoidal modulation of several MHz. It can be seen that the scan angle increases with a growing modulation frequency from 4 mrad for ν_{mod} =1 MHz to around 12 mrad at ν_{mod} =6 MHz. This is due to the fact that the maximal frequency deviation is determined by the product

of $\phi_0\nu_{mod}$ (see eq. 4.19), which is growing as $\phi_0 = 3.45$ rad is constant for all measurements. A rather good sinusoidal deflection pattern for ν_{mod} less than 6 MHz has been measured. For modulation frequencies of 6 MHz and higher, the sequential beam deviation is not sinusoidal anymore. A reason could be the fact that the acoustic wave front in the AOM crystal can not be considered static anymore for high modulation frequencies. Thus, the optic beam in the AOM is diffracted at a moving acoustic wave with several instantaneous frequencies in its wave front. It seems that the modulation bandwidth of the AOM is smaller than 6 MHz.
One can also see that for a modulation frequency of 3 and 6 MHz the intensity of the beam moving in one direction is higher than for the opposite direction. This behavior seems to originate from the AOM.
Even though a residual amplitude modulation was measured in figure 4.8 with a modulation coefficient of $m = 0.15$, there is no visual effect in this acquired pattern: It cannot be seen, that the intensity in one deflection direction is higher than in the opposite direction. One reason could be the RF amplifier which is used to amplify $\mathrm{RF_{PD}}$, which flattens the amplitude modulation.

4.4.3 Results: beam deflection between two fixed angles

It is of interest to study also different deflection patterns, which is crucial in order to optimize PI mitigation, implying different unstable mode shapes with the radiation pressure of a deflected laser beam. A sinusoidal beam deviation is not necessarily the optimum. In the presented setup for AOM driver creation, one opportunity to change the deflection pattern consists in changing the waveform of the $\mathrm{RF_{mod}}$ input signal of the phase modulator. By driving the phase modulator for example with a triangular signal u(t) with an amplitude of ϕ_0 and a period of $\frac{1}{\nu_{mod}}$, we obtain a signal at the photodiode PD1 after the interferometer with

$$\mathrm{RF_{PD}} = A_{PD}\cos(\omega_{car}t + u(t)) \tag{4.27}$$

the resulting instantaneous frequency ν_i is

$$\nu_i(t) = \nu_{car} + \frac{1}{2\pi}\frac{d}{dt}u(t) \tag{4.28}$$

and since the derivative of a triangular wave equals a square wave, the resulting frequency will alternate between two fixed frequencies of

$$\nu_{car} \pm \Delta\nu_{car} \tag{4.29}$$

with a frequency deviation of $\Delta\nu_{car} = \phi_0\nu_{mod}$. Figure 4.13 shows the measured deflection pattern. The triangular wave at the input of the phase modulator has a fixed power level of 28 dBm with modulation frequencies of $\nu_{mod} = 1, 2, 4, 6.4$ and

10 MHz. The laser beam waist radius in the AOM is $w_b = 120$ µm. One can see again the increasing scan angle with the increasing modulation frequency, which is due to the increasing product of $\phi_0 \nu_{mod}$. Obviously, the beam does not stay only on two positions as expected but the deflection angle increases linearly after changing the position. This effect gets stronger as the modulation frequency raises. Its origin is either in the AOM response or in the fact that the RF amplifier deforms the triangular waveform, which is the driver signal of the phase modulator. The phase modulator has a nominal electro-optic bandwidth of 4 GHz, which should not be the limiting factor. The photodiode has a measured bandwidth of 200 MHz, which is also sufficient to acquire amplitude modulations between 80 and 130 MHz without deformation. The beam which is deflected in one direction (from negative to positive angle in the figure) has a lower intensity than the beam deflected in the opposite direction. It could be due to the amplitude modulation of the AOM driver signal. The deflection pattern at a modulation frequency higher than 10 MHz does not have a square wave form anymore. This seems to confirm the fact that the modulation bandwidth of this AOM for a beam waist radius of $w_b = 120$ µm is below 6 MHz.

4.4.4 Results: AOM modulation bandwidth

In order to measure the modulation bandwidth of the AOM, the photodiode PD2 (see fig. 4.10) is fixed to position $\theta = 0$, as shown in figure 4.14. The beam is deflected sinusoidally with different modulation frequencies ν_{mod} around $\theta = 0$, the diffraction angle for the carrier frequency of $\nu_{car} = 110$ MHz. Since the beam passes twice the photodiode during one period, the measured frequency equals twice the modulation frequency, as one can see on the inset. For this measurement the acquired data is measured with a spectrum analyzer. The power of the frequency peak $\nu = 2\nu_{mod}$ is measured and displayed for different modulation frequencies. The results are displayed in figure 4.15. In diagram A) one can see the frequency peak power of $\nu = 2\nu_{mod}$ as a function of the modulation frequency ν_{mod} for a fixed power level of $\mathrm{RF}_{\mathrm{mod}}$ input of the phase modulator of 20 dBm. This measurement is done for a beam waist radius of $w_b = 120$ and 500 µm in the AOM. The amplitude curve of $2\nu_{mod}$ for both beam radii has a maximum. It is for $w_b = 500$ µm at 2 MHz and for $w_b = 120$ µm at 3.3 MHz. For bigger modulation frequencies the AOM acts as a low pass filter.

The fact that for small modulation frequencies (0-2 MHz) the frequency peak of $\nu = 2\nu_{mod}$ is small is due to the fact that $\Delta\nu_{car}$ is defined by the product of $\phi_0 \nu_{mod}$, which is also small for small ν_{mod}, as ϕ_0 is constant. It means that the beam has a small scan angle and does not move from the photodiode. Consequently, the photodiode measures a weak AC component, but a high DC component.

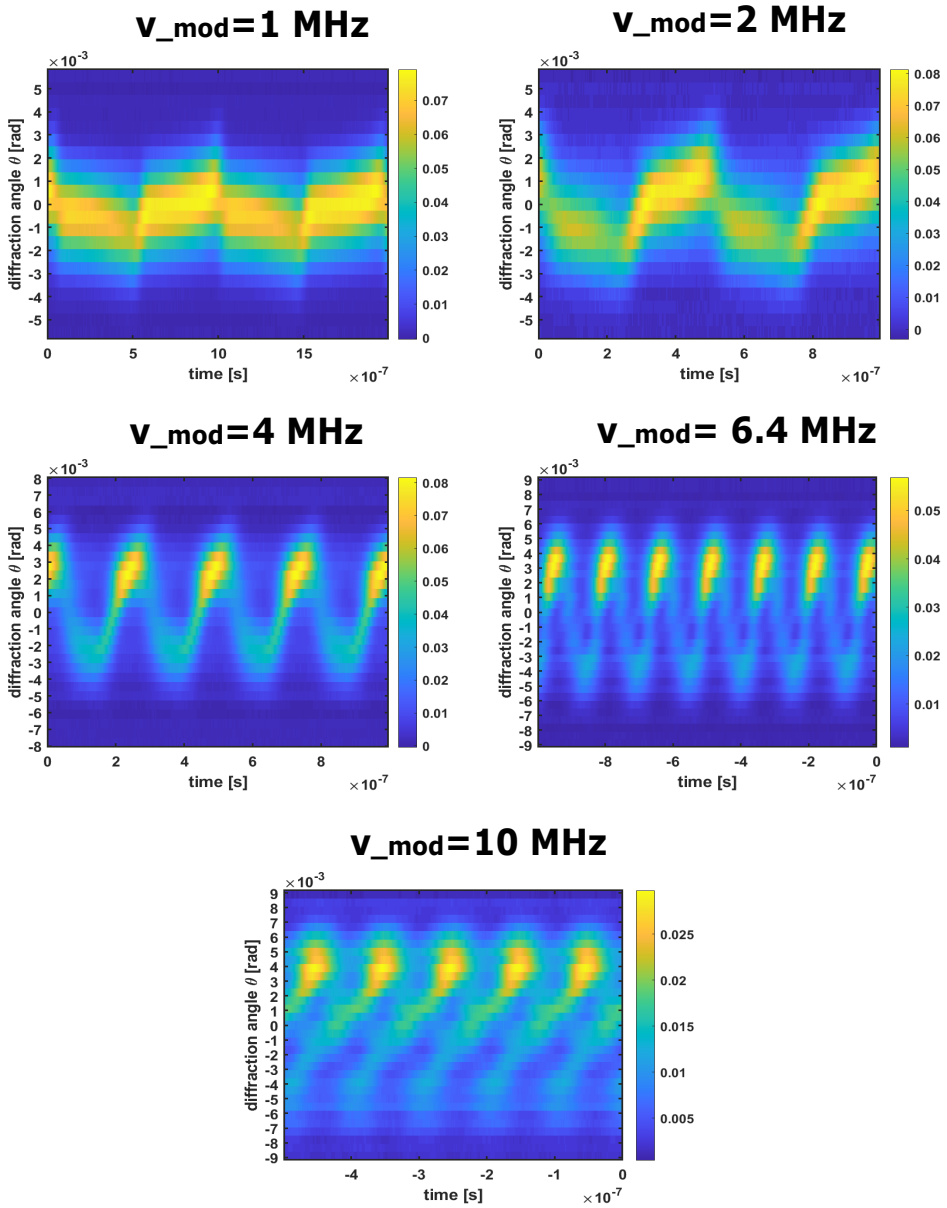

Fig. 4.13: Deflection pattern for a triangular modulated driver signal of the AOM. The measurement is done with an $\mathrm{RF}_{\mathrm{mod}}$ input power of 28 dBm at the EOM and a beam diameter of around 240 µm. The carrier frequency is modulated with a frequency of ν_{mod} = 1, 2, 4, 6.4 and 10. (The unit of the color bar is arbitrary.)

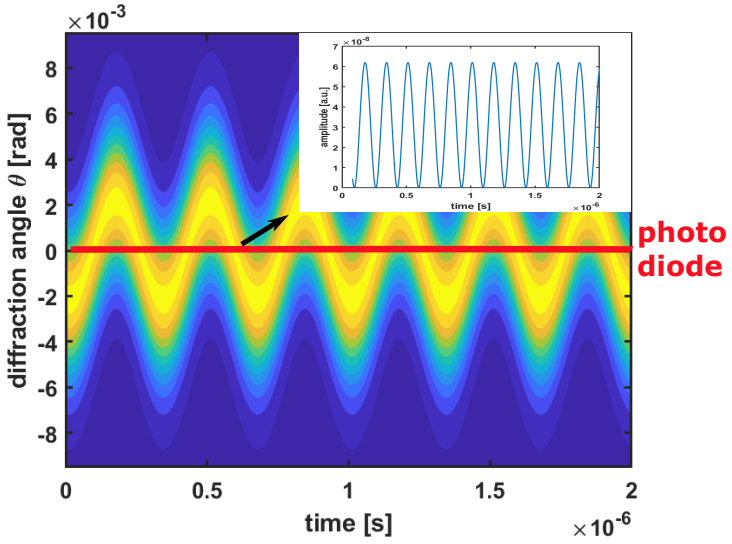

Fig. 4.14: Position of the photodiode PD2 in order to measure the modulation bandwidth of the AOM. The photodiode will see a modulation with $\nu = 2\nu_{mod}$, which is displayed in the inset.

As expected the modulation bandwidth of the AOM increases as the beam waist in the AOM decreases (see equation 4.8). A larger modulation bandwidth means that the AOM deflects with a higher rapidity. We measure a local minimum at 6 MHz for a beam waist of w_b= 120 µm. This behavior is due to the AOM and conforms to the measurement presented in figure 4.12, where one can see that the intensity at θ= 0 is really low for ν_{mod}= 6 MHz, compared to the modulation frequencies ν_{mod}= 3 and 10 MHz.

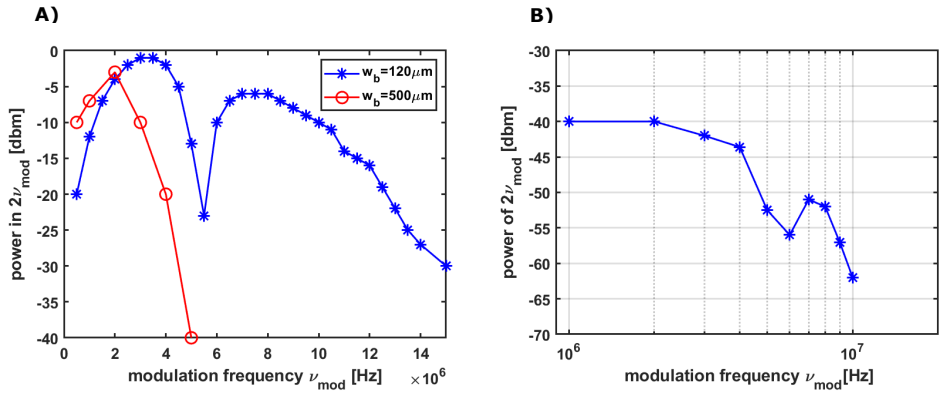

Fig. 4.15: Measured bandwidth of AOM. A photodiode is placed at θ= 0 (see figure 4.14) and the measured intensities are displayed with a spectrum analyzer. The power of the $2\nu_{mod}$-peak in the spectrum is measured as a function of the sinusoidal modulation frequency ν_{mod} of the AOM driver signal. A) Measured power for a constant phase modulator input power of 20 dBm at beam waist radius of w_b= 120 and 500 µm. B) Measured AOM bandwidth for w_b=120 µm for a constant product of $\phi_0\nu_{mod}$ with a power level of 28 dBm of $\mathrm{RF_{mod}}$ at ν_{mod}= 1 MHz.

In order to better visualize the low pass behavior of the AOM, the same measurement is done for the beam waist radius of w_b=120 µm for a constant scan angle for all

modulation frequencies, by keeping the product $\Delta\nu_{car}$ constant. Figure 4.15 shows the result for a power level of 28 dBm at the RF input of the phase modulator for $\Delta\nu_{car} = 1$ MHz. The power of the measured modulation frequency after the AOM stays constant (within 3dB) up to 4 MHz and then decreases for higher modulation frequencies with a local minimum at 6 MHz. It confirms the fact that the modulation bandwidth of the AOM for w_b= 120 µm is at 4 MHz. The manufacturer of the AOM states an analog modulation bandwidth for amplitude modulation of 10 MHz for a spot diameter of 300 µm, but obviously the bandwidth of frequency modulation of the AOM is lower. The power decreases for ν_{mod}> 4 MHz with a higher slope than -20 dB per decade, which means that the AOM acts as a low pass filter of higher order than one for the modulation of the driver frequency.

4.4.5 Conclusion

Rapid sinusoidal beam deflection with an AOM in one dimension is demonstrated. The fast modulated AOM driver signal is generated optically in a Mach-Zehnder interferometer and converted via heterodyne detection into an electic signal. The rapidity is limited by the modulation bandwidth of the AOM to 4 MHz at a beam waist radius of 120 µm. The maximal scan angle for a modulation frequency of 1 MHz is around 4 mrad increasing up to 12 mrad for a modulation frequency of 6 MHz. The maximal scan angle is limited by the maximal possible phase shift generated by the phase modulator in the Mach-Zehnder Interferometer. A periodic deflection between two fixed angles has been setup by driving the phase modulator with a triangular waveform. The beam does not stay on the two deflection angles, but has a linearly increasing deflection angle. An asymmetry in the intensity of both deflection angles has been observed. This could be due to an amplitude modulation of the driver signal of the AOM, even though no visual effect of it has been observed for sinusoidal deflection in figure 4.12.

The presented system is rapid but complex. It would be necessary to further investigate many aspects , such as for example the impact of the phase modulator's RAM on the deflection pattern and the beam deflection between two fixed angles, in order to implement such a system for the proposed flexible active mitigation strategy of PI. The investigated deflection system shows well defined deflection patterns within the modulation bandwidth of the AOM for sequential deflection, but it is limited to small scan angles of some mrad. The scan angle is limited by the maximal $\mathrm{RF}_{\mathrm{mod}}$ input power of the phase modulator. Arbitrary beam deflection between distinct directions has not been achieved, and is not well understood.
The expansion to 2D deflection would require an additional RF generation system in order to drive the X- and Y-deflection independent. This would increase the necessary space and the complexity of this deflection system. For a flexible active

mitigation strategy of PI, as discussed in the previous chapter, it is desirable to investigate another solution for both the driver signal generation and the AOM used for deflection.

4.5 Generation of fast modulated RF signals based on a software-defined radio

In the previous section a modulated AOM driver signal was created, which has been used for sequential beam deflection for modulation frequencies up to 10 MHz. For our flexible active damping system of PI it is desirable to have an arbitrary beam deflection. The creation of fast arbitrary changing radio frequencies which drive the AOM is a challenge. As already mentioned in section 4.2.1, the use of DDS is also limited to commutation frequencies below 1 MHz, which is not sufficient for our application. In this section a software-defined radio platform is investigated to explore its capability to generate radio frequencies with small commutation times.

4.5.1 RF generation setup

We used a Universal Software Radio Peripheral (USRP X310,KINTEX7-410T FPGA, 2 channels, 160 MHz bandwidth each channel, dual 10 Gigabit ethernet, Ettus Research) a software-defined radio platform for the radio frequency generation. It is capable of receiving or transmitting modulated radio frequencies with a high sample rate. In figure 4.16 a picture of the USRP is shown and figure 4.17 depicts its hardware architecture when this device is used for RF generation. The USRP consists

Fig. 4.16: USRP X310 with two input and output channels. (picture taken from [124])

of a large Field Programmable Gate Array (FPGA) with two daughterboards. The FPGA is responsible for the data packet routing, the data transmission control and the digital up conversion of the data to the set carrier frequency. The original FPGA receives the data from a network connection over two direct memory access first-in first-out (DMA FIFO) components. Each daughterboard has digital analog converters with lowpass filters capable of generating analog frequencies in a range from 10 MHz to 6 GHz with a bandwidth of 160 MHz based on In-phase (I) and Quadrature

(Q) data. It has a nominal sample rate of 200 MSamples/s which permits changing the emitted frequency theoretically within 5 ns.

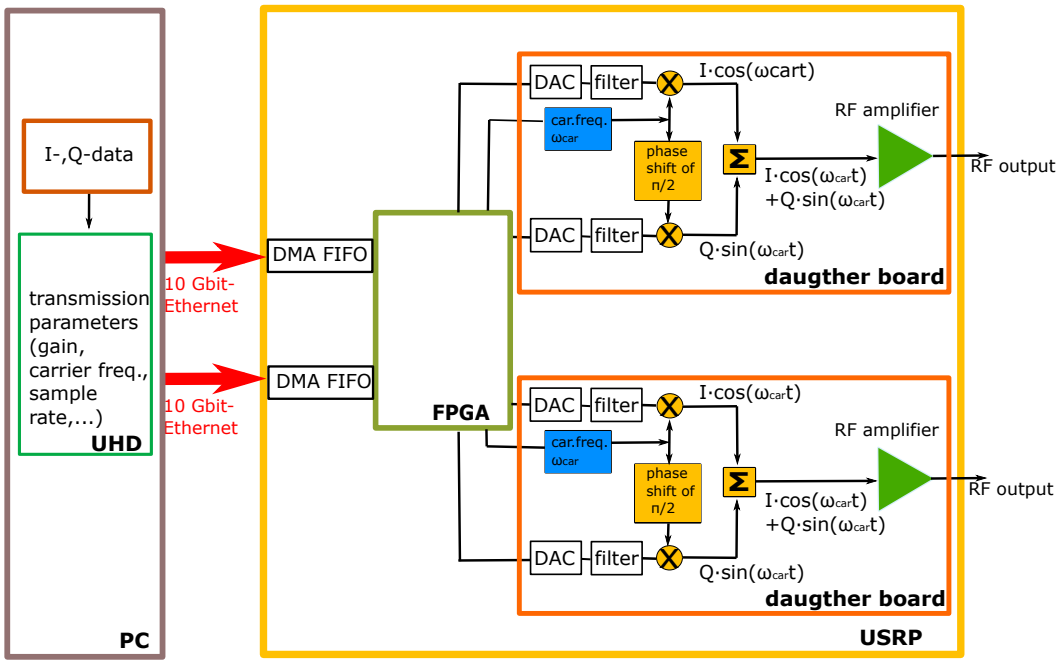

Fig. 4.17: Hardware architecture of an USRP used for RF generation. (figure based on [125])

The USRP is interfaced with the USRP Hardware Driver™ (UHD) software on a linux machine Dell Precision 5820. In UHD the RF generation parameters can be set as for example the carrier frequency and the gain. But it sets also the data transmission parameters like the sample rate. A dual 10 Gigabit ethernet connection between the USRP and the host is established to enable a 2 x 200 Msamples/s transmission with 32 bits per sample (total data transfer of 1.6 GB/s). To enable the highest streaming rates over a network connection, a list of configurations is needed to be set on the host: The CPU governor is set to performance and priority scheduling is enabled to use the whole CPU capacity for the data transmission. The network buffers are set to a maximal value of 625,000,000 bits and jumbo frames of 8000 bytes are set as maximal transmission unit (MTU) for the network transaction layer to maximize the data throughout. For further acceleration a data transport based on data plane development kit (DPDK), which uses user space memory buffers for the data communication over an network interface, is set up. On the USRP side the shipped FPGA image has been modified by adding two additional FIFO buffers to enlarge the bandwidth of the already existing direct memory access FIFO buffer and DPDK transmission has been enabled.

In order to generate an arbitrary angular frequency $\omega_1 = 2\pi\nu_1$ with the USRP with an angular carrier frequency $\omega_{car} = 2\pi\nu_{car}$ the I- and Q-data need to be described by the function

$$I(t) = \cos((\omega_{car} - \omega_1)t) \tag{4.30}$$

$$Q(t) = \sin((\omega_{car} - \omega_1)t) \tag{4.31}$$

The generated radio frequency $\mathrm{RF_{out}}$ equals

$$\mathrm{RF_{out}} = I\cos(\omega_{car}t) + Q\sin(\omega_{car}t) \tag{4.32}$$

and putting eq. 4.30 and eq. 4.31 in eq.4.32 gives

$$\mathrm{RF_{out}} = \cos((\omega_{car} - \omega_1)t)\cos(\omega_{car}t) + \sin((\omega_{car} - \omega_1)t)\sin(\omega_{car}t) \tag{4.33}$$

which can be rewritten as

$$\mathrm{RF_{out}} = \frac{1}{2}\left[\cos((2\omega_{car} - \omega_1)t) + \cos(\omega_1 t)\right] + \frac{1}{2}\left[\cos(\omega_1 t) - \cos((2\omega_{car} - \omega_1)t)\right] \tag{4.34}$$

It results in

$$\mathrm{RF_{out}} = cos(\omega_1)t \tag{4.35}$$

The I- and Q- data for several arbitrary frequencies with their specified duration is saved in a file. When the self-programmed UHD-code is launched, the I- and Q-data is emitted continuously in a loop to the USRP, which generates the radio frequencies continuously in a loop.

4.5.2 Results

In a first step two frequencies are generated alternating every 200 ns. A sample of the USRP's emitted signal with a frequency of 160 MHz and 290 MHz is shown in fig. 4.18(a). Two frequency transitions are visible and are zoomed-in in fig. 4.18(b). A clean oscillation can be seen for both frequencies. The amplitude of the oscillations of a single frequency is stable, but a small amplitude change between the 160 and 290 MHz oscillation is apparent.
To describe the frequency transition and to determine the commutation time, the emitted signal is modeled. The stationary frequency oscillation of 160 and 290 MHz is fitted first to the function S_0(t) and S_1(t)

$$S_{0,1}(t) = a_{0,1}\sin(2\pi f_{0,1}t + \phi_{0,1}) \tag{4.36}$$

respectively with the amplitude $a_{0,1}$, the frequency $f_{0,1}$ and the phase $\phi_{0,1}$. The fit parameters are presented in table 4.1. An amplitude difference between both frequencies of around 6% can be determined. There is the possibility to set the

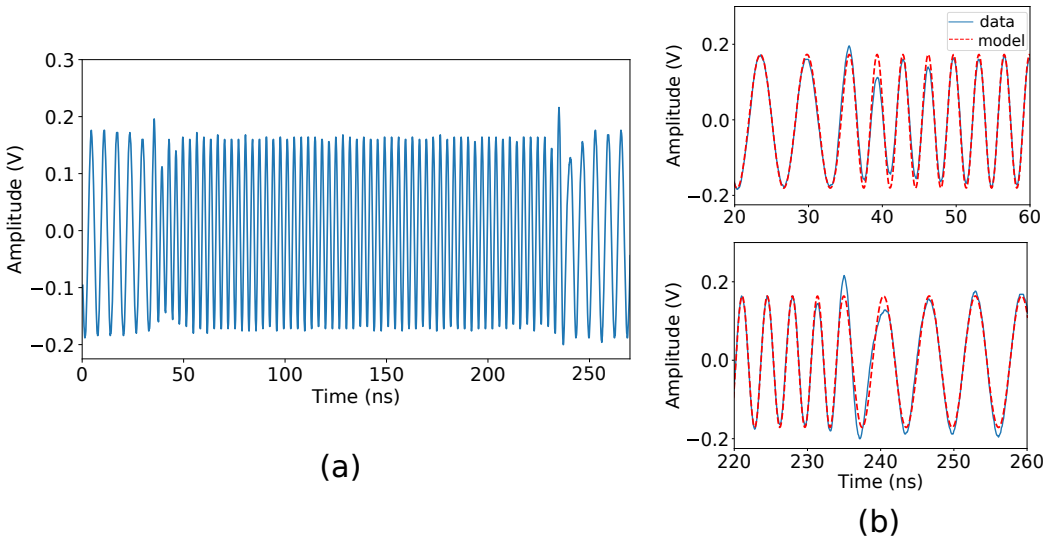

Fig. 4.18: (a) Portion of the signal emitted by the USRP. The frequency changes every 200 ns between 160 and 290 MHz. (b) Zoom on the frequency transitions: 160 to 290 MHz (top), 290 to 160 MHz (bottom). An exponential function is used to model the frequency switch, the fit is plotted in red dashed lines.

amplitude of each generated frequency in the I/Q-data file. It can be used to equalize the amplitude of the generated radio frequency, as will be demonstrated later in section 4.6.2. It is noticeable that there is a discrepancy of less than 1% between the set frequencies of the USRP and the values of f_0 and f_1 obtained by the fit. This can be explained by the fact that the oscilloscope used for the acquisition had not been synchronized with the USRP clock.

Tab. 4.1: Fit parameters of the stationary signals S_0 and S_1 (Eq. 4.36)

S_0	Fit value	S_1	Fit value
a_0	177.3 ± 0.4 mV	a_1	167.2 ± 0.2 mV
f_0	158.37 ± 0.04 MHz	f_1	291.66 ± 0.02 MHz
ϕ_0	3.340 ± 0.004 rad	ϕ_1	- 1.445 ± 0.002 rad

The emitted signal of the USRP is modeled by a sinusoidal function $S(t)$

$$S(t) = a \sin \phi(t) \tag{4.37}$$

with a constant amplitude $a = a_0$ for the first transition in figure 4.18a) and $a = a_1$ for the second transition and a time varying argument $\phi(t)$ of the sine function. We suppose that during both frequency transitions the frequency f varies from the initial respective frequency $f_{0,1}$ to the final frequency $f_{1,0}$, following an exponential decay, which starts at a given time t_s:

$$f(t > t_s) = f_{0,1} + (f_{1,0} - f_{0,1}) \left(1 - \exp^{-\frac{t-t_s}{\tau}}\right) \tag{4.38}$$

The decay constant τ represents the frequency transition time. With eq. 4.38 $\phi(t)$ can be derived for both transitions respectively

$$\phi(t > t_s) = 2\pi f_{0,1} t + (f_{1,0} - f_{0,1})\tau \left(\frac{t - t_s}{\tau} + e^{-\frac{t-t_s}{\tau}} - 1 \right) + \phi_{0,1} \tag{4.39}$$

The two frequency transitions are fitted to eq. 4.37, setting the parameters of table 4.1 as constant and keeping τ and t_s as free parameters.
According to this model the characteristic transition time is 2.21 ± 0.05 ns for the frequency change from 160 to 290 MHz and 1.74 ± 0.06 ns for the change from 290 to 160 MHz. The modeled frequency transition is plotted to the experimental data in figure 4.18(b). The agreement between fit and data is good even though this model does not take into account the amplitude variations. It can be determined in the plots that the amplitude takes about 15 ns to stabilize.

A measurement of the spectrum of the emitted radio frequency is illustrated in figure 4.19. It has been measured with a spectrum analyzer. The emitted frequency is 220 MHz. As already mentioned the I/Q-data are saved in a file describing a waveform of a predefined length. The file used for this RF generation describes a waveform of 10 µs duration, which is continually sent to the USRP by the UHD-code. The frequency

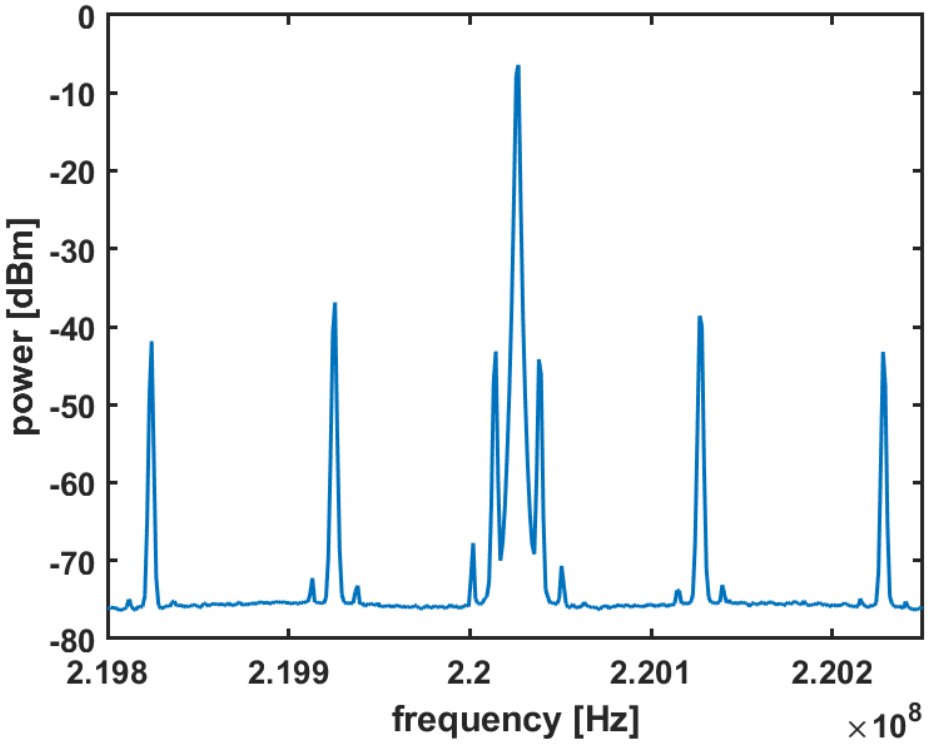

Fig. 4.19: Measured spectrum of a 220 MHz frequency with the USRP in the setup depicted in figure 4.17 using a data file describing a waveform of 10 µs duration.

peak of the emitted frequency has a power of -7 dBm and is at 220.026 MHz. It

confirms the precise frequency generation of the USRP with a relative error of 0.01% to the set frequency. Additional side band peaks with a distance of 100 kHz can be seen. It is due to the fact that the USRP generates for each 10 µs the same data again. Indeed, each time the I/Q-data of a file is generated again, the amplitude of the emitted RF signal oscillates in a similar way as seen at each frequency change (see figure 4.18 and 4.20). This amplitude modulation is visible in the spectrum and is at least 30 dB (0.1%) weaker than the power of the radio frequency. There are also peaks with a distance of 12 kHz around the main radio frequency visible (-37 dB) that can not be associated to a specific parameter of the RF generation.

The manufacturer defines a bandwidth of 160 MHz for both daughterboards, which corresponds to a frequency deviation $\Delta\nu_{car}$ of 80 MHz from the carrier frequency. Figure 4.20 depicts four measured radio frequencies emitted with the USRP. The carrier frequency is 225 MHz. Each frequency is generated for 50 ns before switching to the next one. The amplitude decreases from the 145 MHz to 130 MHz signal

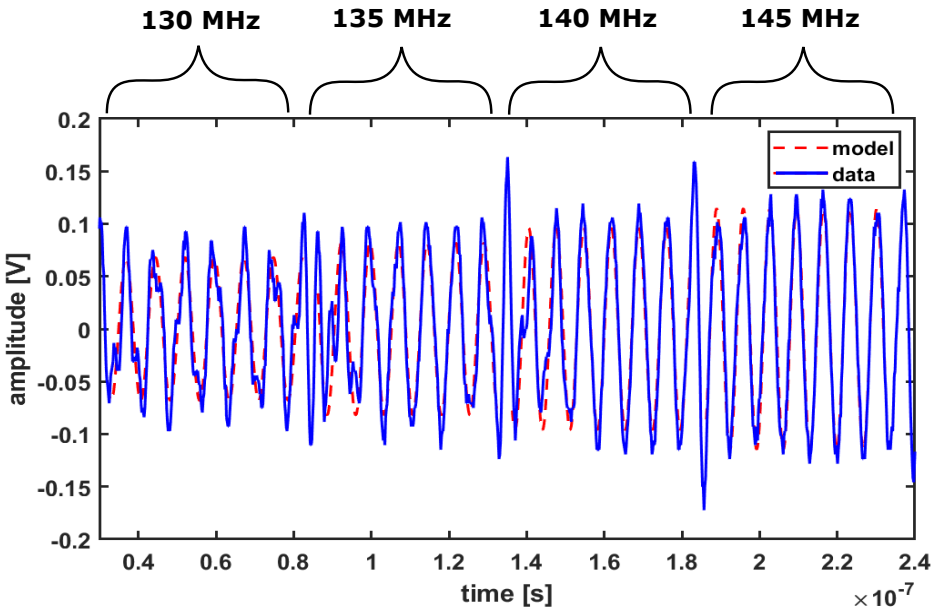

Fig. 4.20: An emitted signal by the USRP with four different frequencies for a carrier frequency of 225 MHz. One frequency is emitted during 50 ns before switching to the next one. Each emitted frequency f_i (excluding the transition) is fitted to a function $S_i(t) = a_i \sin(2\pi f_i t + \phi_i)$ and is plotted in dashed red line.

since we attain the bandwidth limit of the USRP. One can also see that the generated signal for 130 and 135 MHz which corresponds to $\nu_{car} - \nu_1 = 95$ and 90 MHz respectively is deformed. The amplitude for the generated frequency of 140 and 145 MHz is bigger and proper oscillations can already be seen for these frequencies. The plotted model to this measurement is the fit of each generated frequency to the function $S_i(t) = a_i \sin(2\pi f_i t + \phi_i)$, neglecting the transition between the signals.

Since the acoustic bandwidth of the AOM, which will be investigated in the next

Tab. 4.2: Fit parameters of the four signals depicted in figure 4.20 to the function $S_i(t) = a_i \sin(2\pi f_i t + \phi_i)$

S_0	Fit value	S_1	Fit value
a_0	68.21 ± 3.74 mV	a_1	82.02 ± 4.41 mV
f_0	131.8 ± 0.6 MHz	f_1	136 ± 0.6 MHz
ϕ_0	2.5024 ± 0.2303 rad	ϕ_1	- 1.919 ± 0.428 rad
S_2	Fit value	S_3	Fit value
a_2	96.14 ± 3.8 mV	a_3	114.8 ± 2.3 mV
f_2	141 ± 0.5 MHz	f_4	145.5 ± 0.2 MHz
ϕ_2	2.6877 ± 0.4758 rad	ϕ_3	- 1.512 ± 0.304 rad

section, equals 130 MHz, there was no need to modulate the carrier frequency more than 65 MHz.

4.5.3 Conclusion

A USRP in combination with a high performance PC is used to generate discrete radio frequencies with small commutation times on two channels. For this purpose the FPGA of the USRP is modified and a network connection with a high bandwidth of 1.6 GB/s with a PC is established. Predefined radio frequencies with an arbitrary duration and amplitude can be generated with a precision of tens of kHz. A commutation time of 2.2 ns and an accompanying amplitude modulation at each frequency change of approximately 15 ns duration has been measured. A carrier frequency in the range from 10 MHz to 6 GHz can be emitted with a modulation bandwidth of 160 MHz. The analysis presented in this section confirms that the USRP fulfills the requirements regarding the AOM's driving signal: it provides RF signals in random access with a transition time τ much lower than the AOM rise time. The speed of a deflection device will be then limited by the AOM response as we will see in the next section.

4.6 Fast 2D beam deflection with driver signal generated with software-defined radio

In this section a rapid 2D beam deflection system is presented, based on the driver signal generated by the USRP. Two AOMs are used comprising the rapidity of an AO modulator and the large deflection angle of an AO deflector. Fast laser scanning with acousto-optic modulators has been investigated in the past for television projection [111], in microscopy [126] and imaging systems [127] as well as in beam shaping systems [128]. In this context it is investigated as part of an active mitigation strategy of parametric instabilities. Key parameters for our application, such as

for example the deflection efficiency in the whole scan range, the rapidity and the deflection in high optical power regime are investigated.

4.6.1 Optical setup

In this experiment two AOMs (Gooch & Hausego AODF-4224-2, 34 mrad deflection range, 130 MHz acoustic bandwidth) are lined up orthogonal to each other (referred to as X-AOM and Y-AOM). Those AOMs are chosen, because they are a compromise between AOMs designed for amplitude modulation and the ones designed for deflection, as they fulfill both requirements of high speed (33 ns of rise time) and of large scan range (34 mrad). Each AOM has two RF inputs with a differential delay of 4.6 ns between both inputs in order to increase the diffraction efficiency (see section 4.2). The driver signal of each AOM is amplified with an RF-amplifier (RF Bay, Inc., MPA-40-40). Figure 4.21 shows the optical setup. As a laser source a 10 mW seed laser (NKT Photonics Koheras Adjustik), with a wavelength of $\lambda = 1064$ nm, is used. It is amplified with a fiber amplifier that has a maximum output power of 50 W. With the set of two lenses (L1+L2) the beam is focused into the X-AOM to a diameter of 190 µm. As the casing of both AOMs is relatively big and the active aperture of 300 µm is too small to put one AOM directly behind the other, additional optical components are needed between the AOMs. For this reason an imaging lens L3 with a focal length $f = 200$ mm is placed between the X- and Y-AOM with a distance of 2f-2f to image the beam spot of the X-AOM with unity magnification into the Y-AOM. L3 is put into the optical axis of the first order diffracted beam at the central acoustic frequency of the AOM (225MHz). With a camera (CCD Camera Beam Profiler, BC106N-VIS/M, Ø30 µm - 6.6 mm, 350 - 1100 nm), the diffracted beam profile is captured and analyzed.

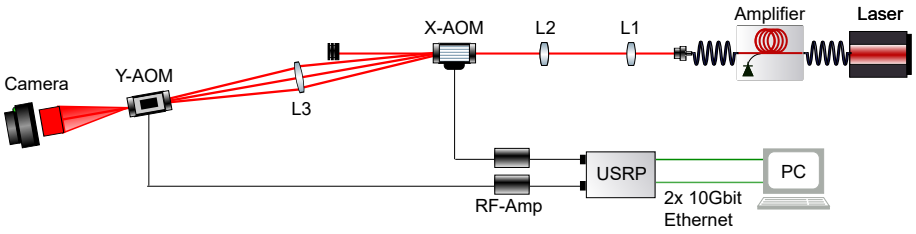

Fig. 4.21: Experimental setup. The seed laser is amplified and focused with lenses L1 and L2 into the X-AOM. The zero-order diffracted beam is blocked with a beam damp. Lens L3 serves as imaging lens to enter the horizontal deflected beam spot into the Y-AOM. The 2D deflected beam is captured with a camera. The driver signal for both AOMs is compiled with a PC, sent via dual 10 Gbit Ethernet connection to the USRP, which creates the radio signals. These get amplified with RF amplifiers (RF-Amp) before being sent to both AOMs.

For the choice of the imaging lens L3 a couple of factors need to be taken into account. Figure 4.22A) depicts a simplified schematic of the 2f-2f imaging configuration with

the propagation of a Gaussian beam. The beam waist radius w_0 of the incoming focused laser beam is in the center of the X-AOM at z_0. L3 is put in at a distance of twice its focal length behind the X-AOM. In this way the geometrical conjugate plane is at z_c, whereas the beam waist after crossing L3 has its waist w_1 at z_{w1}. In figure 4.22B-C) the simulated distance $z_{w1} - z_c$ and the Rayleigh length of the final beam is plotted for different focal lengths f of L3 for Gaussian beam propagation with an initial waist of $w_0 = 95$ µm. It can be seen that the Rayleigh length increases, whereas the distance $z_{w1} - z_c$ decreases by increasing the focal length f of the lens. If this difference is close to or larger than the Rayleigh length of the final Gaussian beam, it will affect the deflection efficiency of the Y-AOM, since the incoming beam does not have a flat wave front. Thus, it seems reasonable to choose a lens with large focal length. But, on the other hand, a large focal length demands a large lens diameter in order to collect the entirety of the deflected beams at a distance of 2f after the X-AOM. It is also desirable to keep the deflection system small and compact. The simulation shows that for a lens with focal length of f = 200 mm, the final waist lies 4 mm before the geometrical conjugate plan, which is acceptable, as it is within the Rayleigh length of 26 mm for a spot waist diameter of 190 µm. A lens diameter of 2 inches is large enough to collect the deflected beams. Another possible configuration for unity magnification imaging of the beam spot consists in using a set of two lenses with the same focal length f in a 4f imaging system [129]. But it is not practicable to find two lenses with the exact same focal length which would result in a spot magnification unequal to one.

4.6.2 Deflection efficiency

At a first step, the deflection efficiency of a single AOM is measured for different beam waists and for different relative positions of the AOM to the beam waist position, in order to characterize the AOM. Figure 4.23 shows the measured curves for an AOM driver power of 2.7±0.4 W. In order to change the beam waist in the AOM, the position of lens L2 is changed. The beam diameter is measured with a camera at several positions behind the AOM to obtain the actual beam waist in the AOM via a fit. In subplot A) one can see that the deflection efficiency curve is apparently unchanged for a beam waist diameter of $2w_0 = 200$ µm $\pm$ 30 µm. It gives the opportunity to change the beam waist, which will change the divergence of the Gaussian beam without decreasing the DE.
In a next step the beam waist is fixed to a diameter of 206 µm and the relative position of the AOM to the beam waist is changed. The result is shown in subplot B). The beam with this waist has a Rayleigh length of 31 mm, which means that the beam radius is increased by a factor of $\sqrt{2}$ at a distance of 31 mm from the beam waist position. Close to the beam waist the optical beam can be considered as parallel. The measured DE curves only stay unchanged when the center of the

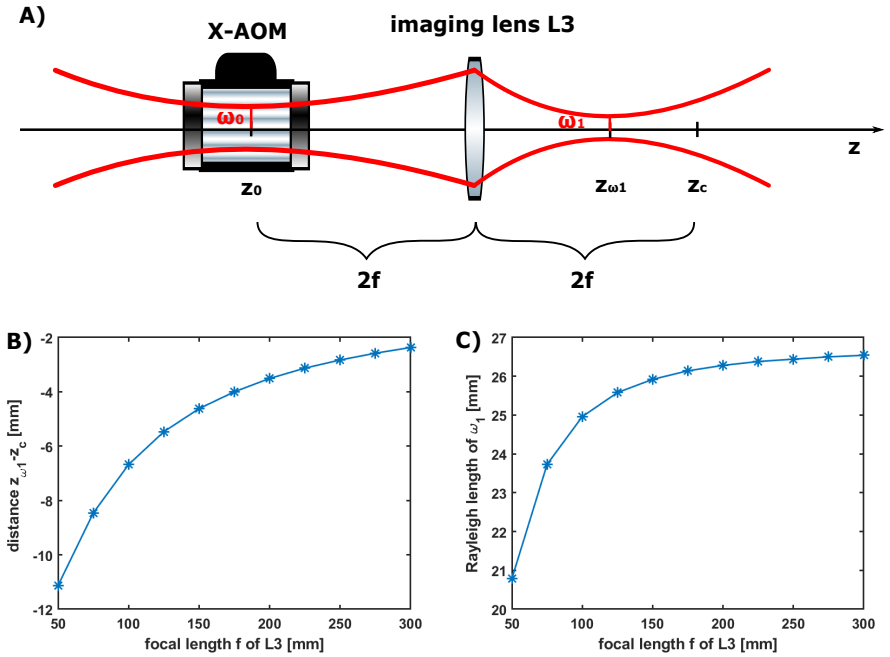

Fig. 4.22: 2f-2f unity magnification system for spot imaging of the X-AOM into the Y-AOM. A) The diffracted Gaussian beam with beam waist radius w_0 at z_0 in the X-AOM crosses the imaging lens L3. In a distance 2f behind L3 the geometrical conjugate plane of the spot is at z_0. The beam waist w_1 at z_{w1} is before z_c. B+C) Simulation of distance $z_{w1} - z_c$ and the Rayleigh length of w_1 for different focal lengths f of L3. The simulation is based on Gaussian beam propagation with beam waist radius w_0=95 µm.

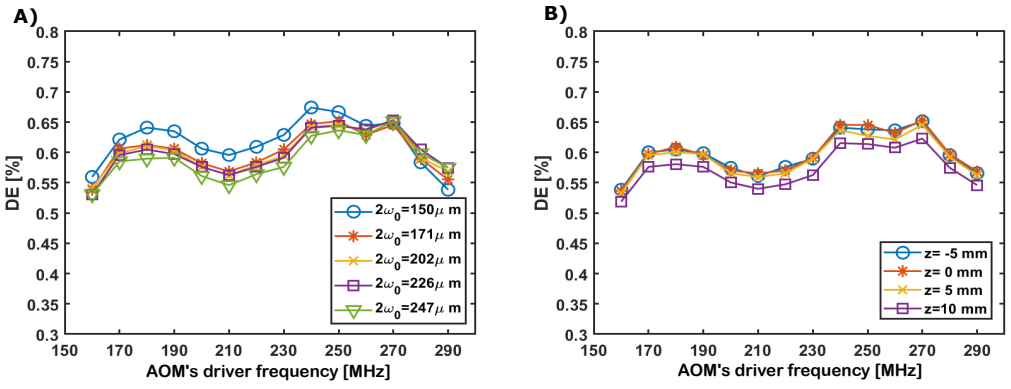

Fig. 4.23: Deflection efficiency as function of the driver frequency for different beam waists in the AOM A) and for different AOM positions compared to the beam waist position with w_0=103µm B) with an AOM RF driver power of 2.7±0.4 W.

AOM stays in a margin of ±5 mm around the waist position and decreases when the distance between the center of the AOM and the beam waist is larger. Apparently, the DE decreases already at small divergence angles of the beam, even within the Rayleigh length of the beam.
For further measurements the beam waist is set to 95 µm and the center of the beam waist is centered in the AOM.
Both AOM are mounted on a multi-axis stage to optimize the tip tilt and rotation angle for a flat deflection efficiency curve in the whole acoustic bandwidth of the modulator i.e. from 160 to 290 MHz. The dependence of the deflection efficiency on the rotation, tip and tilt angle of the AOM is presented in figure 4.24. Subplot A) shows the AOM with the corresponding rotation, tip and tilt angles respectively α, β and γ. The subplot B) depicts the DE curve for different rotation angles. For this measurement an RF power of 2.7±0.4 W is set while focusing the beam to a spot diameter of 190 µm in the AOM. The DE of the diffracted beam is the most sensitive to the rotation angle. The chosen rotation angle of the AOM, with the flattest curve

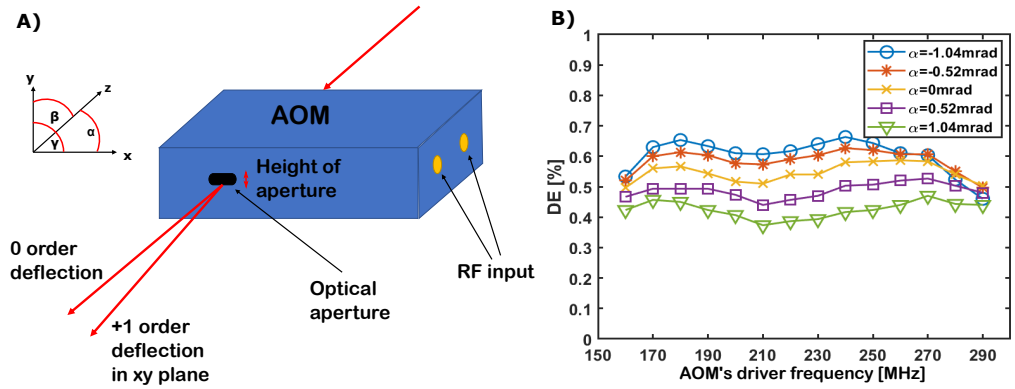

Fig. 4.24: Deflection efficiency as function of the driver frequency for different rotation angles of the X-AOM. A) Schematic of AOM B) DE curves for different rotational angles α for a beam waist diameter of 190 µm and a driver RF power of 2.7±0.4 W

at the largest possible scan angle, is set as $\alpha = 0$. By rotating the AOM towards negative angles of α, the DE for driver frequencies from 170 to 250 MHz is above 60 % but decreases under 50 % for driver frequencies higher than 250 MHz. By rotating the AOM in the opposite direction, the whole DE curve decreases.

In the next step, the X-AOM is used to deflect a laser beam with a beam waist of $w_0 = 95$ µm in the horizontal plane. A set of driver frequencies for both AOMs is chosen in such a way as to match as many deflection spots as possible in the whole scan range. Far beyond the Rayleigh length, the ratio of the scan angle $\Delta\theta$ to the beam divergence $\delta\theta$ defines the number of resolvable spots in 1 dimension. For an

acoustic bandwidth $\Delta\nu_b$ = 130 MHz of the AOM, the scan angle $\Delta\theta$ for isotropic diffraction is obtained from equation 4.6

$$\Delta\theta = \frac{\lambda_L \Delta\nu_{RF}}{V_a} = 33mrad \tag{4.40}$$

for the acoustic velocity $V_a = 4200\frac{\mathrm{m}}{\mathrm{s}}$. It is in accordance with the scan range of 34 mrad defined by the manufacturer. The full-angle divergence $\delta\theta$ of a Gaussian beam in far field, with a waist radius of w_1 = 95 µm, is

$$\delta\theta = \frac{2\lambda_L}{\pi w_1} = 7.1mrad \tag{4.41}$$

The ratio $\frac{\delta\theta}{\Delta\theta}$ equals 4.6 ≈ 5. But since the scan range of $\Delta\theta$ refers to the center of the Gaussian beam, there is one additional spot covered by the scan range. Figure 4.25 shows the horizontal deflection pattern with 6 positions, taken with a camera with a long exposure time, compared to the duration the beam stays on each position. As the image of the camera is superposed with interference due to filters that are mounted on the camera, the image is filtered later on. Figure 4.25B) shows the image after filtering out high spatial frequencies in the image.
Subplot D) shows the intensity profile of the 6 spots along the red line shown in subplot C). The minimal intensity between consecutive spots measures less than 36%. It corresponds to the intensity of less than 18% of a single spot. Thus, the distance between two consecutive beam spots corresponds approximately to the beam diameter (at 13% of the peak's amplitude). One can see in subplot D) that the intensities of each spot vary within 20%. By adjusting the RF power of each driver signal, an even flatter DE curve can be obtained. This can be done in the I/Q-data for the RF generation with the USRP. In order to obtain the correction factor for each AOM driver frequency, two different approaches were tested. One option is to take the peak intensity of each spot of the captured image B) or C) and calculate a correction factor for each driver frequency based on the intensity of the spot with the lowest intensity. A second approach consists in measuring the optical power of the deflected beam on each position and calculating the correction factors based on the beam with the lowest DE.
Figure 4.25E) shows the horizontal scan pattern with the corresponding AOM driver frequencies after adjusting the RF power. Based on the lowest deflected optical power, measured with a power meter, the needed RF power for each driver frequency is calculated, set in the I/Q-data and adjusted by measuring the new deflected beam power again. Figure 4.25F) shows the normalized optical power of each deflected beam shown in E), measured with a power meter. The normalized peak values of each spot shown in E) are also depicted. One can see that even if the optical power measured with a power meter is equal for each deflected beam, the peak intensities in image E) still vary within 10%. Thus, the approach to take the peak values of the spots in the captured image as a reference for RF power adjustment is not preferable.

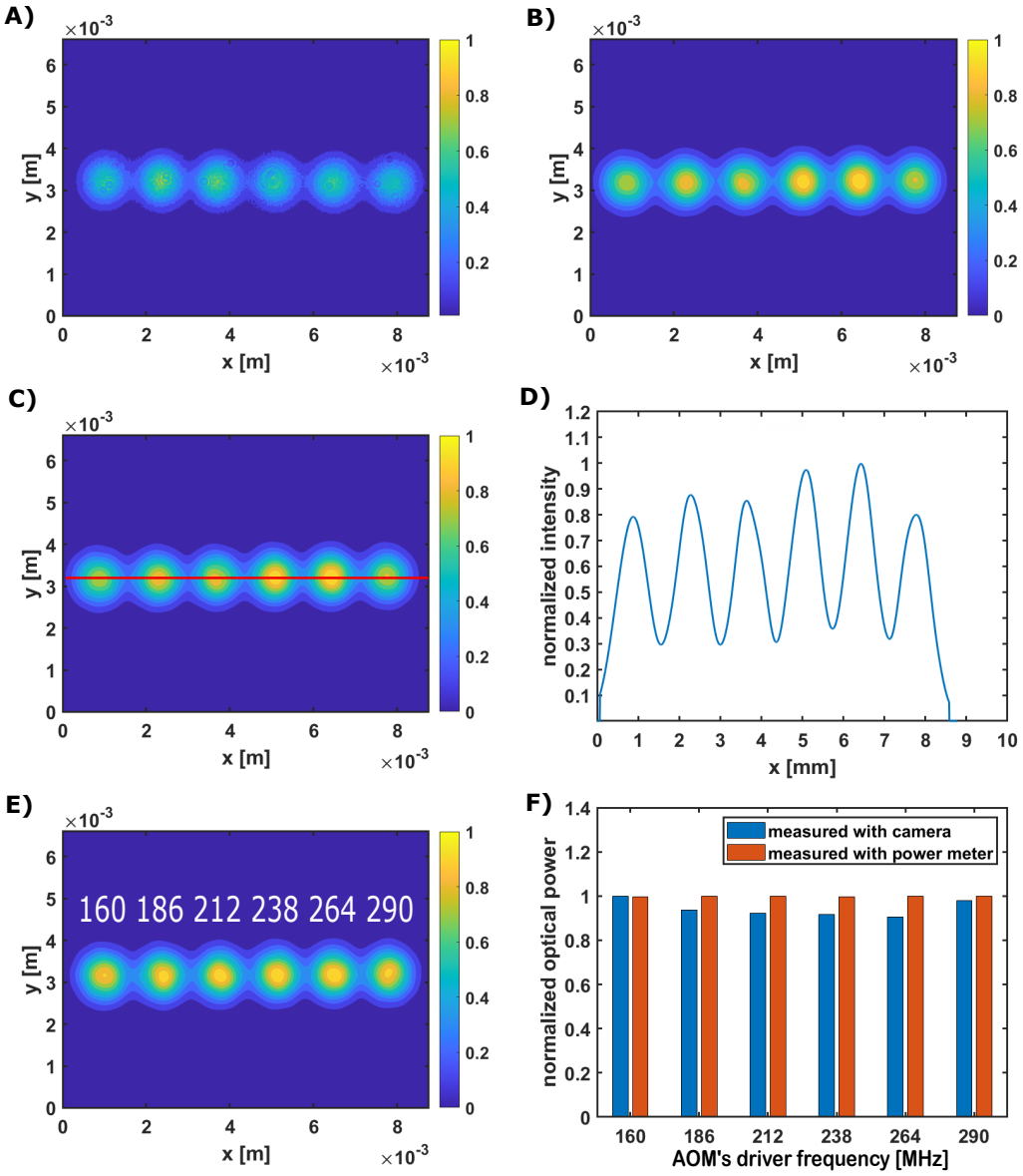

Fig. 4.25: Horizontal deflection pattern. A) Horizontal deflection pattern captured with a camera after X-AOM. The picture is taken with a long exposure time compared to the duration, the beam stays on each position. B) Horizontal deflection pattern after filtering out high spatial frequencies in the image. C) Horizontal deflection pattern with a marked plane (red line), from which the intensity profile of D) is taken from. E) Deflection pattern after adjusting the RF power of each driver frequency based on the measured deflection power with a power meter. The corresponding AOM driver frequencies are shown. F) Beam power at each position measured with a power meter compared to the peak intensity of each spot taken from image E). The color bar shows normalized intensities.

For this reason the deflected optical power is taken as reference for further RF power adjustments.

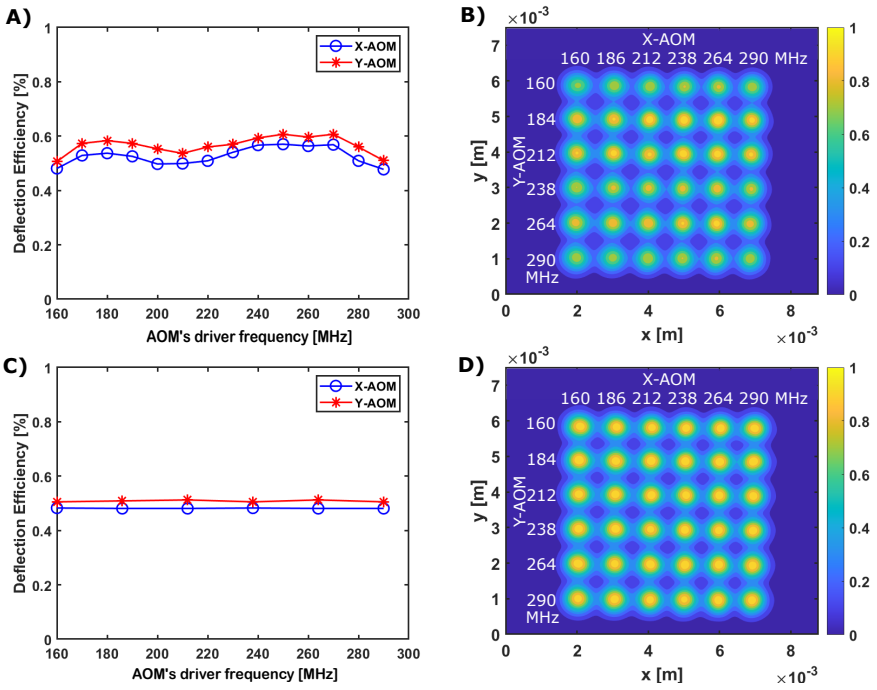

Fig. 4.26: Deflection performance of the 2D deflection system. A) DE curve for Y- and Y-AOM with the highest and flattest DE in the whole acoustic bandwidth of the AOM. B) 2D deflection scan pattern captured with a camera 15 cm after the Y-AOM with an exposure time of 836 ms. The beam is moved every 3 µs, row by row, from the top to the bottom. The corresponding driver frequencies for both AOMs are shown. The color bar shows normalized intensities. C+D) DE curve and deflection pattern after adjusting the RF power of each driver frequency based on the deflection power of each spot to obtain a flat DE curve.

In the next step the whole 2D deflection system is analyzed after optimizing the DE curve for both AOMs. Figure 4.26A) shows the measured efficiency curve for the X- and Y-AOM for a beam spot of 190 µm and a RF power of 2.7±0.4 W. The mean deflection efficiency of the X- and Y-AOM is 52.7% and 56.6%, with a standard deviation that is 6% of the mean value for both AOMs. As both AOMs were tested under the same conditions, the difference of the deflection efficiency seems to be due to differences in manufacture. A deflection pattern obtained with both AOMs is presented in figure 4.26B). The pattern is scanned row by row from left to right and stays 3 µs at each position. It is captured with a beam profile camera 15±1 cm after the Y-AOM with an exposure time of 836 ms. The scan range of both AOMs in this plot is around 4.9µm (peak to peak), which equals an angle of 32±2 mrad. This is consistent with equation 4.40 and the scan range defined by the manufacturer.
By adjusting the RF power, an even flatter DE curve can be obtained. Figure 4.26C) shows the DE of the 6 driver frequencies used for the generated deflection pattern depicted in subplot D) after adjusting the RF power.

The homogeneous power distribution for the whole scan pattern can be seen. A standard deviation of the optical power of each spot, corresponding to 1% of the mean spot power was measured. Each spot shows a well conserved transverse Gaussian beam profile. It allows the conclusion that both AOMs and the imaging configuration do not introduce important beam distortion. With the presented RF power adjustment the deflection efficiency of the X- and Y-AOM is set to 47.5% and 51% in the whole acoustic bandwidth of the AOM. The resulting deflection efficiency of the whole system equals 24.2% .

Fig. 4.27: "Virgo" written with a laser beam with a wavelength of $\lambda_L = 1064$ nm on a detector card. The beam is deflected by the 2D deflection system depicted in figure 4.21. The photo was taken with a smartphone camera.

With the presented 2D deflection system, driven by the software-defined radio, any arbitrary deflection pattern can be generated easily. Figure 4.27 shows a photo of a laser detector card when "Virgo" is written with the laser beam on it. This pattern is obtained by generating the corresponding driver frequencies of the AOMs with the USRP.

4.6.3 Deflection transition time

The time it takes to switch from one deflection direction to another gives the rapidity of the system and is experimentally measured. Two random deflection directions are chosen for this measurement. Figure 4.28(a) illustrates the experimental setup: Two fast photodiodes with a bandwidth of 200 MHz are placed behind the 2D deflection system. The laser beam is continuously deflected between two directions, staying at each deflection angle for 200 ns. The AOM driver frequencies (X-AOM,Y-AOM) are (160,160) MHz and (290,290) MHz. They belong to the spot on the top left and the bottom right in figure 4.26D). In order to synchronize the deflection of both AOMs, the beam needs to hit the crystal of the AOMs at the same distance from the transducer. This can be achieved by moving one AOM parallelly to the axis of the acoustic wave propagation in its crystal on a translation stage. In this way the shortest transition time between two randomly chosen deflection positions is obtained. Both deflected laser beams are focused on the photodiodes to capture the whole beam. Figure 4.28(b) shows the normalized signal of both photodiodes.

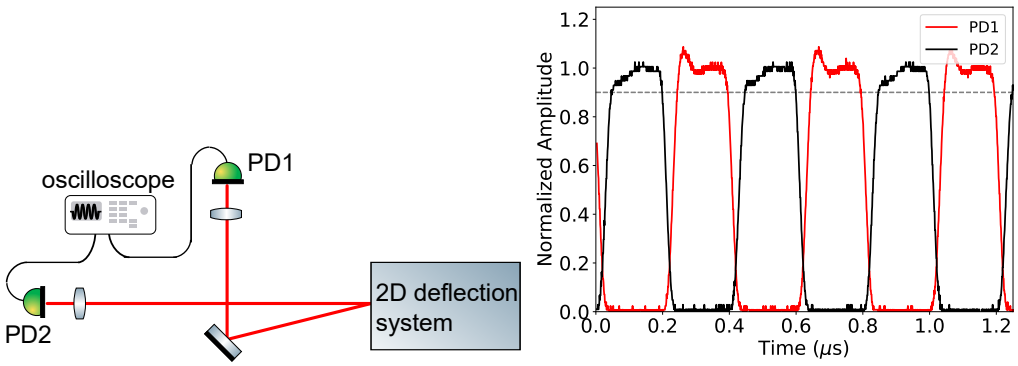

Fig. 4.28: (a) Experimental setup to measure the transition time for beam deflection in random access. Two photodiodes (PD1 and PD2) are used to detect the deflected beam on the positions corresponding to a driving frequency in both AOMs of 160 MHz (PD1) and 290 MHz (PD2). The AOM's driving frequency is switched continuously every 200 ns. A lens is used to focus the entire beam on the sensor. The AOM's input spot diameter is 190 μm. (b) Normalized signals of PD1 (red) and PD2 (black). The dashed line indicates the 90% of the stationary signal level, used to measure the transition time.

.

One can see that if the spot is on photodiode 1 (PD1), the signal of PD2 equals 0 and vice versa. The 90-90% transition time is 50±5 ns. This means that the beam stays effectively around 150 ns at the addressed position with an intensity of more than 90%. By reducing the duration of each driver frequency to 100 ns, it gives an effective dwelling time of the deflected spot of around 50 ns on a position (amplitude higher than 90% of maximum value). This is the minimum dwelling time that can be obtained without reducing the deflected beam power, thus, the applied force. Hence, the maximum deflection rate is 10 MHz. One can also see in fig. 4.28(b) that the deflected beam power takes some time to reach the final level. This time has been estimated at 44 ns, assuming an exponentially damped amplitude oscillation. This is due to the AOMs since this behavior is detector-independent and the amplitude modulation accompanying the frequency transition of the USRP signal has a shorter time constant (see fig. 4.18). An additional Pockels cell in the experimental setup could be used to cancel this amplitude modulation.

4.6.4 High optical power deflection

Not only rapid deflection but also deflection of a high power beam is necessary in order to use the laser beam as a radiation pressure source. A 50 W fiber amplifier (Azur lights, France) is used in order to determine the limits of our 2D deflection system. Fig. 4.29(a) shows the optical setup of this experiment. By using a set of

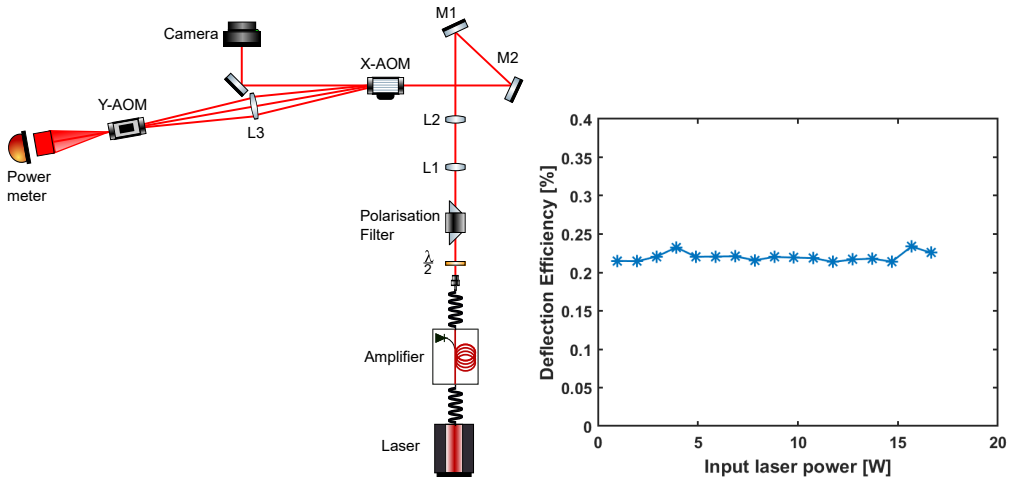

(a) (b)

Fig. 4.29: High power measurement. (a) Experimental setup for high power beam deflection. The seed laser gets amplified with a 50 W fiber amplifier. A set of a half-wave plate ($\frac{\lambda}{2}$) and a polarization filter are used to regulate the laser power. Lenses L1 (f = 750 mm) and L2 (f = 200mm) are used to focus the beam spot to 200 μm at the X-AOM. Mirrors M1 and M2 are used to adapt the beam height and angle. Lens L3 (f = 200 mm) images the spot of the X-AOM into the Y-AOM. The 0 order of the X-AOM is imaged with a camera. The final deflection power is measured with a power meter. (b) Deflection efficiency of the whole 2D beam deflection system for different optical input powers for a beam spot diameter of 200 µm.

a half-wave plate and a polarizer, the optical power is adjusted. The laser beam is focused with a set of two lenses to a waist diameter of 200 µm in the X-AOM, and the optical laser power is increased step by step. As the maximal optical power density of the AOM given by the manufacturer is 500 $\frac{\mathrm{W}}{\mathrm{mm}^2}$, the maximal laser input power is 15.7 W for this beam waist. A camera is used to monitor the transmission beam shape of the X-AOM. For the deflection efficiency measurement, the AOM input power is measured between L1 and L2 and the power of the deflected beam of Y-AOM. The insertion losses of the optical components in between were determined and taken into account. Fig. 4.29(b) shows the deflection efficiency of the whole 2D deflection system for different optical input power. With an increased laser input power of 16.7 W no decrease in deflection efficiency has been detected. However, a thermal lens has been observed with a spot size variation of 8%. This measurement shows a flat deflection efficiency of 22% for input powers up to 16.7 W for this 2D deflection system. The maximal deflected beam power was 3.6 W. The fact that the efficiency is 2% lower than the value measured in section 4.6.2 can be due to laser power fluctuations and the fact that two different power meters were used with a nominal accuracy of $\pm 5\%$ defined by the manufacturer in this power range.

4.6.5 Conclusion

We demonstrated a rapid 2D beam deflection system that has all the characteristics required for active PI mitigation in GW detectors.
The fast deflection is based on AOMs that combine the large deflection range of an acousto-optic deflector with the rapidity of an acousto-optic modulator. The measured transition time between two random steering directions is 50±5 ns, independent from the angle between both directions. This allows a deflection rate of up to 10 MHz, which will be necessary to damp mechanical modes with hundreds of kHz.
The random access deflection is ensured by a software defined radio device (USRP) that is used as fast AOM driver. The fact that the beam can be deflected in random access enables the implementation of an optimal deflection pattern to damp any mechanical mode shape.
A deflection for a maximal beam power of 3.6 W is demonstrated, which is equal to a radiation pressure force of 24 nN. A first estimation done in chapter 3.2 shows that this force is sufficient to damp rising unstable mechanical modes, if they are detected early. These performances were obtained for a laser with a wavelength of 1064 nm and a spot diameter of 190 μm in the AOMs. By decreasing the spot diameter in the AOM, even faster transition times could be achieved with the cost of lower maximal power in the deflected beam, due to the power density limits of the AOM crystal. In this way the available radiation pressure force for PI mitigation would be decreased. In addition, a further focused beam will have a larger divergence which means that the deflected beam hits the cavity mirrors with a larger spot diameter.
As mentioned in the previous chapter, in order to address mechanical mode shapes with small lobes, a small laser spot is desirable to obtain a large overlap. The important quantity that has to be small is the ratio of the beam divergence to the scan angle. We reached stable deflection performances over the AOM's whole scan angle of 32 ± 2 mrad, whereas the beam divergence results from the choice of the optimal spot diameter in the AOM, which is a compromise between the rapidity and the maximal available radiation pressure force. The obtained ratio is 1/5, which means that the spot diameter on the target mirror surface is one sixth of the beam diameter.

Another task that needs to be investigated for PI mitigation based on radiation pressure is the PI detection. Our 2D deflection system could also be used for this purpose, by scanning the whole mirror and measuring its displacement by interfering the reflected beam with a reference beam. This approach will be discussed in the next chapter.

5 Mechanical Mode Sensing

5.1 Introduction

In order to mitigate parametric instabilities via radiation pressure of a movable laser beam, it is crucial to sense arising parametric instabilities. To keep the necessary laser power low, PI should be detected as early as possible as discussed in chapter 3.2.
One way to detect PI consists in measuring the unstable mechanical eigenmode involved in PI. Characteristic quantities of mechanical eigenmodes are their frequency, their quality factor and their geometric shape.
The quality factor of mirror mechanical eigenmodes in GW detectors has been determined by measuring the time constant τ_m (see eq. 2.4) of the exponential ringdown after these modes were excited. The eigenmodes were excited by the ESD in LIGO [56].
In LIGO the geometric mode shape of mechanical eigenmodes could be confirmed by the beat note of the fundamental and higher-order optical mode involved in PI, measured with quadrant photo detectors in transmission of both interferometer arms [4, 57]. The phase shift between the measured beat signal with each quadrant contains information about the mode shape of the optical higher-order mode that is involved in PI. By comparing the mode shape of simulated eigenmodes of the test mass with the phase information obtained by the quadrant photo detectors, the mechanical mode is obtained.
Direct measurements of mirror surface displacements due to thermally excited mirror modes has been demonstrated for mm-scale mirrors [130] and µ-scale mirrors [131] in a cavity. These measurements were done with frequency- and intensity-stabilized lasers with a high sensitivity corresponding to an observable displacement at the level of $10^{-19}\frac{\mathrm{m}}{\sqrt{\mathrm{Hz}}}$. A thermally excited acoustic mode in a 5.6 kg sapphire mirror has been measured with a displacement sensitivity of around $10^{-17}\frac{\mathrm{m}}{\sqrt{\mathrm{Hz}}}$ in the 77 m high optical power cavity of the Gingin Test Facility [52].

The experiment work presented in this chapter aims at sensing excited eigenmodes of a test mirror via a Michelson interferometer. The 2D deflection system presented in the previous chapter is used to change the beam position in the interferometer. The geometric shape of the mechanical mode can be reconstructed by analyzing the interference signal of the beam scanning the mirror surface. In section 5.2 the

experimental setup is presented. The alignment of the interferometer is explained in section 5.3. Subsequently, the results after adjusting the interferometer are presented in section 5.4. A servo loop was used in order to lock the inteferometer. The principle of the servo loop is discussed in section 5.5 and first results are presented. In section 5.6 the possibility to detect thermally excited modes with the presented system is discussed. It includes simulation of the test mirror modes, estimations of limiting noise sources and the measured amplitude spectral density of the interference signal of the implemented interferometer. A final conclusion and propositions to improve the current experiment are presented in section 5.7.

5.2 Experimental layout

An optical setup for mechanical eigenmode sensing, amplification and attenuation by using the 2D deflection system presented in the previous chapter is depicted in figure 5.1. The mode detection is based on a Michelson interferometer. By modulating the laser power and adjusting the phase of the laser beam the same setup could be used to control mechanical eigenmodes of the mirror by amplifying or attenuating them. The laser beam is deflected in two dimensions and the height of the beams is lifted with a periscope in order to point at the center of the test mirror with the central beam. Since the reflectivity and transmission of the beam splitter and polarizer depend on the incident beam angle, the diverging deflected beams after the 2D deflection system are collimated with lens L2. In this way each deflected beam is transmitted and reflected in the same proportions. We used optical components that were available in the laboratory to set up this experiment. Since many optical components with a diameter of one inch were available, as for example the mirror mounted on the piezo, the $\frac{\lambda}{4}$- and $\frac{\lambda}{2}$- wave plates, L2 was chosen in a way to let the entirety of deflected beams cross each optic without any clipping. By putting L2 with a focal length of $f_2 = 300$ mm in a distance of f from the center of the Y-AOM, all possible deflected beams in two dimensions describe a square with a side length of about 1 cm for a scan range of 34 mrad of both AOMs.
A set consisting of a polarizer and a $\frac{\lambda}{4}$- wave plate is used as an isolator. The polarization of the back reflected light from both mirrors in the Michelson-Inteferometer is shifted by 90 degrees with respect to the incoming light which is subsequently reflected at the polarizer (P1). A $\frac{\lambda}{2}$- wave plate is used to turn the polarization of the deflected beams to adapt the polarization of the polarizer for maximal transmission of the incoming beam. By putting a mirror behind the $\frac{\lambda}{4}$- wave plate and tilting the mirror to be capable to measure the back reflection of the isolator, an isolation of >30 dB has been measured.
The Michelson interferometer has a one-inch diameter mirror at the end of the reference arm mounted on a piezo stack and a two-inch diameter test mirror at the

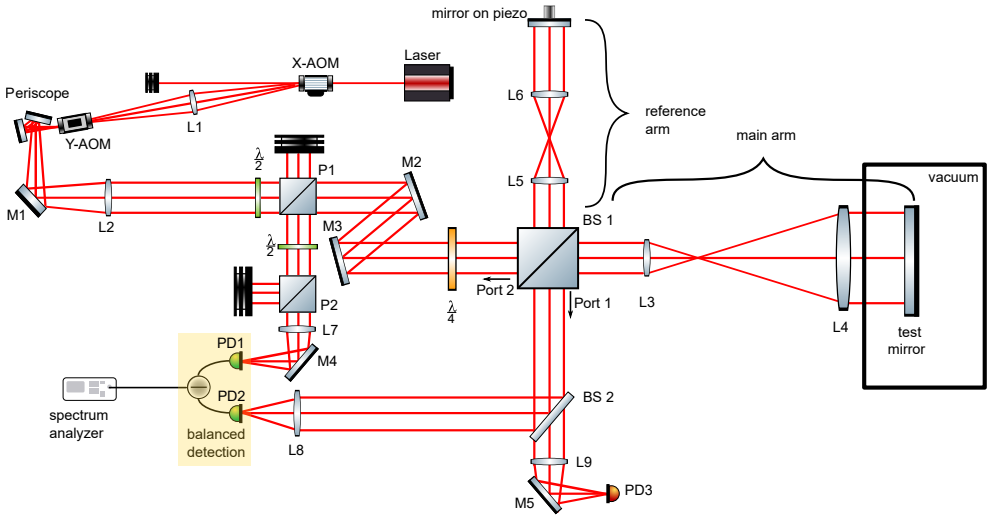

Fig. 5.1: Optical setup for mechanical mode sensing by interferometry. The 2D deflection system presented in chapter 4.6 is used to deflect the laser beam in two dimensions with the X- and Y-AOM. A periscope is used to raise the beam height without turning the deflection direction of each beam. Lens 2 collimates the ensemble of all spots, and the $\frac{\lambda}{2}$- wave plate turns the polarisation, so that the beams are transmitted by the polarizer P1. A set consisting of a polarizer (P1) and a $\frac{\lambda}{4}$- wave plate is used as isolator for the incoming beams. With a 50/50 beam splitter (BS) the beams are split into two arms. A telescope L3 + L4 is used in the main arm to enlarge the beams to be able to point at any position on the test mirror. The test mirror is placed in a vacuum chamber. A unity magnification telescope L5 + L6 is used in the reference arm to adjust the phase of the beams to fit the phase of the beams in the main arm. The end mirror of the reference arm is mounted on a piezo and driven by a servo-system to keep the interference signal on half fringe. The interference signals leaving the interferometer at port 1 and 2 are captured in balanced detection with two photodiodes. For this reason the optical power of the interference signal leaving at port 2 is adjusted with a set of a $\frac{\lambda}{2}$- wave plate and a polarizer P2. The difference between the photo currents of photodiode PD1 and PD2 is analyzed with a spectrum analyzer. The interference signal at port 1 is captured additionally with a photodiode (PD 3).

end of the other arm. The mirror mounted on the piezo stack is home-made (see figure 5.2A). A telescope with two-inch mirrors L3 and L4 is used to enlarge the beams in order to cover as much as possible of the surface of the end mirror. Since the lenses of the telescope L3 + L4 introduce a phase shift to the beams depending on their distance to the central beam, an additional telescope L5 + L6 with unity magnification is installed in the reference arm. The telescope L5 + L6 is used to adapt the phase of the beams in the reference arm in order to attain an interference signal with a similar phase for as many deflected beams as possible.
In order to increase the signal-to-noise ratio (SNR) of the measured interference signal, it is captured in balanced detection [132], the interference signal of port one of the Michelson interferometer being focused with lens L8 into photodiode PD2. The exiting beam from port 2 is reflected by the polarizer P1. With an ensemble of a $\frac{\lambda}{2}$- wave plate and a second polarizer P2 its intensity can be adjusted. This beam is focused with lens L7 into photodiode PD1. For balanced detection the intensity of the beams on both photodiodes is set equal. The photo current of both photodiodes is subtracted in a circuit and a voltage proportional to this difference is retrieved. The voltage is analyzed with a spectrum analyzer. Since the interference signals of both ports of a Michelson interferometer have different signs (see chapter 1.2.1), it is not suppressed by the balanced detection, but can be measured with the spectrum analyzer.
With such a detection scheme the laser intensity noise and other noise sources affecting the beam in both interferometer arms equally are suppressed. Figure 5.2B) shows the test mirror with a diameter of 2 inches and a thickness of 0.5 inches. It is a fused silica mirror with super-polished front and back sides (from Advanced Thin Films). The quality factor of mechanical eigenmodes of this mirror are estimated to be at the order of 10^6 based on [133]. The mirror is held at three distinct contact points in the middle of its depth. This mirror mount is intended to allow mechanical oscillations of the mirror with a minimized dissipation while avoiding mirror suspension. The mirror is mounted in a vacuum chamber in order to prevent thermal modes being damped through viscous friction with the ambient air. A vacuum of the order of 10^-6 mbar was achieved. During the measurements the vacuum pump is switched off.

5.3 Alignment procedure

In order to align the interferometer, all optical components between mirror M1 and the test mirror are removed except for all mirrors. The test mirror is in a mount that is not easily adjustable, as one can see in figure 5.2B). For this reason it is installed first. The periscope and mirror M1 are adjusted in a way that the central deflected spot (with the carrier frequency of both AOMs as driver frequency) points at the

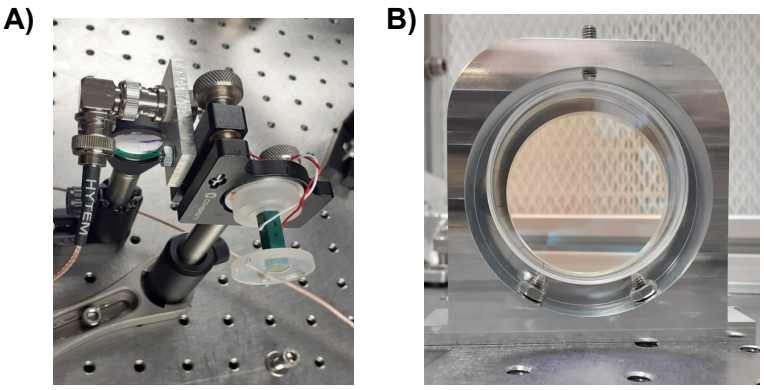

Fig. 5.2: Photos of optical components used. A) Self-constructed mirror mounted on a piezo stack. B) Test mirror with high mechanical mode quality factors.

center of the test mirror. The horizontal orientation of the mirror is roughly adjusted so that the back reflected beam is collinear with the incident beam. A detector card is used to verify the position of both beams by holding it into the infrared beam. Mirror M2 and M3 are installed in a way that the beam is also reflected at their center. The collimation lens L2 is mounted on a translation stage to easily adjust its position, so that the beam is well collimated. A camera is used to measure the beam waist at different distances from L2 to verify that the beam waist stays constant.
In the next step the $\frac{\lambda}{2}$- and $\frac{\lambda}{4}$- wave plates with the polarizer P1 are set in place. The scan pattern with 36 spots, as depicted in figure 4.26 in chapter 4.6, is emitted with the 2D deflection system. A camera is put behind the $\frac{\lambda}{4}$- wave plate and the positions of all optical components are adjusted if necessary so that all 36 spots can be seen without any clipping.
Then the beam splitter is installed and adjusted, so that the incident central deflected beam and exiting beam at port 2 are collinear. in the next step the reference mirror is installed and adjusted so that both reflected beams exiting port 1 are collinear. For this procedure a camera is installed at port 1 and the reference mirror is adjusted.
In the next step the scan pattern with 36 beam directions is emitted with the 2D deflection system. The position of the reference mirror is modulated with a low frequency by applying a modulated voltage to the piezo. An interference pattern is observed with the camera at port 1. In order to observe constructive and destructive interference of all 36 spots with the camera at the same time (the camera has a long exposure time compared to the scan frequency of the beam), the interferometer still needs to be adjusted. The horizontal adjustment is done with the reference mirror and vertical adjustment is done with mirror M2 and M3. When all 36 spots on the camera appear and disappear simultaneously (constructive and destructive interference) all deflected beams are in phase.
In the last step both telesopes are installed: first the camera is put between the beam splitter and the test mirror. The position of the central deflected beam is marked on the camera. Then the deflection pattern with 36 spots is emitted and L3 is fixed with a distance of its focal length before the camera. L3 is adjusted so that the focal point

of the deflection pattern overlaps with the marked position of the central deflected beam on the camera. The camera is then fixed in port 1 and L4 is fixed at a distance equal to the sum of the focal length of L3 + L4 behind L3 on a translation stage. The position of L4 is adjusted, so that as many beams as possible are in phase. The same procedure is done for the telescope in the reference arm.

5.4 Results of interferometer alignment

A critical point in this setup is the telescope L3+L4. It is necessary to enlarge the beams in order to cover the whole mirror surface. The collimated beams of the deflection pattern with 36 deflection directions after L2 describe a square with a side length of around 1 cm. In order to cover the test mirror with all deflected beams they need to be magnified. Figure 5.3 shows two possible magnifications of a deflection pattern of 36 beam spots on a mirror. The distance of consecutive spots equals the diameter of a spot at $\frac{1}{e^2}$ of its intensity. In configuration A) all 36 spots are on the mirror but only 64 % of the mirror's surface is covered. In configuration B) the whole surface of the mirror can be attained by the laser beam but 21 % of the scan pattern is clipped by the mirror. We chose a magnification of 4 for the telescope

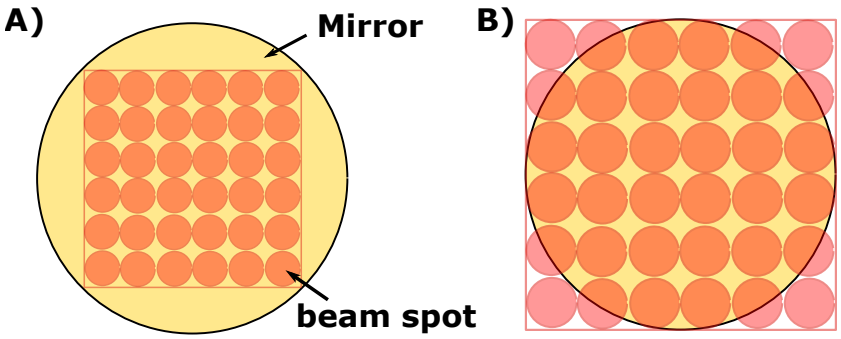

Fig. 5.3: Schematic of two possible magnifications of a beam pattern on the test mirror. A pattern of 36 beam positions (orange circles) with a distance of the $\frac{1}{e^2}$-spot diameter shown on the test mirror (yellow circle). A) A magnification so that all deflected beams are on the mirror. B) A magnification so that the whole mirror surface is covered by the deflected beams with the lost of beam positions which are clipped by the mirror.

in order to cover the total mirror surface with the deflection pattern.This means that f_4 should equal to $f_4 = 4f_3$ with f_3 and f_4 the focal length of L3 and L4. And both lenses should have a distance of $f3 + f_4$.
At first we chose lenses with small focal lengths to keep the interferometer small and compact. But lenses with spherical surfaces with small focal lengths are more sensitive to spherical aberrations since the curvature of these lenses is higher. Different configurations were tested to minimize spherical aberrations:

1- Lenses with larger focal lengths were tested. The telescope with the largest available focal lengths in the lab were a lens L3 and L4 with focal lengths $f_3 = 100$ mm and $f_4 = 400$ mm, respectively.
2- The ratio of the magnification of the telescope and the beam size after collimation is changed. Instead of L2 with $f_2 = 300$ mm a lens with $f_2 = 400$ mm was used as collimation lens. In this way the beam diameter after collimation was larger so that a telecope with a smaller magnification was used with $f_3 = 150$ mm and $f_4 = 400$ mm. But in this configuration some beams of the deflection pattern with 36 spots were clipped at the optical components between L2 and the beam splitter.
3- An aspherical lens was purchased and tested. Since only aspherical lenses with a focal length of $f = 100$ mm were available from the manufacturers, a telescope with L3 as aspherical lens with $f_3 = 100$ mm and L4 as spherical lens with $f_4 = 400$ mm was tested.

For the measurements reported in the following, a telescope described under option 3 was used. An additional telescope with unity magnification was implemented in the reference arm in order to compensate the phase shift between the 36 deflected beams, introduced by the lenses of telescope L3+L4.

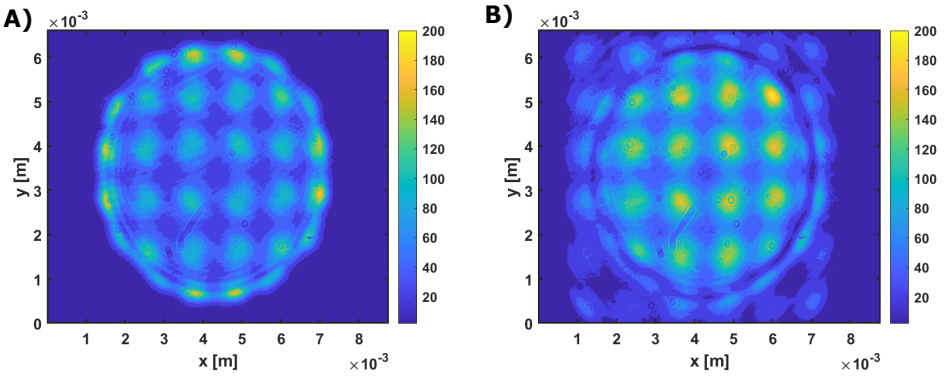

Fig. 5.4: Deflection pattern of 36 deflection directions (see figure 4.26 in chapter 4.6) created with the 2D deflection system and captured with a camera at port 1 of the interferometer depicted in figure 5.1 A) when the beams in the reference arm are blocked. B) when the beams of both interferometer arms interfere. (The color bar defining the intensity has arbitrary units.)

Figure 5.4A) depicts the deflection pattern of 36 spots obtained with the 2D deflection system (see figure 4.26) at port 1 of the interferometer, when the beams in the reference arm are blocked. For this measurement a camera is put at the place of PD2 in the setup with a smaller distance as f_8 from L8 in order to capture all spots. It shows basically all deflected beams that are reflected off the two-inch-diameter test mirror and are transmitted by the telescope L3+L4. One can see that the beams at the edge are already clipped, introducing interference fringes at the edge of the pattern due to diffraction. Lens L4 and the test mirror clip the magnified pattern of the 36 deflected beams. With the implemented telescope 6 spots are already

visible on the horizontal and vertical axis of the pattern, while the ones at the edges are deformed by the diffraction ring. One can see that with the telescope L3+L4, with magnification 4, the whole surface of the test mirror is covered by the deflected beams, with the cost of clipped beams. A configuration with a little larger magnification than depicted in figure 5.3B) is achieved.
The interference pattern of the 36 beams measured with the camera is illustrated in figure 5.4 B). Only 16 of the 36 beams seem to interfere with a similar phase since their intensity is quite similar. A circle with low intensity surrounds these 16 spots on the image, whereby the four spots in each corner are also partly affected. It seems to be due to the clipping of the beams in the main arm. The remaining 20 spots which are back reflected by the reference mirror can also be seen but with lower intensity, outside the circle.

A study of the 12 beams in the center of the deflection pattern shown in figure 5.4 is depicted in figure 5.5. After a preliminary measurement we figured out that the four beams in the corner of the 16 spots already have an important phase shift, so these beams were not included in the study. Assuming that the circle defining the deflection pattern shown in 5.4A) defines the edge of the test mirror one can say that these 12 spots cover approximately a circle with a radius of $\frac{2}{3}$ of the mirror radius. It results in 44 % of the mirror surface. The subplot A) shows a scan of the 12 spots captured with the camera for constructive interference. Well-conserved Gaussian beam profiles can be seen for these spots. It allows the conclusion that these beams are not clipped or diffracted by any component in the interferometer. In order to determine the phase between the interference signals of each beam the piezo of the reference mirror has been driven with a slow linear increasing tension (duration > 1 s) from 0.5 to 8.5 V. In the same time the laser has constantly scanned this pattern by switching the position each 100 μs. Photodiode PD3 has been used to capture the interference signal. With an oscilloscope 37 measurements of the interference signal of the 12 spots has been captured. Figure 5.4B) shows one measured interference signal with the photodiode. One can see 12 different voltage levels with 0.1 ms duration which repeat after time 1.3 ms. The measured tension is proportional to the interference signal and varies between 0 for destructive interference and about 1.7 V for constructive interference. As the laser beam is scanned so fast compared to the slow linear ramp driving the piezo, the tension at the piezo for each measurement can be considered as constant. This can also be seen in subplot B) where the interference signal of the 12 beams is measured twice within several ms and the voltage of corresponding interference signals stays constant. By retrieving the amplitudes of the interference signal for each spot from the 37 measurements and plotting them versus the piezo driver tension the plots in figure 5.5C) have been obtained.
The measured data is shown as blue dots and a fitted curve with the form of

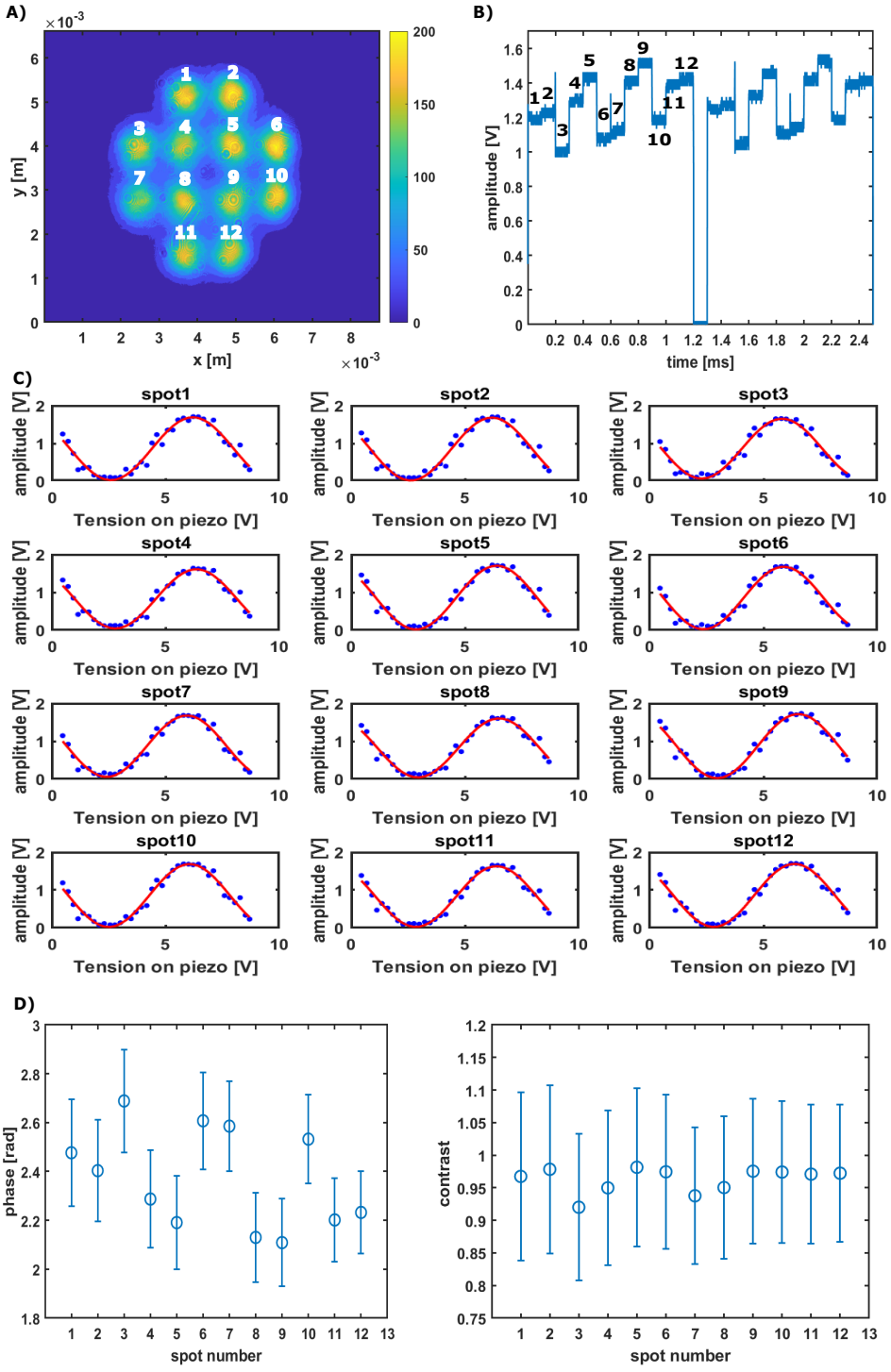

Fig. 5.5: Interference signal of the 12 spots in the center of figure 5.4.A) Photo of constructive interference measured with the camera at port 1 of the inteferometer (The color bar defining the intensity has arbitrary units). B) Interference signals measured with a photodiode PD3 at port 1. The beam stays at each position for 100 µs. C) Interference signal versus driver tension of the piezo of the reference mirror with data (blue dots) and a fit (red line) with a function $y(x) = a\cos(\frac{2\pi x}{p} + \phi) + c$ D) fitted phase for each spot E) fitted contrast for each spot.

$y(x) = a\cos(\frac{2\pi x}{p} + \phi) + c$ is shown in red. x describes the tension applied on the piezo, a the amplitude of the interference signal, p the period of the interference signal, ϕ the phase and c the offset. The mean value for the fitted period for all spots equals 7.1V. That means that by applying a difference of 7.1 V to the piezo the mirror is displaced by 532 nm since the laser wavelength is λ_L=1064 nm.
Subplot D) and E) show the obtained fit parameters for the phase ϕ and the contrast for each spot with the corresponding errors of the parameters for a 95 % confidence level of the fit. A contrast of more than 90 % for all 12 spots has been measured with a maximal phase difference between the interference signal of the spot 3 and 7 of $0.2\pi \pm 0.1\pi$.

For the mechanical mode detection the interferometer is locked on half fringe of the interference signal. It corresponds to the offset parameter of the fit with $c = 0.82$ V. When the beam is deflected between these 12 positions on the mirror the interference signal has a maximal phase shift of 0.2π. This means that it is still in the linear region of the sinusoidal interference signal. Thus, the servo system will still be able to keep the interferometer locked at the same set point.

5.5 Locking of the interferometer

In order to be sensitive to small arm length differences in the interferometer, different noise sources need to be suppressed. In the laboratory, for instance, there are acoustic noise sources like different chillers and instruments but also air fluctuations due to ventilation systems. These sources disturb the optical arm length of both interferometer arms which results in fluctuations in the measured interference signal. One opportunity to overcome such noise in the interference signal consists in locking the interferometer. For this purpose the reference mirror is mounted on a piezo to easily adapt the reference arm length so that the interference signal stays stable in time. This allows the acquisition of data by averaging over several seconds.
Figure 5.6 depicts a simplified schematic of the interferometer presented in figure 5.1 with a servo loop to lock the interferometer. The laser beam is deflected in two dimensions with the 2D deflection system. These deflected beams enter the Michelson interferometer. At the end of the main arm is the test mirror and at the end of the reference arm is the reference mirror mounted on a piezo stack. By applying an electrical tension on the piezo stack the position of the reference mirror can be changed (Δx). In the output port 1 of the interferometer there is a lens which focuses the entire beams into a photodiode. In order to lock the interferometer the position of the reference mirror needs to be controlled. This can be done by setting up a servo loop:
The interference signal obtained by changing the arm length of a Michelson- Interfer-

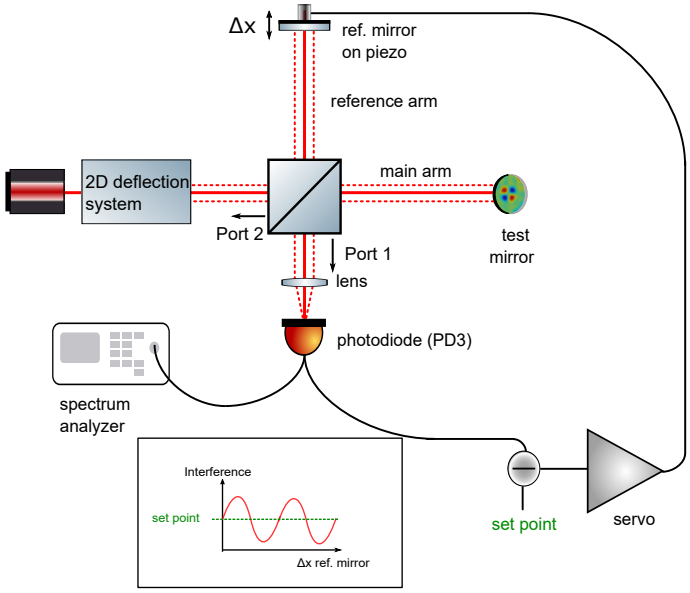

Fig. 5.6: Conceptional schematic of Michelson interferometer used to sense mechanical eigenmodes of a test mirror locked with a servo system. The laser beam is deflected in two dimensions before entering the interferometer. At the end of one arm is the mirror test mass which is investigated and at the other arm is a reference mirror mounted on a piezo stack. The interference signal of all deflected beams is focused into a photodiode. A servo loop is used to lock the interferometer to half fringe signal by controlling the reference mirror position. The frequencies and amplitudes of the mechanical modes on the test mirror are observed on the spectrum analyzer. Inset: the set point used is the offset of the sinusoidal interference signal.

ometer is described in Chapter 1.2.1. The measured tension at an output port of the Michelson interferometer can be described by a sinus function when Δx is changed by several laser wavelengths (see inlay of figure 5.6). The set point of the control loop is set to the half fringe voltage of the interference signal. Since the slope of the sinusoidal interference signal at half fringe is the highest, the interferometer is consequently also the most sensitive to local displacements of the test mirror. An error signal is produced by taking the difference of the set point tension and the actual captured photodiode tension. The servo system uses this error signal to correct the reference mirror position. The implemented servo is a simple integrator with an adjustable gain.

In the first step the transfer function of the ensemble of reference mirror with piezo stack (see figure 5.2A) is measured. For this measurement an offset tension is applied to the piezo so that the interference signal is about the set point. In this way a linear response of the photodiode signal is obtained. Subsequently a frequency sweep with a constant amplitude of 1 V is applied to the piezo and the interference signal is captured with a photodiode in port 1 of the interferometer. The transfer function is the measured interference signal divided by the applied signal to the piezo. Figure 5.7 shows the measured transfer function. One can see some resonances of the piezo stack with mirror for instance at 220 Hz, 2.3 kHz and 4.4 kHz.

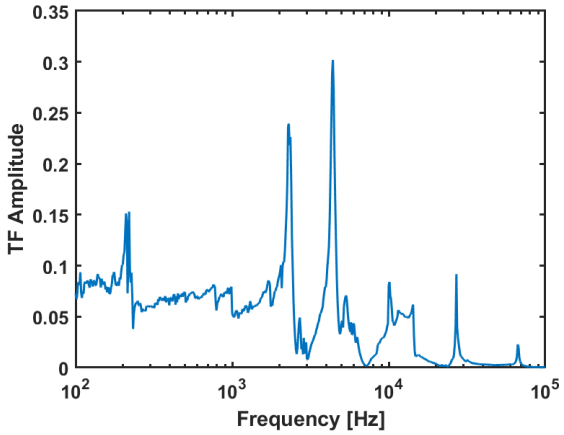

Fig. 5.7: Transfer function of the ensemble of piezo stack and reference mirror (see figure 5.2A) in the interferometer depicted in figure 5.6.

A servo system was implemented with this mirror. The measured bandwidth of the servo system was smaller than 30 Hz. This means that noise sources up to 30 Hz were suppressed with this servo loop. In order to enlarge the bandwidth two notches were built for the 220 Hz and 2.3 kHz resonance. They were added in the servo circuit, so that the servo system did not become unstable. In this way the bandwidth of the servo loop was enlarged to around 800 Hz.
This bandwidth could not be kept for long since the resonance peak of 220 Hz was drifting in time. The final bandwidth of the servo loop was less than 30 Hz.
In order to improve the servo loop it would be of interest to design a new piezo-mirror setup with fewer resonances and at higher frequencies.

5.6 Detection of the mirror's eigenmodes

5.6.1 Simulation

A finite element simulation of free vibrational modes of the test mirror was done with Ansys by my colleague Mourad Merzougui. In this way the range of eigenmodes frequencies for this test mirror could be estimated. Since the mirror was not freely suspended but fixed with three screws as shown in figure 5.2B the simulation gives an approximation. Table 5.1 shows a list of the first free vibrational modes for a silica cylinder with a diameter of 2 inches (50.8 mm) and a thickness of 0.5 inches (12.7 mm). Figure 5.8 shows the simulated mirror with its first vibrational mode with a drumhead mode shape at 35.6 kHz. The geometrical mode shape can be seen with the maximal displacement of the surface in red and the minimal displacement in blue.

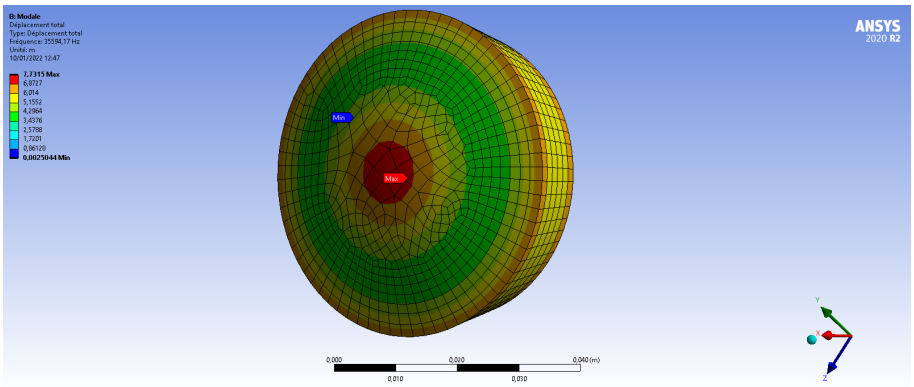

Fig. 5.8: Ansys simulation of test mirror for the first drumhead eigenmode of 35.594 kHz.

Tab. 5.1: First free eigenmodes for a silica cylinder with a diameter of 2 inches (50.8mm) with a thickness of 12.7 mm. Simulation is done with Ansys.

mode	Frequency [kHz]
1	24.651
2	24.658
3	35.594
4	48.840
5	48.845
6	54.201
7	54.205
8	60.928
9	60.947
10	66.665
11	66.722
12	70.301
13	74.220
14	74.232

5.6.2 Estimation of noise limiting the detection

An estimation of the mirror surface displacement due to thermal excitation in our experiment is done based on [134]. The amplitude spectral density a_t of the displacement at an angular eigenfrequency ω_m of the mirror equals

$$a_t(\omega_m) = \sqrt{\frac{4k_BTQ}{\omega_m^3\mu}} \tag{5.1}$$

with the Boltzmann constant k_B, the temperature T, the quality factor Q of the mechanical mode at ω_m and the mass μ of the mirror that contributes to the mode. For $\omega_m = 2\pi \cdot 35$ kHz, $T = 293$ K, $Q = 10^6$ and $\mu = 0.1$ kg we obtain:

$$a_t \approx 4 \cdot 10^{-15} \frac{m}{\sqrt{Hz}} \tag{5.2}$$

An approximation for relevant noise sources in the measurement is presented in the following. It is done for an optical power $P = 1$ mW on the photodiodes, a quantum coefficient $\eta = 0.25$ for silica photodiodes (Thorlabs FDS100) and an impedance of $R = 10\ k\Omega$ for the photodiodes. A peak-to-peak voltage of 5.5 V is assumed for the interference signal corresponding to a quarter of the laser wavelength $\frac{\lambda_L}{4} = 266$ nm. With this relation the voltage fluctuations δU can be converted into an differential arm length fluctuation δL.

- **shot noise**: For the two photodiodes the obtained shot noise expressed as ASD of the measured tension U equals:

$$\delta U = R\eta\sqrt{\frac{2Phc}{\lambda_L}} \approx 50\frac{nV}{\sqrt{Hz}} \tag{5.3}$$

  with the Planck constant h, the speed of light c. This corresponds to a displacement noise δL in the interferometer

$$\delta L \approx 2 \cdot 10^{-15} \frac{m}{\sqrt{Hz}} \tag{5.4}$$

- **electronic noise**: The estimated noise due to the electronics in the photodiode can be described as measured voltage fluctuation δU

$$\delta U = \sqrt{4k_BTR} \approx 13\frac{nV}{\sqrt{Hz}} \tag{5.5}$$

  This corresponds to a displacement noise δL in the interferometer arms of

$$\delta L \approx 6 \cdot 10^{-16} \frac{m}{\sqrt{Hz}} \tag{5.6}$$

- **seismic noise**: The arm length difference δL introduced due to seismic noise can be estimated as

$$\delta L = \frac{10^{-7}}{f^2} \approx 10^{-16} \frac{m}{\sqrt{Hz}} \tag{5.7}$$

  f is the frequency of the noise.

One can expect that the differential arm length due to thermal excitation of eigenmodes of the test mirror is around the noise level of the photo detector. It could be that shot noise limits this measurement. Consequently, it would be important to measure with a higher optical power. In order to detect the eigenmodes of the mirror we will have to excite them.

5.6.3 Measurements

We investigated the possible detection of the eigenmodes listed in Table 5.1 with a drum mode-shape. First measurements were done with the Michelson interferometer depicted in figure 5.1. The beam number 4 in figure 5.5 was deflected and the interferometer was locked with the servo system with a bandwidth of less than 30 Hz. The interference signal was captured in balanced detection and analyzed with a Network Signal Analyzer (SR 780 from Stanford Research Systems) with a bandwidth of 102 kHz.

A measurement of the amplitude spectrum density (ASD) of the interference signal is depicted in figure 5.9. Each curve consists of two measurements taken from 10 to 60 kHz and from 50 to 102 kHz. By measuring in a smaller frequency span a higher spectral resolution is obtained. The ASD of the interference signal is compared to a dark noise measurement, when both photodiodes are covered and to a measurement, when the beam in one arm is blocked. Subplot A) shows the ASD of the interference signal between 10 and 100 kHz compared with the measured dark noise. The level of the dark noise corresponds to the estimated electronic noise within a factor 3. One can see that the measurement floor of the ASD of the interference signal attains 10^{-6} $\frac{\mathrm{V_{rms}}}{\sqrt{\mathrm{Hz}}}$. The peak-to-peak voltage of the interference signal for this measurement was 5.5 V. Thus, the amplitude of 10^{-6} $\frac{\mathrm{V_{rms}}}{\sqrt{\mathrm{Hz}}}$ corresponds to a differential arm length of $\delta L = 4.8 \cdot 10^{-14} \frac{\mathrm{m}}{\sqrt{\mathrm{Hz}}}$. It is around one order of magnitude higher than the expected displacement of the mirror surface due to thermally excited mirror modes. Several peaks can be seen in the interference signal which are not present in the dark noise measurement like the one at 16, 32 and 48 kHz. There are also peaks in the spectrum which are also apparent in the dark noise spectrum like the peak at 20, 40 and the double peak at 96 and 97 kHz. These peaks could also be due to glitches in the spectrum analyzer or to electromagnetic noise in the environment.
The peak at 49 kHz is noticeable since it has been measured in the noise spectrum

but it has not been measured in the interference spectrum even if its amplitude was measured large enough. Consequently, it seems to be a glitch. In figure 5.9B)

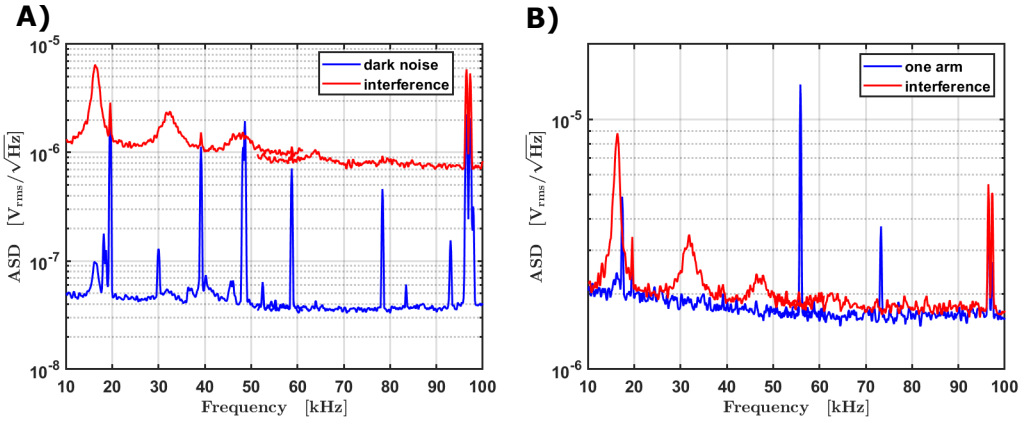

Fig. 5.9: Sensitivity curve of interferometer depicted in figure 5.1 with an average of 100. A) For dark noise and interference measurement (on 50 Ω load). B) For laser beam only in one interferometer arm compared with interference signal.

the sensitivity curve of the interferometer is compared to the measured spectrum when the beam is blocked in one interferometer arm. One can see the peaks at 16, 32 and 48 kHz again in the interference signal. These peaks appear only in the interference signal and therefore come from one of the interferometer arms. Their amplitudes are too high to be the eigenmodes of the test mirror. They are also to large to fit the expected high Q-factor of the test mirror modes. It is also possible that this measurement has not be done in perfect balanced detection so that the origin of these peaks could be due to the RIN of the laser source. There are also peaks apparent in the measured spectrum when the beam in one arm is blocked like the one at 17, 56 and 73 kHz. These peaks are not present in the interference spectrum nor in the dark noise spectrum. They may be glitches.

5.7 Conclusion and Perspective

By using the 2D deflection system presented in chapter 4.6 a way to sense mechanical modes of a test mirror with a Michelson interferometer is presented. In order to point at any position of the test mirror with a diameter of 2 inches a magnifying telescope is used. Because of clipping effects and spherical aberrations in the telescope only 44% of the test mirror surface is sensed. The beam diameter (at $\frac{1}{e^2}$ intensity) is approximately 0.8 cm on the test mirror. This final spot size on the mirror limits the maximal resolvable mode shape. With the demonstrated twelve spots separated by a distance equal to the beam diameter the mode shape of low order drum modes should already be detectable.

A servo loop was installed to lock the interferometer to the half fringe voltage. It was done to suppress noise sources in the low frequency range in the measured

interference spectrum. Due to resonances of the reference mirror mounted on a piezo stack the bandwidth of the servo system was less than 30 Hz at the end, with a low gain of suppression.
With a finite element simulation of the test mirror the frequency of the first free vibrational drum mode has been determined at around 35 kHz. From calculations of noise sources in the interferometer (see section 5.6.2) the shot noise could be the limiting factor for the detection of thermally excited modes of the test mirror at around 35 kHz.
But the measured noise floor of the interference spectrum with balanced detection shows that it is roughly one order of magnitude higher than the equivalent mirror surface displacement due to this thermally excited mode. The measured spectrum needs to be investigated further in order to determine the noise sources. This is crucial to increase the sensitivity of the interferometer. The additional noise that has been measured could come from the reference arm, whose contribution has not been considered in the noise estimation in section 5.6.2. The observed peaks at 16, 32 and 48 kHz may come from the reference mirror as well since it has lower mechanical quality factors because of the piezo mount and of the fact that it is not in vacuum. If this measurement has not be done in perfect balanced detection, it could also be that these peaks are due to the residual RIN of the laser in the measured signal.

There are several opportunities to enhance the presented system. This can be either done by increasing the spatial sensing resolution or by increasing the sensitivity of the interferometer:

- The magnification of the telescope could be adapted better in order to avoid clipping of the deflected beams. One could also consider using lenses with larger diameters than the test mirror to avoid clipping in the telescope.

- The use of two aspheric lenses in the telescope in the main arm would reduce spherical aberrations. It would decrease the phase difference of the deflected beams.

- The assembly of piezo and mirror should be redesigned in such a way as to avoid resonances in the low frequency range. In this way the locking bandwidth of the servo system could be increased. This would results in better suppression of low frequency noise.

- The error signal for the servo loop was taken from the interference signal measured with a photodiode PD3 at port 1 of the interferometer. In this setup the servo system converts laser intensity noise into phase noise of the interference signal. By calculating the error signal based on balanced detection

the set point is set to zero and will always correspond to the half fringe of the interference signal.

In order to observe eigenmodes of the test mirror with the presented table-top system one needs to amplify them first. Possible ways to do this are presented in figure 5.10. The mirror can be forced to oscillate by electrostatic forces of electrostatic actuators [135]. The actuator could be driven first by a modulated signal that is swept close to the eigenfrequency of a mechanical mode of the mirror. The photodiode signal is filtered with a band pass filter around the eigenmode frequency and amplified first before being sent to the electrostatic actuators. In this way the eigenmode is amplified in a positive feedback-loop via electrostatic forces.
The driver signal of the Y-AOM can also be modulated at the frequency of the mechanical mode. In this way the optical power of the laser beam pointing at the mirror is modulated with the frequency of the eigenmode of the mirror. If the phase is well adjusted the mirror mode is then amplified via the radiation pressure [130, 136].
In a second step the eigenmode of the mirror can be characterized. Therefore the laser power should not be modulated further to sense the mechanical mode. Its quality factor can be determined by measuring the characteristic time of the exponential ringdown of the amplitude of the mechanical mode. In a third step our system can be used to damp this eigenmode of the mirror as described in chapter 3.

If the presented system were installed in the current GW detectors it is possible that thermal modes of the GW detector test masses could already be observed. The quality factors of their mechanical modes are higher and their frequencies are lower [137] compared to the investigated test mirror. Consequently, the amplitude spectral density of the thermal modes of the GW test masses is higher so they could already be detected with the presented system. This means that also PI in the GW detector could be detected with our system.

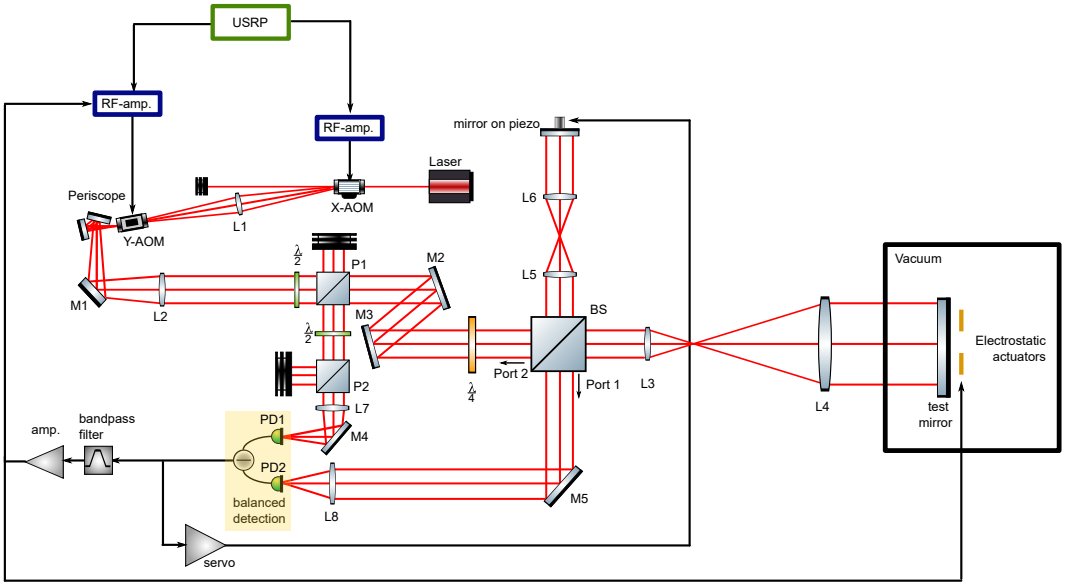

Fig. 5.10: Schematic of possible ways to amplify eigenmodes of the test mirror in a positive feedback loop. The mirror is forced to oscillate by electrostatic forces.The balanced detection signal is filtered with a band pass filter at the frequency of the eigenmode and amplified. This signal can be sent to the electrostatic actuators to amplify the eigenmode via electrostatic forces. Otherwise it can be sent to the RF-amplifier of the Y-AOM to modulate the optical power of the laser beam pointing at the mirror to amplify the eigenmode via radiation pressure.

6 Conclusion

Parametric Instability is a limiting factor of the intra-cavity power in gravitational wave detectors. High optical power in the Fabry-Perot arm cavities decreases the shot noise of the detectors and increases the sensitivity at high frequency (>100 Hz). Advanced LIGO had during O3 an average circulating power in the cavities of 239 kW in the Livingston Observatory and 201 kW in the Hanford Observatory [39]. This is around 30% of the design power. Advanced Virgo was running with 160 kW in their cavities corresponding to 23% of its design power.

Before O3, acoustic mode dampers were implemented at each test mass of the LIGO interferometers to reduce the Q-factor of unstable mechanical modes. These dampers resulted in an increase of less than 1% of thermal noise into the interferometer [67]. In Virgo PI has been observed once during O3, while the interferometer input power was increased from 18.5 W to 27 W during the locking phase [138]. Next generation GW foresee to run with intra-cavity powers of several MW with an increase of the sensitivity of a factor of ten compared to current detectors. Thus, more PIs are expected involving mechanical modes with different kinds of mode shapes. Flexible PI mitigation strategies are needed which are effective for any kind of involved unstable mechanical modes and higher-order optical modes. These strategies should not increase the noise level in the detector to achieve the required sensitivity.

In this thesis a PI mitigation strategy based on radiation pressure of a small movable laser beam is presented: the idea is to decrease the Q-factor of unstable mirror modes via the damping force of a laser beam that points at different lobes of the spatial mode shape. This active damping scheme is similar to the demonstrated damping with ESD [57] but with a different kind of force which can be spatially flexible applied and is easily adjustable. The radiation pressure force could also be used to deform the surface of the mirrors in order to decrease the gain of the higher-order mode which is involved in PI.

In chapter 3 the requirements of the auxiliary laser are estimated: A laser with a low RIN and an optical power of some Watts should be sufficient to damp arbitrary unstable mechanical modes with a high overlap. This requires a reliable and sensitive sensing method to detect PI as early as possible. The mode shape and frequency of the involved mechanical mode needs to be determined. No significant noise coupling into the interferometer are expected, as this was also the case for damping with electrostatic forces [57]. The wavelength of the auxiliary laser should be chosen in a way that the beam is reflected by the high reflectivity coating of the test masses

and does not resonate in the arm cavities. A fast deflected beam is needed with a deflection rate of several MHz to damp unstable eigenmodes with frequencies up to several hundred kHz.

First experimental studies of the active PI mitigation scheme are presented in chapter 4 and 5, with the perspective of implementing such a system in current GW detectors. In chapter 4 experimental investigations on a beam deflection system based on acousto-optic deflectors are discussed. The challenge was to generate a fast changing AOM driver signal. The optical generation of a fast modulated radio frequency based on heterodyne detection was demonstrated. Fast frequency modulations were achieved due to the high bandwidth of electro-optic modulators of several GHz used in the Mach-Zehnder interferometer of the setup. The signal generation in this way turned out to be quite complex due to many possible error sources in the optical setup.

The generation of two different AOM driver signals with a software-defined radio platform was investigated. Commutation times of 2.2 ns were measured which made it possible to program a fast changing arbitrary AOM driver signal. In this way a beam deflection rate of 10 MHz in two dimensions was achieved, with a spot diameter of 1/6 of the target mirror diameter. This should be sufficient to damp different kinds of unstable mechanical modes with a good overlap. The maximal available optical power of the deflected beam is 3.6 W. First estimations based on a simple mode of a damped harmonic oscillator show that the corresponding radiation pressure force of 24 nN is sufficient to damp arising unstable mechanical modes. A more precise model is needed, which includes arising PI in the cavity, to estimate the impact of the applied radiation pressure force of a small laser beam on the optical modes in the cavity. In this way an optimal scan pattern of the movable beam for arbitrary mode shapes can be calculated.

A sensing method of PI is proposed and first experimental investigations are presented in chapter 5. The movable beam from the 2D deflection system from chapter 4 was used to sense mechanical modes of a test mirror in a Michelson interferometer. A magnifying telescope was implemented to cover the whole test mirror surface with a diameter of two inches with the sensing beam. Due to spherical aberrations in the telescope, the effective sensing area was limited. With a sensitivity corresponding to a differential arm length change of $\delta L = 4.8 \cdot 10^{-14} \frac{\mathrm{m}}{\sqrt{\mathrm{Hz}}}$, no thermally excited eigenmodes of the mirror were observed. First estimations of noise sources in the interferometer show that the amplitude of the first thermally excited drum mode at around 35 kHz is of the same order of magnitude than the ASD of the shot noise in the interferometer. A servo loop to lock the interferometer was implemented, which worked only with a low bandwidth due to moving resonances in the assembly of piezo-actuator and reference mirror.

Several propositions to increase the spatial resolution of this system as well as the sensitivity of the interferometer are given in Chapter 5.7.

It was also proposed to use the investigated sensing setup to excite first mechanical

modes of the test mass in order to sense and damp them with the same setup. In this way the impact of a small damping force on a mirror surface can experimentally be studied. This will be a next important step in the development of an active PI mitigation scheme based on radiation pressure. Before implementing such a system in current and next generation GW detectors a dedicated study is required and the auxiliary laser system as well as the mirror control system need to be adapted.

Bibliography

[1] A. Einstein. “Die Grundlage der allgemeinen Relativitätstheorie”. In: *Annalen der Physik* 4.49 (1916), pp. 769–822 (cit. on p. 1).

[2] James B. Hartle, ed. *Gravity An introduction to Einstein’s General Relativity*. San Francisco: Addison Wesley, 2003 (cit. on pp. 1, 5).

[3] David G. Blair, Eric J. Howell, LI Ju, and Chunnong Zhao, eds. *Advanced Gravitational Wave Detectors*. New York: Cambridge University Press, 2012 (cit. on pp. 1, 6, 10).

[4] Carl Blair. “Parametric Instability in Gravitational Wave Detectors”. PhD thesis. University of Western Australia, 2017 (cit. on pp. 1, 21, 23, 26, 30, 83).

[5] ET Steering Committee Editorial Team. *Design Report Update 2020 for the Einstein Telescope*. Tech. rep. 2020 (cit. on pp. 1, 12, 20, 23).

[6] B. P. Abbott et al. “Observation of Gravitational Waves from a Binary Black Hole Merger”. In: *Physical Review Letters* 116.061102 (Feb. 2016) (cit. on p. 2).

[7] Diego Bersanetti, Barbara Patricelli, Ornella Juliana Piccinni, et al. “Advanced Virgo: Status of the Detector, Latest Results and Future Prospects”. In: *Universe* 7.322 (Aug. 2021) (cit. on pp. 2, 11, 12, 20).

[8] J.Weber. “Detection and Generation of Gravitational Waves”. In: *Physical Review* 117.1 (Jan. 1960), pp. 306–313 (cit. on p. 2).

[9] J.Weber. “Observation of the thermal fluctuations of a Gravitational-Wave detector”. In: *Physical Review Letters* 17.24 (Dec. 1966), pp. 1228–1230 (cit. on p. 2).

[10] J.Weber. “Evidence for discovery of gravitational radiation”. In: *Physical Review Letters* 22.24 (June 1969), pp. 1320–1324 (cit. on p. 2).

[11] Odylio Denys Aguiar. “Past, present and future of the Resonant-Mass gravitational wave detectors”. In: *Research in Astronomy and Astrophysics* 11.1 (2011), pp. 1–42 (cit. on pp. 2, 3).

[12] Jorge L. Cervantes-Cota, Salvador Galindo-Uribarri, and George F. Smoot. “A Brief History of Gravitational Waves”. In: *Universe* 2.22 (Sept. 2016) (cit. on pp. 3, 7).

[13] G. E. Moss, L. R. Miller, and R. L. Forward. “Photon-Noise-Limited Laser Transducer for Gravitational Antenna”. In: *Applied Optics* 10.11 (Nov. 1971), pp. 2495–2498 (cit. on p. 3).

[14] Robert L. Forward. “Wideband laser-interferometer graviational-radiation experiment”. In: *Physical Review D* 17.2 (Jan. 1978), pp. 379–390 (cit. on p. 3).

[15]Rainer Weiss. “Electronically Coupled Broadband Gravitational Antenna”. In: *Quarterly Progress Report,* 105 (1972), p. 54 (cit. on p. 3).

[16]H Billing, K. Maischberger, A. Rudiger, et al. “An argon laser interferometer for the detection of gravitational radiation”. In: *Journal of Physics E: Scientific Instruments* 17.11 (1979), pp. 1043–1050 (cit. on p. 3).

[17]Stefan L. Danilishin and Farid Ya. Khalili. “Quantum Measurement Theory in Gravitational-Wave Detectors”. In: *Living Reviews in Relativity* 15.1 (Mar. 2012) (cit. on p. 5).

[18]S Hild, H Grote, J Degallaix, et al. “DC-readout of a signal-recycled gravitational wave detector”. In: *Classical and Quantum Gravity* 26.055012 (Feb. 2009) (cit. on p. 5).

[19]Donald R. Herriott and Harry J. Schulte. “Folded Optical Delay Lines”. In: *Applied Optics* 4.8 (Aug. 1965), pp. 883–889 (cit. on p. 6).

[20]Barry C. Barish and Rainer Weiss. “LIGO and the Detection of Gravitational Waves”. In: *Physics Today* 52.10 (Oct. 1999), pp. 44–50 (cit. on p. 6).

[21]C.Bradaschia, R.Del Fabbro, A.Di Virgilio, et al. “The Virgo project: A wide band antenna for gravitational wave detection”. In: *Nuclear Instruments and Methods in Physics Research Section A: Accelerators, Spectrometers, Detectors and Associated Equipment* 289.3 (Apr. 1990), pp. 518–525 (cit. on p. 6).

[22]H Lück and the GEO600 Team. “The GEO600 project”. In: *Classical and Quantum Gravity* 14 (Feb. 1997), pp. 1471–1476 (cit. on p. 6).

[23]Seiji Kawamura and the TAMA Collaboration. “Laser Interferometer Gravitational Wave Detector:The Current Status of the TAMA Project”. In: *Progress of Theoretical Physics Supplement* 136 (Apr. 1999), pp. 72–86 (cit. on p. 6).

[24]The LIGO Scientific Collaboration et al. “Advanced LIGO”. In: *Classical and Quantum Gravity* 32.074001 (2015) (cit. on pp. 7, 15).

[25]F. Acernese et al. “The Advanced Virgo detector”. In: *Journal of Physics: Conference Series* 610.012014 (2015) (cit. on pp. 7, 15).

[26]The Virgo Collaboration. *Advanced Virgo Technical Design Report VIR-0128A-12*. Tech. rep. 2012 (cit. on pp. 7, 31).

[27]Brian l. Meers. “Recycling in laser-interferometric gravitational-wave detectors”. In: *Physical Review D* 38.8 (Oct. 1988), pp. 2317–2326 (cit. on p. 7).

[28]*European Gravitational Observatory, Virgo*. [retrieved 12 December 2021], `http://public.virgo-gw.eu/a-worldwide-network/` (cit. on pp. 8, 10).

[29]R. Abbott et al. “GWTC-2: Compact Binary Coalescences Observed by LIGO and Virgo during the First Half of the Third Observing Run”. In: *Physical Review X* 11.021053 (June 2021) (cit. on p. 9).

[30]Yoichi Aso, Yuta Michimura, Kentaro Somiya, et al. “Interferometer design of the KAGRA gravitational wave detector”. In: *Physical Review D* 88.043007 (Aug. 2013) (cit. on p. 9).

[31]T Akutsu, M Ando, K Arai, et al. “First cryogenic test operation of underground km-scale gravitational-wave observatory KAGRA”. In: *Classical and Quantum Gravity* 36.165008 (July 2019) (cit. on p. 9).

[32]Tarun Souradeep, Sendhil Raja, Ziauddin Khan, C. S. Unnikrishnan, and Bala Iyer. "LIGO-India – a unique adventure in Indian science". In: *Current Science* 113.4 (Aug. 2017), pp. 672–677 (cit. on p. 9).

[33]Peter R. Saulson. "Terrestrial gravitational noise on a gravitational wave antenna". In: *Physical Review D* 30.4 (Aug. 1984) (cit. on p. 10).

[34]Jennifer C. Driggers, Matthew Evans, Keenan Pepper, and Rana Adhikari. "Active noise cancellation in a suspended interferometer". In: *Review of Scientific Instruments* 83.024501 (Feb. 2012) (cit. on p. 11).

[35]M. G. Beker, G. Cella, R. DeSalvo, et al. "Improving the sensitivity of future GWobservatories in the 1–10 Hz band: Newtonian and seismic noise". In: *General Relativity and Gravitation* 43 (May 2010), pp. 623–656 (cit. on p. 11).

[36]Steven D Penn, Peter H Sneddon, Helena Armandula, et al. "Mechanical loss in tantala/silica dielectric mirror coatings". In: *Classical Quantum Gravity* 20 (June 2003), pp. 2917–2928 (cit. on p. 11).

[37]Yu Levin. "Internal thermal noise in the LIGO test masses: A direct approach". In: *Physical Review D* 57.2 (Jan. 1998), pp. 659–663 (cit. on p. 11).

[38]Lisa Barsotti, Jan Harms, and Roman Schnabel. "Review: Squeezed vacuum states of light for gravitational wave detectors". In: *Reports on Progress in Physics* 82.016905 (Dec. 2018), p. 29 (cit. on p. 12).

[39]A. Buikema, C. Cahillane, G. L. Mansell, et al. "Sensitivity and performance of the Advanced LIGO detectors in the third observing run". In: *Physical Review D* 102.062003 (Sept. 2020) (cit. on pp. 12, 103).

[40]M Punturo, M Abernathy, F Acernese, et al. "The Einstein Telescope: a third-generation gravitational wave observatory". In: *Classical and Quantum Gravity* 27.19 (Sept. 2010), p. 194002 (cit. on p. 12).

[41]Michele Maggiore, Chris Van Den Broeck, Nicola Bartolo, et al. "Science case for the Einstein telescope". In: *Journal of Cosmology an Astroparticle Physics* 050 (Mar. 2020) (cit. on p. 12).

[42]M Abernathy, F Acernese, P Ajith, et al. *Einstein gravitational wave Telescope conceptual design study*. Tech. rep. ET Science Team, 2011 (cit. on p. 12).

[43]B. P. Abbott et al. "Exploring the sensitivity of next generation gravitational wave detectors". In: *Classical and Quantum Gravity* 34.4 (Jan. 2017), p. 044001 (cit. on pp. 13, 20, 23).

[44]Evan D. Hall, Kevin Kuns, Joshua R. Smith, et al. "Gravitational-wave physics with Cosmic Explorer: Limits to low-frequency sensitivity". In: *Physical Review D* 103.122004 (June 2021) (cit. on p. 13).

[45]John A. Sidles and Daniel Sigg. "Optical torques in suspended Fabry–Perot interferometers". In: *Physics Letters A* 354 (Jan. 2006), pp. 167–172 (cit. on p. 15).

[46]Matthew Evans et al. "Observation of Parametric Instability in Advanced LIGO". In: *Physical Review Letters* 114.161102 (Apr. 2015) (cit. on pp. 15, 17–19, 21).

[47]V.B.Braginsky, S.E.Strigin, and S.P.Vyatchanin. "Parametric oscillatory instability in Fabry–Perot interferometer". In: *Physics Letters A* 287.287 (Sept. 2001), pp. 331–338 (cit. on pp. 15, 18, 20).

[48]V.B.Braginsky, S.E.Strigin, and S.P.Vyatchanin. “Analysis of parametric oscillatory instability in power recycled LIGO interferometer”. In: *Physics Letters A* 305 (Sept. 2002), pp. 111–124 (cit. on pp. 15, 33).

[49]M. Evans, L. Barsotti, and P. Fritschel. “A general approach to optomechanical parametric instabilities”. In: *Physics Letters A* 374 (Nov. 2009), pp. 665–671 (cit. on pp. 15–18).

[50]C. Zhao et al. “Gingin High Optical Power Test Facility”. In: *Journal of Physics: Conference Series* 32.056 (2006) (cit. on p. 18).

[51]C. Zhao, L. Ju, Y. Fan, et al. “Observation of three-mode parametric interactions in long optical cavities”. In: *Physical Review A* 78.023807 (Aug. 2008) (cit. on p. 18).

[52]C. Zhao, Q. Fang, S. Susmithan, et al. “High-sensitivity three-mode optomechanical transducer”. In: *Physical Review A* 84.063836 (Dec. 2011) (cit. on pp. 18, 83).

[53]Ivan S. Grudinin, Andrey B. Matsko, and Lute Maleki. “Brillouin Lasing with a CaF2 Whispering Gallery Mode Resonator”. In: *Physical Review Letters* 102.043902 (Jan. 2009) (cit. on p. 18).

[54]Matthew Tomes and Tal Carmon. “Photonic Micro-Electromechanical Systems Vibrating at X-band (11-GHz) Rates”. In: *Physical Review Letters* 102.113601 (Mar. 2009) (cit. on p. 18).

[55]X. Chen, C. Zhao, S. Danilishin, et al. “Observation of three-mode parametric instability”. In: *Physical Review A* 91.033832 (Mar. 2015) (cit. on p. 18).

[56]S. Gras, P. Fritschel, L. Barsotti, and M. Evans. “Resonant dampers for parametric instabilities in gravitational wave detectors”. In: *Physical Review D* 92.082001 (Oct. 2015) (cit. on pp. 19, 20, 23, 83).

[57]Carl Blair, Slawek Gras, Richard Abbott, et al. “First Demonstration of Electrostatic Damping of Parametric Instability at Advanced LIGO”. In: *Physical Review Letters* 118.151102 (Apr. 2017) (cit. on pp. 19, 22, 25, 29, 83, 103).

[58]Jérôme Degallaix, Chunnong Zhao, Li Ju, and David Blair. “Thermal tuning of optical cavities for parametric instability control”. In: *Journal of the Optical Society of America* 24 (June 2007), pp. 1336–1343 (cit. on pp. 20, 21).

[59]Fahmida Ferdous, Alena A. Demchenko, Sergey P. Vyatchanin, Andrey B. Matsko, and Lute Maleki. “Microcavity morphology optimization”. In: *Physical Review* 90.033826 (Sept. 2014) (cit. on pp. 20, 21).

[60]Andrey B. Matsko, Mikhail V. Poplavskiy, Hiroaki Yamamoto, and Sergey P. Vyatchanin. “Mitigating parametric instability in optical gravitational wave detectors”. In: *Physical Review D* 93.083010 (Apr. 2016) (cit. on pp. 20, 21).

[61]Mikhail V Poplavskiy, Andrey B Matsko, Hiroaki Yamamoto, and Sergey P Vyatchanin. “Diffraction losses of a Fabry-Perot cavity with nonidentical non-spherical mirrors”. In: *Journal of Optics* 22.115603 (Oct. 2020) (cit. on pp. 20, 21, 25).

[62]L Ju, D. G. Blair, C. Zhao, et al. “Strategies for the control of parametric instability in advanced gravitational wave detectors”. In: *Classical and Quantum Gravity* 26.015002 (Dec. 2008) (cit. on pp. 20, 21, 25, 26, 30).

[63] C. Zhao, L. Ju, J. Degallaix, S. Gras, and D. G. Blair. “Parametric Instabilities and Their Control in Advanced Interferometer Gravitational-Wave Detectors”. In: *Physical Review Letters* 94.121102 (Apr. 2005) (cit. on p. 20).

[64] L. Ju, C. Zhaoa, S. Gras, et al. “Comparison of parametric instabilities for different test mass materials in advanced gravitational wave interferometers”. In: *Physics Letters A* 355 (Mar. 2006), pp. 419–426 (cit. on p. 20).

[65] S. Gras, D.G. Blair, and L. Ju. “Test mass ring dampers with minimum thermal noise”. In: *Physics Letters A* 372 (Oct. 2008), pp. 1348–1356 (cit. on pp. 20, 22).

[66] S. Gras, D.G. Blair, and C. Zhao. “Suppression of parametric instabilities in future gravitational wave detectors using damping rings”. In: *Classical and Quantum Gravity* 26.135012 (June 2009) (cit. on pp. 20, 22).

[67] S. Biscans, S. Gras, C. D. Blair, et al. “Suppressing parametric instabilities in LIGO using low-noise acoustic mode dampers”. In: *Phys. Rev. D* 100 (12 Dec. 2019), p. 122003 (cit. on pp. 20, 22–24, 103).

[68] Guilherme Rosa Franzini, Giovanna Ribeiro Campedelli, and Carlos Eduardo Nigro Mazzilli. “A numerical investigation on passive suppression of the parametric instability phenomenon using a rotative non-linear vibration absorber”. In: *International Journal of Non-Linear Mechanics* 105 (May 2018), pp. 249–260 (cit. on p. 20).

[69] V.B.Braginsky and S.P.Vyatchanin. “Low quantum noise tranquilizer for Fabry–Perot interferometer”. In: *Physics Letters A* 293 (Feb. 2002), pp. 228–234 (cit. on p. 21).

[70] S. W. Schediwy, C. Zhao, L. Ju, D. G. Blair, and P. Willems. “Observation of enhanced optical spring damping in a macroscopic mechanical resonator and application for parametric instability control in advanced gravitational-wave detectors”. In: *Physical Review A* 77.013813 (Jan. 2008) (cit. on p. 21).

[71] Zhongyang Zhang, Chunnong Zhao, L. Ju, and D. G. Blair. “Enhancement and suppression of opto-acoustic parametric interactions using optical feedback”. In: *Physical Review A* 81.013822 (Jan. 2010) (cit. on p. 21).

[72] YaoHui Fan, Lucienne Merrill, ChunNong Zhao, et al. “Testing the suppression of opto-acoustic parametric interactions using optical feedback control”. In: *Classical and Quantum Gravity* 27.084028 (Apr. 2010) (cit. on p. 21).

[73] John Miller, Matthew Evans, Lisa Barsotti, et al. “Damping parametric instabilities in future gravitational wave detectors by means of electrostatic actuators”. In: *Physics Letters A* 375.3 (Jan. 2011), pp. 788–794 (cit. on pp. 21, 25, 29, 37).

[74] C. Zhao, L. Ju, J. Degallaix, S. Gras, and D. G. Blair. “Parametric Instabilities and Their Control in Advanced Interferometer Gravitational-Wave Detectors”. In: *Physical Review Letters* 94.121102 (June 2005) (cit. on p. 21).

[75] Sunil Susmithan, Chunnong Zhao, Fang Qi, Li Ju, and David Blair. “Thermal tuning of optical cavities for parametric instability control”. In: *Journal of Physics: Conference Series* 363.012018 (2012) (cit. on p. 21).

[76] Chunnong Zhao, Li Ju, Qi Fang, et al. “Parametric instability in long optical cavities and suppression by dynamic transverse mode frequency modulation”. In: *Physical Review D* 91.092001 (May 2015) (cit. on p. 21).

[77]Y. B. Ma, J. Liu, Y. Q. Ma, et al. “Thermal modulation for suppression of parametric instability in advanced gravitational wave detectors”. In: *Classical and Quantum Gravity* 34.135001 (June 2017) (cit. on p. 21).

[78]T. Hardwick, V. J. Hamedan, C. Blair, A. C. Green, and D. Vander-Hyde. “Demonstration of dynamic thermal compensation for parametric instability suppression in Advanced LIGO”. In: *Classical and Quantum Gravity* 37.205021 (Sept. 2020) (cit. on p. 21).

[79]Jue Zhang, Chunnong Zhao, Li Ju, and David Blair. “Mitigating parametric instability in optical gravitational wave detectors”. In: *Classical and Quantum Gravity* 37.075015 (Mar. 2020) (cit. on p. 21).

[80]Mindy Jacobson, Michael Smith, Phil Willems, and Aidan Brooks. *Auxiliary Optics Support System Design Requirements Document, Vol. 1 Thermal Compensation System*. Tech. rep. LIGO Sience Collaboration, Nov. 2021 (cit. on p. 22).

[81]Margherita Turconi, Thomas Harder, Rémi Soulard, and Walid Chaibi. *Mitigation of Parametric Instability*. contribution to the 2019 EW/QCD/Gravitation session of the 54th Rencontres de Moriond (2019), `https://arxiv.org/abs/1910.06678` (cit. on p. 27).

[82]Carl Blair, Sunil Susmithan, Chunnong Zhao, et al. “Radiation pressure excitation of test mass ultrasonic modes via three mode opto-acoustic interactions in a suspended Fabry–Pérot cavity”. In: *Physics Letters A* 377 (May 2013), pp. 1970–1973 (cit. on p. 27).

[83]Chunnong Zhao, Li Ju, Qi Fang, et al. “Parametric instability in long optical cavities and suppression by dynamic transverse mode frequency modulation”. In: *Physical Review D* 91.092001 (May 2015) (cit. on p. 27).

[84]Stefan W. Ballmer. “LIGO interferometer operating at design sensitivity with application to gravitational radiometry”. PhD thesis. Massachusetts Institute of Technololgy, 2006 (cit. on p. 31).

[85]D Estevez, P Lagabbe, A Masserot, et al. “The Advanced Virgo photon calibrators”. In: *Classical and Quantum Gravity* 38.075007 (Feb. 2021) (cit. on p. 31).

[86]S. Karki, D. Tuyenbayev, S. Kandhasamy, et al. “The Advanced LIGO photon calibrators”. In: *Review of scientific instruments* 87.114503 (Nov. 2016) (cit. on p. 31).

[87]Thomas Klein and Robert Huber. “High-speed OCT light sources and systems [Invited]”. In: *Biomedical Optics Express* 8.2 (Feb. 2017) (cit. on p. 39).

[88]G. Zhou, F. Mok, and D. Psaltis. “Beam Deflectors and Spatial Light Modulators for Holographic Storage Application”. In: *Holographic Data Storage*. Ed. by Hans J. Coufal, Demetri Psaltis, and Glenn T. Sincerbox. Vol. 76. springer, 2000, pp. 241–257 (cit. on p. 39).

[89]Mona Jarrahi, R. Fabian W. Pease, David A. B. Miller, and Thomas H. Lee. “Optical switching based on high-speed phased array optical beam steering”. In: *Applied Physics Letters* 92.014106 (Jan. 2008) (cit. on p. 39).

[90]Gaddum Duemani Reddy and Peter Saggau. “Fast three-dimensional laser scanning scheme using acousto-optic deflectors”. In: *Journal of Biomedical Optics* 10.064038 (Dec. 2005) (cit. on p. 39).

[91] Gerald F. Marshall and Glenn E. Stutz, eds. *Handbook of Optical and Laser Scanning*. Boca Raton: CRC Press Taylor & Francis Group, 2012 (cit. on pp. 39, 40, 42, 44).

[92] I. C. Chang. "Acousto-Optic Devices and Applications". In: *Handbook of Optics*. Ed. by Bass M. et al. McGRAW-HILL , INC ., 1995 (cit. on pp. 39, 40).

[93] Emil Haellstig, Johan Stigwall, Mikael Lindgren, and Lars Sjoqvist. "Laser beam steering and tracking using a liquid crystal spatial light modulator". In: *Proceedings SPIE 5087* (Aug. 2003) (cit. on p. 39).

[94] G.R.B.E. Römer and P. Bechtold. "Electro-optic and acousto-optic laser beam scanners - Invited Paper -". In: *Physics Procedia* 10 (2014), pp. 29–39 (cit. on p. 39).

[95] E. I. GORDON. "A Review of Acoustooptical Deflection and Modulation Devices". In: *Applied Optics* 5.10 (Oct. 1966), pp. 1629–1639 (cit. on pp. 39, 43).

[96] D. P. Resler, D. S. Hobbs, R. C. Sharp, L. J. Friedman, and T. A. Dorschner. "High-efficiency liquid-crystal optical phased-array beam steering". In: *Optics Letters* 21.9 (May 1996) (cit. on p. 39).

[97] I. Gorog, J. D. Knox, and P.V.Goerdertier. "A Television-Rate Laser Scanner. I. General Considerations". In: *RCA Review* 33.4 (Dec. 1972), pp. 623–666 (cit. on p. 39).

[98] W. Ronny Huang, Juan Montoya, Jan E. Kansky, et al. "High speed, high power one-dimensional beam steering from a 6-element optical phased array". In: *Optics Express* 20.16 (July 2012) (cit. on p. 39).

[99] Yoshikuni Hirano, Yuji Miyamoto, Masato Miura, et al. "High-Speed Optical-Beam Scanning by an Optical Phased Array Using Electro-Optic Polymer Waveguides". In: *IEEE* 20.2 (Mar. 2020) (cit. on p. 39).

[100] Shogo Yagia and Kazuo Fujiuraa. "Electro-optic KTN devices". In: *Physics Procedia* 56 (2014), pp. 40–47 (cit. on p. 39).

[101] G.R.B.E. Römer and P. Bechtoldb. "Electro-optic and acousto-optic laser beam scanners". In: *Physics Procedia* 56 (2014), pp. 29–39 (cit. on p. 39).

[102] Wenbin Zhu, Ju-Hung Chao, Chang-Jiang Chen, Shizhuo Yin, and Robert C. Hoffman. "Three order increase in scanning speed of space charge-controlled KTN deflector by eliminating electric field induced phase transition in nanodisordered KTN". In: *Scientific Reports* 6.33143 (Sept. 2016) (cit. on p. 39).

[103] Ju-Hung Chao, Wenbin Zhu, Chang-Jiang Chen, et al. "High speed non-mechanical two-dimensional KTN beam deflector enabled by space charge and temperature gradient deflection". In: *Optics Express* 25.13 (June 2017), pp. 15481–15492 (cit. on p. 39).

[104] Chang-Jiang Chen, Ju-Hung Chao, Yun Goo Lee, et al. "Enhanced electro-optic beam deflection of relaxor ferroelectric KTN crystals by electric-field-induced high permittivity". In: *Optics Letters* 44.22 (Nov. 2019), pp. 5557–5560 (cit. on p. 39).

[105] *High speed, high power 2D beam steering for mitigation of optomechanical parametric instability in gravitational wave detectors*. [submitted 20 January 2022], `http://arxiv.org/abs/2201.08272` (cit. on p. 40).

[106] L . Brillouin. "Diffusion de la lumière et des rayons x par un corps transparent homogène". In: *Annales de Physique* 9.17 (Feb. 1921), pp. 88–122 (cit. on p. 40).

[107]R.Lucas and P. Biquard. “Propriétés optiques des milieux solides et liquides soumis aux vibration élastiques ultra sonores”. In: *Proceedings of the Nationalacademy of Sciences* 18.6 (June 1932), pp. 464–477 (cit. on p. 40).

[108]P.Debye and F.W.Sears. “On the scattering of light by supersonic waves”. In: *Proceedings of the Nationalacademy of Sciences* 18.6 (June 1932), pp. 409–414 (cit. on p. 40).

[109]C.V.Raman and N.S.Nagendra Nath. “The Diffraction of Light by High Frequency Sound Waves, Part 1+2”. In: *Proceedings of the Indian Academy of Sciences* 2 (Sept. 1935), pp. 406–420 (cit. on p. 40).

[110]C.V.Raman and N.S.Nagendra Nath. “The Diffraction of Light by High Frequency Sound Waves, Part 3-5”. In: *Proceedings of the Indian Academy of Sciences* 3 (Sept. 1936), pp. 75–84, 119–125, 459–465 (cit. on p. 40).

[111]A. Korpel, R. Adler, P. Desmares, and W. Watson. “A Television Display Using Acoustic Deflection and Modulation of Coherent Light”. In: *Applied Optics* 5.10 (Oct. 1966), pp. 1667–1675 (cit. on pp. 43, 70).

[112]Itay Peled, Ron Kaminsky, and Zvi Kotler. “Acousto-optics bandwidth broadening in a Bragg cell based on arbitrary synthesized signal methods”. In: *Applied Optics* 54.16 (May 2015), pp. 5056–5073 (cit. on p. 43).

[113]S. E. Harris and R. W. Wallace. “Acousto-Optic Tunable Filter*”. In: *Journal of the Optical Society of America* 59.6 (1969), pp. 744–747 (cit. on p. 43).

[114]D.L. Hecht. “Spectrum Analysis Using Acousto-Optic Devices”. In: *Proc. SPIE* 0090 (Dec. 1976) (cit. on p. 43).

[115]W.T. Rhodes. “Acousto-optic signal processing: Convolution and correlation”. In: *Proceedings of the IEEE* 69.1 (Jan. 1981), pp. 65–79 (cit. on p. 43).

[116]Amnon Yariv and Pochi Yeh, eds. *Optical Waves in Crystals Propagation and Control of Laser Radiation*. New York: John Wiley & Sons, Inc., 1984 (cit. on p. 44).

[117]*AA opto-electronic*. [retrieved 03 December 2020], `http://www.aaoptoelectronic.com` (cit. on p. 44).

[118]*Isomet Cooporation*. [retrieved 12 December 2020], `http://www.isomet.com/` (cit. on p. 44).

[119]*Gooch & Hoosego*. [retrieved 12 December 2020], `https://gandh.com/` (cit. on p. 44).

[120]Thaned Pruttivarasin and Hidetoshi Katori. “A control hardware based on a field programmable gate array for experiments in atomic physics”. In: *Review of Scientific Instruments* 91.033203 (Mar. 2020) (cit. on p. 44).

[121]Yuanbo Du, Wenbing Li, Yapeng Ge, et al. “Note: A high-frequency signal generator based on direct digital synthesizer and field-programmable gate array”. In: *Review of Scientific Instruments* 88.096103 (Sept. 2017) (cit. on p. 44).

[122]O. E. DeLange. “Optical heterodyne detection”. In: *IEEE Spectrum* 5 (Oct. 1968), pp. 77–85 (cit. on p. 45).

[123]K. Razdan and D. A. Van Baak. “Demonstrating optical beat notes through heterodyne experiments”. In: *American Journal of Physics* 70 (Oct. 2002) (cit. on p. 45).

[124] *Ettus Research*. [retrieved 30 March 2022], https://www.ettus.com/all-products/x310-kit/ (cit. on p. 64).

[125] *National Instruments*. [retrieved 30 March 2022], https://zone.ni.com/reference/en-XX/help/373380J-01/usrphelp/2944_block_diagram/ (cit. on p. 65).

[126] Zhili Huang, Nicole Munro, Andreas F. R. Huhmer, and James P. Landers. "Acousto-Optical Deflection-Based Laser Beam Scanning for Fluorescence Detection on Multichannel Electrophoretic Microchips". In: *Analytical Chemistry* 71.23 (Dec. 1999), pp. 5309–5314 (cit. on p. 70).

[127] Gergely Katona, Gergely Szalay, Pál Maák, et al. "Fast two-photon in vivo imaging with three-dimensional random-access scanning in large tissue volumes". In: *Nature Methods* (Jan. 2012) (cit. on p. 70).

[128] Walther Akemann, Jean-François Léger, Cathie Ventalon, et al. "Fast spatial beam shaping by acousto-optic diffraction for 3D non-linear microscopy". In: *Optics Express* 23.22 (Oct. 2015) (cit. on p. 70).

[129] Craig Scott, ed. *Introduction to Optics and Optical Imaging*. Piscataway, New York: Wiley-IEEE Press, 1998 (cit. on p. 72).

[130] Y. Hadjar, P. F. Cohadon, C. G. Aminoff, M. Pinard, and A. Heidmann. "High-sensitivity optical measurement of mechanical Brownian motion". In: *Europhysics Letters* 47.5 (Sept. 1999), pp. 545–551 (cit. on pp. 83, 100).

[131] O. Arcizet, P.-F. Cohadon, T. Briant, et al. "High-Sensitivity Optical Monitoring of a Micromechanical Resonator with a Quantum-Limited Optomechanical Sensor". In: *Physical Review Letters* 97.133601 (Sept. 2006) (cit. on p. 83).

[132] Alejandro Domínguez-López, Alexia López-Gil, Sonia Martín-López, and Miguel González-Herráez. "Signal-to-Noise Ratio Improvement in BOTDA Using Balanced Detection". In: *IEEE Photonics Technology Letters* 26.4 (Feb. 2014), pp. 338–341 (cit. on p. 86).

[133] Kenji Numata, Amy Kemery, and Jordan Camp. "Thermal-Noise Limit in the Frequency Stabilization of Lasers with Rigid Cavities". In: *Physical Review Letters* 93.250602 (Dec. 2004) (cit. on p. 86).

[134] Peter R. Saulson. "Thermal noise in mechanical experiments". In: *Physical Review D* 42.8 (Oct. 1990), pp. 2437–2445 (cit. on p. 96).

[135] Sibilla Di Pace. "Towards the observation of the radiation pressure noise in a suspended interferometer : the QuRaG experiment". PhD thesis. Université de Nice- Sophia Antipolis, Università di Roma- La Sapienza, 2014 (cit. on p. 100).

[136] M. Feat, C. Zhao, L. Ju, and D. G. Blair. "Demonstration of low power radiation pressure actuation for control of test masses". In: *Review of Scientific Instruments* 76.036107 (Mar. 2005) (cit. on p. 100).

[137] David E. Cohen, Annalisa Allocca, Gilles Bogaert, Paola Puppo, and Thibaut Jacqmin. "Toward optomechanical parametric instability prediction in ground-based gravitational wave detectors". In: *Applied Optics* 60.27 (Sept. 2021), pp. 8540–8549 (cit. on p. 100).

[138] David Cohen. "Study of optomechanical parametric instabilities in the Advanced Virgo detector". PhD thesis. Université Paris-Saclay, 2021 (cit. on p. 103).

List of Figures

List of Tables

Colophon

This thesis was typeset with LaTeX 2_ε. It uses the *Clean Thesis* style developed by Ricardo Langner. The design of the *Clean Thesis* style is inspired by user guide documents from Apple Inc.

Download the *Clean Thesis* style at `http://cleanthesis.der-ric.de/`.